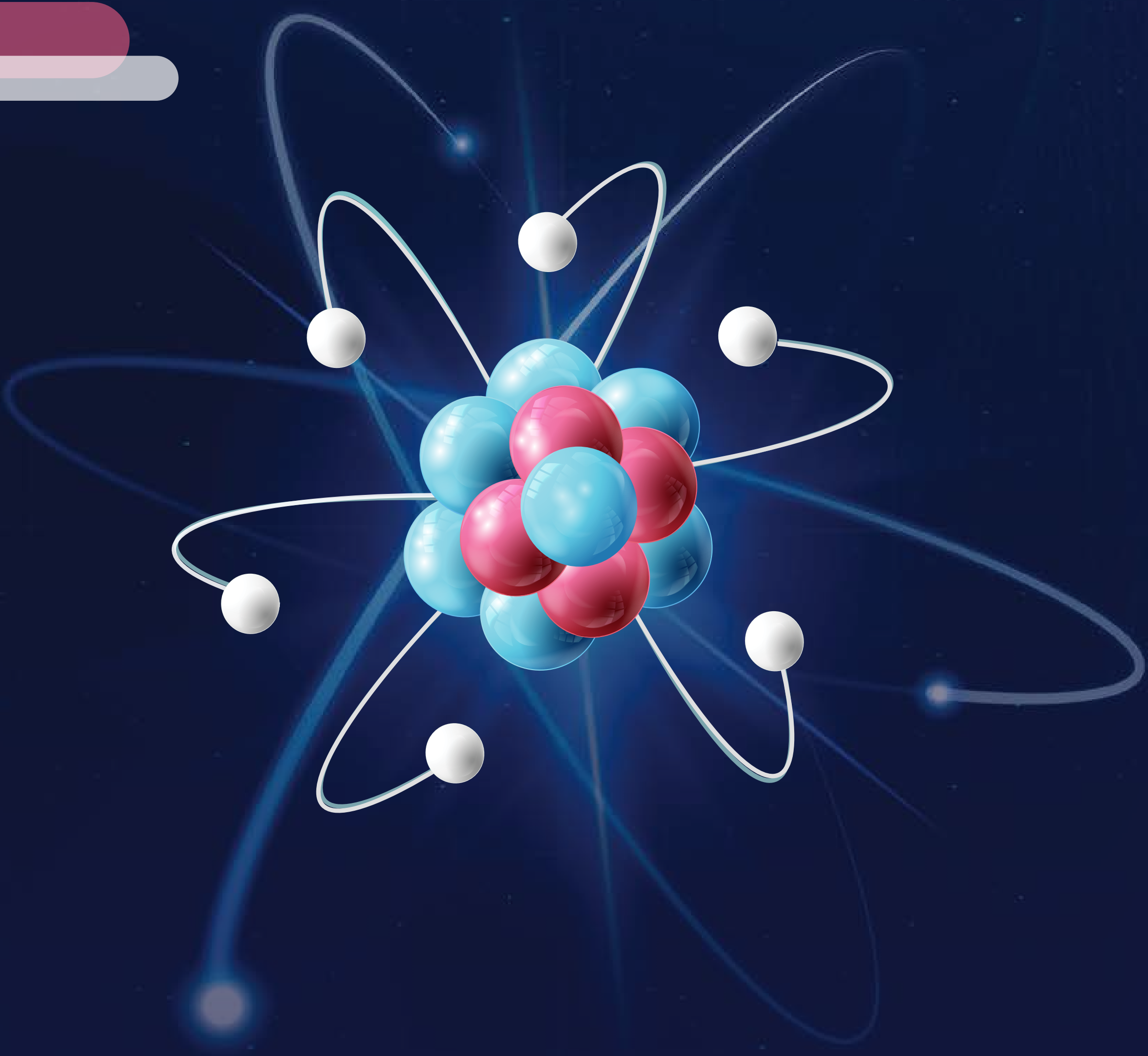

PAZY Foundation

International Nuclear Information System
IAEA INIS

The Israeli Institute for fusion Research (IIFR)

ROTEM
Rotem Industries Ltd.

GOA-Tech

ITecאיטק

דיבידנד
פתרונות פיננסים וביטוח

ABSTRACTS BOOK

KALEIDOSCOPE
Conferences | Events | Exhibitions

Table of Contents

Opening Letter

It is a great honor and privilege for us, the Israel Nuclear Society (INS) and the Israel Society for Radiation Protection (ISRP), to invite you to the 31st Conference of the Nuclear Societies in Israel.

We expect about 200 local and international participants, among them: physicists, Nuclear engineers, Medical Physicists, Radiologists, Radiation Technologists, coming from industry, government, healthcare, and leading universities in Israel and abroad.

In the name of the organizing committee, we invite you to participate in the coming INS31 conference and hope you will find it interesting, challenging, and productive.

Your suport would be extremely important in ensuring the success of the conference, your particaiption will provide an excellent opportunity to gain broad exposure of your work amongst the conference participants.

We look forward to welcoming you all at INS31,

The organizing committee

Plenary Speakers

Prof. Elisabetta Boaretto

Scientific Archaeology and D-REAMS Laboratory, Weizmann Institute of Science. Graduated in Nuclear Physics at the University of Padova and PhD in Physics at the Hebrew University, Prof Boaretto is the Director of the Kimmel Center for Archaeological Science and of the Dangoor Research Accelerator for Radiocarbon dating at the Weizmann Institute.

She is the incumbent of the Dangoor Professorial Chair of Archaeological Sciences at the Weizmann Institute of Science. Her research is focus on archaeological questions related to material, cultural and climatic changes where high resolution chronology with radiocarbon is fundamental. For this she developed novel methods to study the archaeological record and the nature of the associated material with scientific instrumentation in the archaeological excavation and in the laboratory. Her research has changed our understanding of the human past for the past 50,000 years in Israel.

Dr. Itay Gissis

is an experimental physicist with over 18 years experience in leading R&D projects primarily in RAFAEL. Itay is a Psagot D graduate in Physics and electrical engineering and has an MSc. and Phd. in Physics from the Technion in the field of laboratory and astrophysical plasmas, diagnostics, and pulse power. Currently Itay leads the R&D team of the Israeli fusion energy startup company - nT-Tao developing the compact core fusion concept. (www.linkedin.com/in/itay-gissis)

Prof. François Paquet

is currently Deputy Director of research and expertise in the environment at the French Authority for Nuclear Safety and Radiation Protection, France. He is also Chairman of the Task Group on Internal Dose Coefficients (IDC) and Vice-Chairman of the committee 2 of the International Commission on Radiological Protection (ICRP). Francois Paquet is author or co-author of 180 peer-reviewed publications, 13 books and 11 book chapters.

Prof. Guy Ron

is a nuclear physicist and computational biologist at the Racah Institute of Physics, Hebrew University of Jerusalem. His research spans nuclear physics, particle physics, and computational biology, focusing on fundamental forces of nature, precision measurements, and biological data analysis. In computational biology, he has contributed to innovative projects such as multiplexed single-molecule epigenetic analysis for cancer diagnostics.Prof. Ron earned his Ph.D. (2009) in Physics from Tel Aviv University, specializing in nuclear physics under Prof. Eli Piasetzky. His Ph.D. work provided groundbreaking insights into proton electromagnetic form factors. He completed postdoctoral fellowships at the Weizmann Institute and Lawrence Berkeley National Laboratory before joining Hebrew University in 2011.Prof Ron also serves on the Israeli National Nuclear Physics Committee and actively contributes to interdisciplinary research in physics and computational biology.

The 31st Conference of the Nuclear Societies in Israel

הכנס ה-31 של האגודות הגרעיניות בישראל

25-27 March 2025 | Hotel Botanica, Haifa

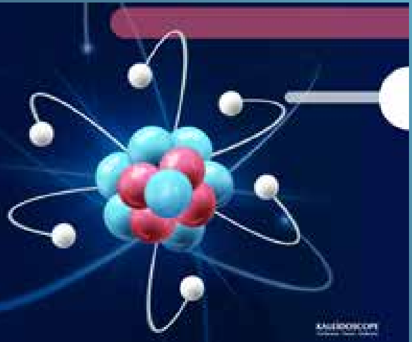

Tuesday 25.3.2025

14:00-18:00 Registration Desk - Hotel Hall

18:00-20:00 Welcome Reception - Hotel Patio

Wednesday 26.3.2025

08:00-09:00 Registration, Reception and Exhibition - Hotel Lobby

09:00-09:15 **Conference Opening - Botanica Garden Hall**

09:15-09:30 **Lior Arazi - Lecture in memory of Prof. Itzhak Kelson, z"l**

09:30-10:30 **Plenary Session 1 - Botanica Garden Hall**

Moderators: Jean Koch and Erez Gilad

09:30-10:00 State of The Art in Internal Dosimetry
François Paquet

10:00-10:30 Introduction to Fusion Energy and nT-Tao Compact Core Approach
Itay Gissis

10:30-10:45 Coffee Break & Exhibition Viewing - Hotel Hall and Balcony

10:45-11:45 **Poster Session 1 - Botanica Garden Hall**

Moderator: Chen Dubi

11:45-13:00	**Session 1 - Nuclear Reactors 1**	**Session 2 - Radiation Protection**
	Moderator: Shai Kinast	**Moderator: Favel Gov**
	Botanica Garden Hall	***G Level***
11:45-12:00	Measurements of the Flux Trap Effect in MTR Fuel Using Gamma Spectroscopy **Izhar Neder**	Evaluation of Public Exposure to Ionizing Radiation: UNSCEAR 2025 Report **Mikhail Balonov**
12:00-12:15	Ito-Langevin Process for Neutron Noise **Guy Gabrieli**	The Linear No-Threshold Model and Alternative Risk Models: Implications, Debates and the Regulatory Challenge **Favel Gov**
12:15-12:30	The Two Point Feynman-α Theory: a Practical Point Of View on Ex-Corq Detectors **Chen Dubi**	Dose Calculation Model for Narrow Beam **Yael Fried**
12:30-12:45	Neutronic Experiments During the Commissioning of the ETRR-2: Benchmark Calculations Revisited with OpenMC Code **Yuri Khodorkovsky**	FLUKA Evaluation of B4C Surface Coating for Minimizing Air Activation in the SARAF Phase II Target Room **Yevgeniya Korotinsky**
12:45-13:00	Catch 22 of Advanced Nuclear: Techno-Economics of SMRs and Gen IV Reactors **Danny Grossman**	Deterministic Effects to the Skin from Ionizing Radiation - a Recent Data Review **Orit Shmuel**

13:00-13:45	Lunch Break & Exhibition Viewing - Hotel Restaurant	
13:45-15:15	**Session 3 - Thermo-Hydraulics** **Moderator: Alex Rashkovan** ***Botanica Garden Hall***	**Session 4 - Radiation Protection and Environmental Risk Assesment** **Moderator: Lior Epstien** ***G Level***
13:45-14:00	The Study of Transient Heat Transfer Mechanisms and Two=phase Flow During Post Flow Instability Dryout Accident **Yosef Aharon**	Radiation Protection Aspects and Optimization of Spent Nuclear Fuel Transportation for Research Reactors **Roy Gross**
14:00-14:15	Numerical Study of Flow, Heat Transfer and Nucleate Boiling over a Wavy Wall **Einan Tal**	Patient and Medical Team Doses from Embedded Radioactive Fragments in Radiological Dispersal Device Scenarios **Rachel Hen Shukrun**
14:15-14:30	Characterization of Heat Transfer and Friction Coefficients ina a Closed Loop Thermosyphon Flow **David Saban**	Tungsten Based Materials Selection for Shielding and Balancing in the Medical and Nuclear Fields **Dov Chaiat**
14:30-14:45	Experiments and Modeling of Cooling Circles and Cooling Tower for Nuclear Reactors **Zohar Sahray**	Seismic Analysis of Non Structural Components Based on Observation Data **Stav Kontarovich**
14:45-15:00	Metal Ignition in Nuclear Fuel Channel **Elias Ezra**	Define Yamin Plain Wind Velocity Persistence and Long Term Correlations **Shay Moshel**
15:00-15:15	Three-dimensional Vortex and Gas Entrainment Numerical Analysis in Rotating Liquid Flow with a Free Surface **Shay-David Amar**	Advanced Nuclear Siting- New Opportunities in the Israeli Case Study **Ami Nagler**
15:15-15:30	Coffee Break & Exhibition Viewing - Hotel Hall and Balcony	
15:30-17:00	**Session 5 - Simulation & Numerical Methods** **Moderator: Erez Gilad** ***Botanica Garden Hall***	**Session 6 - Radiation Detection & Measurements 1** **Moderator: Alon Osovitsky** ***G Level***
15:30-15:45	Benchmarking of the SPERT-III E-core experiment with the Monte Carlo codes TRIPOLI-4, TRIPOLI-5 and OpenMC **Shai Kinast**	Low Level Activity Measurements of Am-241 in Environmental and Biological Liquid Samples Utilizing Liquid Scintillation Counter **Shai Cohen**
15:45-16:00	Simulating the Impact of Electrostatic Fields on Electron Beam Additive Manufacturing Processes **Itzhak Orion**	A System for the Detection and Quantification of Effluent Releases of Positron-Emitting Isotopes **Dimitry Ginzburg**
16:00-16:15	Development and Benchmarking of a Relativistic Point Detector in OpenMC **Itay Horin**	Advanced High-Sensitivity Multi-Layer Neutron Detectors Utilizing LiFZnS (Ag) Scintillators for Homeland Security Applications **Ilan Cohen Zada**
16:15-16:30	Comparison of Moment Closure and SDE Approximations of the Logistic Model **Eshed Magali**	Subdividing Scintillator-based Compton Cameras with Constant Readout Channels for Improved Spatial Resolution **Zohar Davidov**

16:30-16:45	Development of a 2D PWR Diffusion Model with Thermal Coupling for Control Optimization **Yuval Ben Galim**	Optimizing Silicon Passivated Implanted Planar detector for Alpha detection - Resolution Investigation **Eliran Evenstein**
16:45-17:00	Reactor Optimization by Reinforced Learning **Deborah Schwarcz**	

17:00-17:15 Israel Nuclear Society (INS) General meeting - Botanica Garden Hall

19:30-21:30 Dinner , Hotel Rooftop - Floor number 3

Thursday 27.3.2025

08:00-09:00 Registration, Reception and Exhibition - Hotel Lobby

09:00-10:30 **Plenary Session 2 - Botanica Garden Hall**

Moderators: Gustavo Haquin and Ilan Yaar

09:00-09:30 The Proton Radius Puzzle - Status and Perspectives
Guy Ron

09:30-10:00 Applying Nuclear Physics to Discover Atmospheric 14C Concentration Variations through the Archaeological Record: The Babylonian Destruction of Jerusalem
Elisabetta Boaretto

10:00-10:30 The Israel Institute for Fusion Research
Noaz Nissim

10:30-10:45 Coffee Break & Exhibition Viewing - Hotel Hall and Balcony

10:45-11:45 **Poster Session 2 - Botanica Garden Hall**

Moderator: Chen Dubi

11:45-13:00	**Session 7 - Chemistry, Materials Science & Nuclear Forensics**	**Session 8 - Safe Management of Radioactive Waste**
	Moderator: Erez Cohen	**Moderator: Ofra Klein Ben David**
	Botanica Garden Hall	***G Level***
11:45-12:00	Active Neutron Multiplicity Counting With A Non-Poissonian Interrogation Source **Chen Dubi**	Shallow Radioactive Waste Repositories and Surface Processes - importance and relevance **Noa Balaban**
12:00-12:15	Methods in Metallurgical-Mechanical Integrity Assessment of Irradiated Aluminum Reactor Components **Nissim Navi**	Challenges and Solutions for a Type-A Radioactive Waste Package Based on a Case Study **Irad Brandys**
12:15-12:30	Aerogel Spacer in Fission Tracks Detector From Star to Super-star Image Processing **Itzhak Halevy**	Thermal Model of Geological Disposal Concept for Radioactive Sealed Sources **Raz Chricker**
12:30-12:45	Resonant Raman Scattering in F-electron, Fluorite-Type Oxides **Tsachi Livneh**	Borehole Disposal of Radioactive Waste in Israel - Characterization program and Borehole **Ofra Klein-Bendavid**

12:45-13:00	Order-Disorder Transitions in Cerium and Praseodymium Hydrides, Manifested in Temperature-Dependent Raman Scattering Spectroscopy **Shahar Aziza**	Geopolymers as Immobilization Matrices for Cs-bearing Zeolites **Yarden Lior-Shain**
13:00-13:15	**Award for Outstanding Student Lectures – Botanica Garden Hall**	
13:15-14:00	Lunch Break & Exhibition Viewing – Hotel Restaurant	
14:00-15:15	**Session 9 – Nuclear Reactors 2** **Moderator: Izhar Neder** ***Botanica Garden Hall***	**Session 10 – Radiation Detection & Measurements 2** **Moderator: Adi Abraham** ***G Level***
14:00-14:15	Importance-Guided Evolutionary Optimization for Nuclear Reactor Core Fuel Management **Erez Gilad**	Improving Performance of PIPS Detectors using Advanced Characterization Techniques **Ohad Westreich**
14:15-14:30	Advancements in Cross-Section Homogenization for Rotating Control Drums in Microreactors **Erez Gilad**	Directional Detection of Multiple Gamma Sources Using Mutual Shielding of Scintillators **Nadav Ben David**
14:30-14:45	Energy Deposition Post-Shutdown in various components of the OPAL Reactor core **Nir Kastin**	MAXIMA-I A Coincidence System for Nuclear Decay Investigations **Sagi Nissim**
14:45-15:00	Temperature Measurement Using Fiber Bragg Gratings for a Nuclear Reactor Application **Shlomi Schneider**	Whole Body Counter Model Validation Using Monte Carlo Simulations **Lior Epstein**
15:00-15:15	Mathematical Foundation of the IFP Method **Ben Hatzofe**	Fast Neutron Detector Using $_{4}$He **Amir Broide**
15:15-15:30	Coffee Break & Exhibition Viewing – Hotel Hall and Balcony	
15:30-16:30	**Session 11 – Nuclear Physics** **Moderator: Guy Ron** ***Botanica Garden Hall***	**Session 12 – Radiation Therapy & Alpha DaRT** **Moderators: Lior Arazi and Ilan Yaar** ***G Level***
15:30-15:45	Structural Evolution of Even-Even and Odd-Mass Atomic Nuclei **Noam Gavrielov**	The Effect of Broad Nucleus Size Distributions in Diffusing Alpha-emitters Radiation Therapy **Yevgeniya Korotinsky**
15:45-16:00	Precision Measurement of the Charge Radius of Be-9 Through Muonic X-Ray Spectroscopy **Ofir Eizenberg**	Measurements of the Effective Diffusion Length of Ra-224 Decay Products in Healthy Tissues in Diffusing Alpha-Emitters Radiation Therapy **Lior Epstein**
16:00-16:15	The NEXT Search for Neutrinoless Double Beta Decay: Status and Prospects **Lior Arazi**	Combining Alpha-DaRT with Convection Enhanced Delivery for Improved Tumor Dose Coverage **Lior Epstein**
16:15-16:30	Advances in Topological Analysis for Background Reduction in Gaseous Time Projection Chamber Event Processing **Adam Redwine**	

Poster Session 1

Mor Ben Lulu	Validation of a MnO_2-Based Method for Simultaneous Detection and Quantification of Low Concentrations of Pb-210 and Ra-226 in Drinking Water Using Gamma Spectroscopy
Sutanu Bhattacharya	Neutron-Induced Reactions in a High Density Plasma at National Ignition Facility
Irad Brandys	Adaptive Real-Time Protective System for Critical Facilities and Infrastructures Against Blast Wave Loading
Raz Chricker	Development and Constructing a Thermal Conductive Measuring System for Soil Samples
Hanan Datz	Quick Sort Triage Critical Mission: Detecting Internal Exposure in Mass Radiological Emergency
Yael Fried	Radiological incidents and accidents involving mobile high activity sources
Nir Pour	Preliminary Study on the Colorization of Neutron-Induced Tracks in CR-39 Detectors
Yossi Salomon	Safety Critical Software Design Modular Architecture for Enhanced Reliability
Yossi Salomon	Outsourced Software Development: Strategic Risk Reduction for Software Systems
Daniel Satingher	Entangled charge carriers in LiF;Mg,Ti Traps/Luminescence Centers (TCs/LCs) - A Theoretical Approach
Yaniv Shaposhnik	The Ed Scale for Maintenance: A Comprehensive Framework for Evaluating and Prioritizing Maintenance Needs in Research Reactors
Igal M. Shohet	Resistance and Risk Assessment of Tunneled Smr Npp Exposed to Earth Penetrating Weapons' Hits in a Multi-Year Perspective
Rachel Hen Shukrun	Artifact Removal in Medical Imaging of Embedded Fragments Containing Different Radioactive Materials
Yeshayahu Weiss	Characteristics of the mechanisms in vertically counter-current liquid-gas flow, subjected to wall heat flux boundary condition
Shahar segal	Alpha particle identification using polymer detector
Yevgeniya Korotinsky	The Integration of Blender 3D Mesh Modeling and FLUKA Flair through Voxelization
Raphael Gonen	Electrodeposition and the problematic use of H2SO4 and HNO3, the traditional ingredients of electrolyte solutions
Doron Bitton	Experimental study of Critical Heat Flux temperature due to a rapid heating process at constant pressure

Poster Session 2

Rami Babayew	Fission Tracks Pattern Analysis and Properties Reconstruction: Advancing Nuclear Forensics using Classic Image Processing Algorithms
Mor Ben Lulu	A Combined Gamma Spectrometry and Proportional Counting Method for Sr-90 Quantification in a Mixed Sample: An ALMERA Proficiency Test Case Study
Mor Ben Lulu	Manual Correction of Gamma Contributions in Liquid Scintillation Counting: A Case Study with Quantulus GCT 6220
Mor Ben Lulu	PROCORAD Proficiency Tests A 10Year Review of Performance in Gamma-Emitter Detection and Quantification
Savion Braunstein	The Effect of Matrix Composition on Solidification Rate and Heat Generation of Geopolymers
Noam Elgad	Utilization of Deep Learning for Star Segmentation and Classification using Semi-Automated Adaptive Threshold methodology
Shahar Kravchik Valdarsky	High Complexity Maintenance Activities of the IRR2
Sagi Nissim	MAXIMA-II - A versatile Detection System for Trace-Level Radiation Analysis
Yaron Perets	Disposal of Nuclear Waste in Space Using Electromagnetic Accelerator Launchers
Nir Pour	Implementation of the DXT-RAD Dosimeter in the External Dosimetry Lab at SNRC
Ophir Ruimi	The Plasma Window for Enhanced Particle Beam Transmission from Vacuum to Atmosphere
Oriya Sabag	Comparison Between Semi-Insulating GaAs Alpha Radiation Detector with Schottky Anode Contact and P+ Anode Contact Layer Grown by MOCVD
Ronen Yavor	Cubic Ellipsoid Nuclear Model - a Link between Nuclear Structure and Atomic Properties
Rinat Levy	Maximum storage time period of urine samples for ICP-MS uranium analysis
Mor Ben Lulu	Addressing Challenges in Low-Energy Gamma Radiation Quantification for Almera Environmental Samples
Galit Bar	A New Adhesive Material Resistant to Ionizing Radiation

ABSTRACTS

Plenary Speakers Abstracts

Applying Nuclear Physics to Discover Atmospheric 14C Concentration Variations through the Archaeological Record: The Babylonian Destruction of Jerusalem

Elisabetta Boaretto

Weizmann Institute of Science

Reconstructing the absolute chronology of Jerusalem during the time it served as the Judahite Kingdom's capital is challenging due to its dense, still inhabited urban nature and the plateau shape of the radiocarbon calibration curve during part of this period. To overcome this problem we applied stringent field methodologies using microarchaeological methods in the excavation, leading to densely radiocarbon-dated stratigraphic sequences. With more than 100 dates we built a high resolution chronology to describe the development of Jerusalem in the Iron Age.

Using these sequences, we identified unexpected regional offsets in atmospheric 14C concentrations c. 720 BC, and in the historically secure stratigraphic horizon of the Babylonian destruction in 586 BC. We succeed to build a detailed high resolution chronology for the cultural remains associated to the end of Iron Age and shed light in the urbanistic development of the city in the Iron age.

Introduction to Fusion Energy and nT-Tao Compact Core Approach

Itay Gissis
nT-Tao Ltd. (VP R&D)

Thermonuclear fusion energy promises a limitless source of clean, abundant, and sustainable power on Earth. The pursuit of controlled fusion energy has spanned over 80 years, driven by extensive government and academic research efforts. In the past decade, the private sector has increasingly entered the fusion landscape, aiming to harness emerging technologies and accelerate the path towards fusion power. nT-Tao is a startup company founded in Israel with a vision of creating a commercially viable fusion reactor. nT-Tao approach to fusion is of "long" pulse magnetic confinement which aims at a plasma regime which is midway between traditional magnetic confinement fusion (MCF) and inertial confinement fusion. Namely, density of , temperature of and energy confinement time of . The pulsed reactor should operate at and produc.

The relatively high density enables lower plasma volume - hence the "compact" core. Nevertheless, heating dense plasma requires orders of magnitude more power compared to traditional MCF systems. The heating is enabled by innovative heating techniques utilizing pulsed power generator and power electronics. The confinement is obtained by using advanced Stellarator design with dynamic stabilization techniques. In the talk I will introduce the company physical concept of the compact core pulsed reactor. I will present Stellarator design simulations, heating mechanisms design and testing, and diagnostics development. Finally, I will present the current stage of prototype C-2A and the company R&D roadmap towards commercialized fusion.

The Israeli Institute for Fusion Research

Noaz Nissim

Nuclear fusion, as a source of clean energy, offers advantages that ensure sustainability and a secure supply: the fuels are widely available and virtually limitless, there is no greenhouse gas production, and it is intrinsically safe due to the absence of risks associated with an uncontrolled chain reaction. With the appropriate selection of materials for the reactor's structure, the radioactivity of the building materials is expected to diminish within a few decades, and they may even be reused in a new reactor. Research and development of fusion for energy production have been underway worldwide since the 1950s. The two main contemporary fusion research projects are ITER (initially the International Thermonuclear Experimental Reactor, where "iter" means "the way" or "the path" in Latin), an international collaboration involving 35 countries under construction in the south of France. ITER is a TOKAMAK-type magnetic confinement reactor designed as a technological demonstrator for the combustion of DT (Deuterium-Tritium) fuel.

The National Ignition Facility (NIF) at the Livermore research center in the USA is another major project conducting research on fusion energy production using inertial confinement with the help of a high-energy laser. The NIF laser comprises 192 beams generating approximately 2 MJ of laser energy in a few tens of nanoseconds, all hitting a target containing DT fuel simultaneously for uniform heating. Both projects are funded with budgets in the order of tens of billions of dollars. In addition, numerous university-scale research projects, and about 40 private companies are involved in fusion research worldwide. Despite the extensive global efforts in fusion research, Israel has not formally participated in any of the major initiatives.

While many countries boast large infrastructures facilitating research on the scientific front of hot plasmas, providing platforms for training generations of scientists in the practical and theoretical aspects of fusion physics, Israel lacks an organized training program on the subject within its universities. The goals of the institute are to establish an Israeli knowledge center on nuclear fusion for energy purposes and hot plasmas, ensure solid support for research activities covering all scientific and technological aspects of hot plasma and nuclear fusion, promote research providing basic data essential for advancing nuclear fusion applications and plasma science, and foster collaboration between academic research bodies and industry on issues related to nuclear fusion applications for energy needs. The institute also aims to train the future generation of scientists specializing in fusion for energy purposes.

State of the Art in Internal Dosimetry

François Paquet

Deputy Director of research and expertise in the environment, French Authority for Nuclear Safety and Radiation Protection; ICRP Committee 2 Vice-Chair, ICRP Task Group on Internal Dose coefficients Chair

Internal dosimetry is a discipline that brings together a body of knowledge, tools and procedures for calculating the doses received after radionuclides have been incorporated into the body. Given the complexity of dose calculation procedures, the International Commission on Radiological Protection (ICRP) provides dose coefficients (CED) that can be used to rapidly define committed effective doses, just from knowledge of the intake or of the radionuclides measured in bioassays.

A considerable effort has been made in recent years to update all the tools used to calculate doses after incorporation: biokinetic models, which describe with great precision the behavior of radionuclides in the body, have been updated with the latest data from the scientific literature; nuclear decay data have been revised to take into account about 1,250 of the most common isotopes; mathematical phantoms, representing human anatomy, have been replaced by extremely realistic voxel phantoms, soon to be replaced by MESH phantoms offering unrivalled precision for calculating energy deposition in sensitive tissues and cells; finally, tissue weighting factors wT and radiation weighting factors wR have also been revised in line with the latest epidemiological and radiobiological data. All this knowledge has been published in various ICRP publications, leading to updating dose coefficients for workers (ICRP 2015, 2016, 2017, 2019, 2022) and members of the public (ICRP, In Press). These new coefficients represent a real step forward, as they are based on the best scientific knowledge available and are currently being deployed in most countries around the world for use in radiation protection, i.e. justification, optimization and limitation of exposures.

Despite all these progresses, CED do not meet all requirements, particularly when there is a need to assess the individual risk resulting from exposure. Although effective dose is linked to the risk, CED are calculated for reference persons who are exposed to reference situations that may be very different from the reality. This is of little importance when doses are very low, but can be more problematic, particularly in medicine, where doses can be moderate to high and delivered to patients suffering from various pathologies, and who are therefore very different from the ICRP reference men and women.

Much work remains to be done in several areas of internal dosimetry, to take into account different anatomies and physiologies, new radiopharmaceuticals, and to develop specific tools that will ultimately allow us to move toward increasingly personalized dosimetry.

The Proton Radius Puzzle - Status and Perspectives

Guy Ron

The proton, one of the fundamental building blocks of matter, has long been thought to be well understood in terms of its charge radius. However, precise measurements using different experimental techniques—electronscattering,hydrogenspectroscopy,andmorerecently,muonichydrogenspectroscopy—have revealed inconsistencies in the extracted proton charge radius, leading to what is now known as the proton radius puzzle. The unexpected discrepancy between the radius measured using different methods challenges our understanding of nucleon structure, analysis methods, and possible beyond-Standard-Model physics.

I will review the experimental methods used to determine the proton charge radius, discuss the theoretical frameworks involved in the interpretation of these measurements, and explore potential resolutions to the puzzle. Recent experimental results, including new scattering and spectroscopy data, will be examined. Finally, I will discuss ongoing and future efforts to resolve this discrepancy.

Session 1 – Nuclear Reactors 1

Moderator: Shai Kinast

Measurements of the Flux Trap Effect in MTR Fuel Using Gamma Spectroscopy

I. Neder[1,*], H. AbuzIf[2], G. Gabrieli[1], U. Steinitz[1], Z. Yungrais[1], O. Aviv[1], K. Barda[1], I. Iluz[1], A. Krakovich[1], E. Gilad[2]

1 Soreq Nuclear Research Center, Yavne 818000, Israel
2 The Unit of Nuclear Engineering, Ben-Gurion University of the Negev
Corresponding author: *izharne@soreq.gov.il

An accurate estimation of the Power Peaking Factor (PPF) is a key ingredient in planning, commissioning, and maintaining the operational lifecycle of nuclear reactors. The PPF is known to significantly increase in the presence of water gaps in the core, that serve as local thermal flux traps and induce fissions in the traps' surrounding. Reliable prediction of this effect is computationally challenging as it strongly depends on local core features such as fuel depletion distribution and precise geometrical modeling. Thus, experimental validation of computed PPF allows a better estimation of the calculation errors.

Here we report a high-resolution (~3mm) surface scan of the power density in MTR fuel assemblies near water gaps, using gamma spectroscopy analysis of short-lived fission products that were performed in the Israeli Research Reactor – 1 (IRR-1). The first experimental campaign used burned fuel that was re-irradiated in the core for a few hours. The experimental results were compared with detailed high-resolution full-core 3D Monte Carlo calculations. In the second experimental campaign, we used a fresh MTR fuel assembly that was irradiated with optimized core geometry that increased the PPF effect, for benchmarking reactor calculations. Spectroscopic gamma measurements, performed along and across the fuel assembly, included several emission lines with different energies and therefore different penetration depths into the fuel assembly. This feature thus allows for a partial 3D mapping of the power density distribution in the fuel assembly at the time of irradiation in the core. Results of the power distribution showed good agreement with initial calculations, specifically for an enhanced PPF effect of up to a factor of 1.58 due to the flux trap. KEYWORDS: Flux Trap, Power Peaking Factor, Fission product Gamma Spectroscopy, Nuclear Reactor Calculations

Ito-Langevin Process for Neutron Noise

Guy Gabrieli, Yair Shokef, Izhar Neder

Tel Aviv University

We derive an Ito-Langevin stochastic process that captures the time-dependent deviation from Poisson behavior of the noise detected from a general heterogeneous sub-critical neutron system. Using the probability generating function for the actual physical process, we deduce the super-Poisson deviation of the covariance matrix of counts at the detector due to neutron multiplication upon fission. This leads to a general form that coincides with the second moment of an Ito process. This comparison facilitates the formulation of a corresponding effective Langevin equation, which potentially enables simulations that significantly reduce the computational resources required compared to direct simulation of the system's actual noise. This method could assist in designing sub-critical noise experiments for licensing new research reactors, for improving cross-section libraries and for non-destructive assays of spent fuel.

The Two Point Feynman-α Theory: A Practical Point of View on Ex-Core Detectors

C. Dubi, E. Magali
Ben-Gurion University

The Feynman-α method is a widely used realization of the so-called "reactor noise" theory, where static and kinetic parameters of the core are estimated by sampling statistical properties of the neutron count distribution in a critical or subcritical configuration. In the Feynman- α method, the variance-to-mean ratio (as a function of the detection gate) is sampled, and then the α eigenvalue is estimated through a standard fitting procedure. The theory behind the Feynman-α method relies on a single-group analysis.

From a practical point of view, the single group model requires that the detector be located within or next to the reactor core. Implementation of the Feynman-α method is simple and robust due to three facts: first, although the dynamics are determined by (at least) 5 parameters, the fit is done only for a two-parameter function. Second, these parameters are well separated: one is a constant multiplier and the second is an exponential coefficient. Third, the exponential coefficient has a clear and simple physical interpretation, which can be easily used to estimate the reactivity of the core. In the past decade, the classic Feynman-α theory has been extended to a multi-group setting, using the probability generating function formalism.

However, in the resulting formulas, it seems, the above mentioned properties are often lost: implementation would require a fit on a multi-exponential function, whose decay modes are defined by the eigenvalues of a certain "reaction rate" matrix, which may not be explicitly computed, and would depend on parameters that can not be calibrated in a simple manner. The present study introduces a simple two-group model, for two distinct spatial regions: the core region and the moderator/reflector region. It assumes that the detector is located outside the core, within the moderator/reflector region. Through direct analysis of the reaction rate matrix, we address the practical applications of the two-point Feynman-α theory: when should we expect a good "separation" between the different decay modes, and when would the reactivity be tractable from standard fitting procedure. This study starts with the theoretical derivation, then we first conduct a numeric study to verify the conditions for applying the two region model, and second we use the two region model to revisit Ex-Core noise experiments conducted an the IPEM/MB-01 and the CROCUS reactors.

Neutronic experiments during the commissioning of ETRR-2: Benchmark calculations revisited with OpenMC code

Y. Khodorkovsky, N. Kastin, E. A. Villarino

The Egyptian 2nd Training and Research Reactor (ETRR-2), also called the Multipurpose Reactor (MPR), was built by the INVAP company of Argentina. The constructions began in 1990 and the reactor went critical for the first time on November 1997 [1-2]. During the next months, several neutronic experiments were conducted with different core configurations. In particular, different core configurations, containing growing numbers of beryllium reflectors were built, finally loading the in-core cobalt irradiation device on February 1998.

The neutronic experiments performed included: control plate (CP) worth calibration using the asymptotic period method; shutdown margin measurement using the rod drop method; neutron flux mapping in water between the fuel plates using gold wires activation method. The results of these experiments were included, together with the core specifications, as part of the IAEA coordinated research project (CRP) for benchmarking computational tools, applied to research reactors [3].

OpenMC is a modern state-of-the-art Python and C/C++ -based free open-source Monte Carlo code, capable of modelling neutron and photon transport for criticality, as well as fixed source problems [4]. In this work, the ETRR-2 core was modelled with OpenMC, using the data included in the international benchmark [5-7], with ENDF/B-VIII.0 cross sections database.

The critical states of each core configuration with different CP positions were calculated and compared with the experimental data. Two details in the model, that were not clear, or missing from the original data, were found important to obtain the critical states with as small bias from criticality as possible. First, the relative bias between the calculated critical states was reduced from 250 to 150 pcm by choosing the most appropriate model for the CP geometry. Second, the absolute bias from k=1 was reduced by 150 pcm by introducing the correct amount of equivalent boron content (EBC) that represents the neutron absorbing impurities in aluminium. Using the best available models for the different cores, differential rod worths, shutdown margins and reactivity excesses were now calculated and compared with the experimental results. Finally, thermal neutron fluxes in specific places inside water channels were computed.

In general, the results for the critical states are not worse than these of calculations performed during the design and commissioning by the INVAP company [8]. Moreover, they improve in absolute bias when using the correct impurities in aluminum. The statistics of our results for the critical states of core SU-29-2S0 is better than the one of SNRC [9], and it improves in the absolute bias also because of the correct amount of impurities in aluminum.

The differential and the total reactivities of CPs compare well to experiments for the final core configurations (1/98 and 2/98), and to the old INVAP results. The average relative deviations are bound by 15% for these cores, but may be up to 45% for the initial configurations (SU-29 and SU29-2S0). The published calculations of SNRC [9] and of NECSA [10] are only for CR-5 calibration in core configuration SU-29-2S0 and the deviations from experimental data are similar to INVAP's and to ours - the total CR-5 reactivity deviation is bound by 15%.

Preliminary results of the thermal neutron fluxes are also presented.

Catch 22 of Advanced Nuclear: Techno-Economics of SMRs and Gen IV Reactors

Danny Grossman, Ami Nagler

Small modular reactors (SMRs) and Generation IV reactors offer the potential for significant improvements in safety and siting, as well as lower project costs and lower project risk. 98 projects are currently in various stages of development, and recently, big tech has invested billions in multiple projects and companies.

Since no SMRs have been built in the West so far, the billion-dollar question is: What will the cost of SMRs and advanced nuclear be, and will they be competitive in the energy market? There is a large body of literature on the expected cost of SMRs. This literature mainly focuses on the negative economy of scale compared to mass production and learning curve cost reductions.

In this work, we explore several of the above assumptions vs. the historical data- for example: where and how do we see scaling benefits (spoiler: nearly nowhere). Using these insights, we contrast several SMR company statements with long-term estimations and bottom-up cost models to identify critical cost drivers of small vs. large nuclear reactors. Results show that technology selection and optimized size can be vital for economically competitive nuclear power plants. We also show that opex and fuel costs are much more important in small nuclear builds.

Session 2 – Radiation Protection

Moderator: Favel Gov

Evaluation of Public Exposure to Ionizing Radiation: UNSCEAR 2025 Report

M. Balonov[1], H. Grogan[2], Ph. Steinman[3], W. Ringer[4], C. Robinson[5], T. Cabianca[6], V. Berkovskyy[7,8], C. Lawrence[9], R. Michel[10], B. Napier[11], and M. Zimmermann[6]

1 Consultant, Israel; email: balonovmi@gmail.com
2 Cascade Scientific, UNSCEAR Quality Assurance Lead Writer, USA
3 Federal Office of Public Health FOPH, Switzerland
4 Austrian Agency for Health and Food Safety, Austria
5 Norwegian Radiation and Nuclear Safety Authority, Norway
6 UNSCEAR secretariat, Austria
7 Ukrainian Radiation Protection Institute, Ukraine
8 National Research Center for Radiation Medicine, Ukraine
9 Australian Radiation Protection and Nuclear Safety Agency, Australia
10 Consultant, Leibniz University Hannover, Germany
11 Consultant, USA

Since the establishment of the United Nations Scientific Committee on the Effects of Atomic Radiation (UNSCEAR) by the UN General Assembly in 1955, the mandate of the Committee has been, inter alia, to undertake broad reviews of the sources of public exposure to ionizing radiation and of the associated radiation doses. Exposure of the public from natural and human-made sources is an important topic that the Committee has evaluated since 1958 and regularly updated. The aim of this scientific evaluation launched in 2020 is to review the latest scientific evidence and literature since 2007 regarding sources and levels of public exposure to ionizing radiation from natural and human-made sources and prepare an update to the previous UNSCEAR reports. This update based on data provided by 61 UN Member States and compiled from published peer reviewed literature and international organizations has been approved by the Committee in 2024. Quality criteria have been established to promote consistency in the review process. The basis for estimation of annual effective dose in the population globally or regionally is the calculation of external and internal dose (inhalation, ingestion) from results of monitoring or modelling of the living environment (dose rate, radionuclide concentration in the air, food and drinking water) obtained from the data review.

The doses reported are characteristic doses to particular population groups and their variability reflects the variability in environmental radioactivity and the different exposure situations. The range of average annual effective dose to the public from natural radiation sources was estimated to be 1–14 mSv whereas the average worldwide effective dose was estimated to be around 3.0 mSv. The major contribution (60%) is from inhalation of radon, thoron and their decay products, which represents about 1.8 mSv. The ingestion of uranium and thorium series radionuclides and potassium-40 represents a smaller contribution of around 0.5 mSv. External exposure to terrestrial radionuclides and cosmic radiation contribute 0.40 mSv and 0.30 mSv, respectively. While the average annual worldwide effective dose estimate has increased from 2.4 mSv, when compared to previous reports, this change does not reflect an actual change in public exposure. It reflects methodological improvements and a greater diversity in the data available from different locations and regions that were not available for previous Committee's estimates. Compared to natural sources, exposure of the public from human-made sources is generally lower, except in the rare situation of major accidents. Exposures to the public due to nuclear power production have been evaluated by means of discharge information and the assessment methodology from the UNSCEAR 2016 Report, with some minor modifications. Estimated annual doses to members of the public generally do not exceed a few tens of μSv. The worldwide collective effective dose per unit electricity generated was estimated. Analysis of data on public exposures from other applications of sources of ionizing radiation, (e.g., medical, industrial, and research applications, and the use of consumer products) concluded that average worldwide annual doses from those sources are from a few to several hundred μSv. Such exposures, however, affect a large fraction of the world population. The estimates of past and current public exposure at nuclear weapons test sites have been updated at New Mexico, USA, Marshall Islands, Mururoa, and Fangataufa, French Polynesia and Semipalatinsk, Kazakhstan. Past exposures at many of these sites were estimated to have been well above natural background levels, immediately following the tests. However, continuing public exposures at these sites are generally much lower than those from natural background. Public exposure relating to the legacy of other military applications of nuclear and radioactive material, i.e., nuclear weapons production, maintenance and decommissioning, are generally negligible except for the radiological consequences of major accidents. The Committee has previously published detailed reports relating to the accidents that occurred at the Chornobyl NPP in 1986 and the Fukushima Daiichi NPP in 2011. There has been a continuous reduction of radionuclide levels in soil, air, water bodies, vegetation, and foodstuffs due to radionuclide decay and migration within ecosystems and due to environmental countermeasures in the affected areas. Current annual doses to the public residing in the areas of Belarus, Russian Federation and Ukraine surrounding the Chornobyl NPP, range from tens of μSv to 1 - 2 mSv. In the area of the Fukushima Daiichi NPP, current annual doses to residents in non-evacuated municipalities range from a few μSv to 0.3 mSv.

The Linear No-Threshold Model and Alternative Risk Models: Implications, Debates and the Regulatory Challenge

Gov Favel

PhD, NLSO Former Head

Radiation protection policies worldwide have largely relied on the linear no-threshold (LNT) model, which assumes a direct relationship between radiation dose and risk, even at low levels. This paper examines the scientific basis of the LNT and explores alternative risk models in light of evolving scientific understanding. The paper include a review of empirical studies, theoretical critiques, and case studies to assess the implications of model selection for public health, regulatory policies, and socioeconomic costs. The analysis includes evidence from high background radiation areas, the impact of LNT-based interventions following nuclear accidents, and the potential benefits of considering hormetic effects. A key challenge arises from the LNT's assumption that any exposure carries some risk, potentially leading to a perception of hazard that exceeds the actual magnitude of risk at low doses. This perception can conflict with the principle of a graded approach to regulation, where regulatory effort is proportionate to the assessed risk. This conflict and its implications for regulatory practice are discussed.

Background: The Linear No-Threshold (LNT) hypothesis posits that the risk of ionizing radiation is directly proportional to the dose, with no threshold below which the risk is negligible. Originating from Hermann Muller's 1946 Nobel Prize lecture [1], the LNT model has become the cornerstone of radiation protection policies worldwide. Its mathematical simplicity and applicability have contributed to its widespread adoption. However, this model's validity and universality have been questioned, sparking intense scientific debate over alternative risk models. This paper explores these models and highlights the implications of their adoption, using recent literature and case studies.

Methods: Key studies from 2020 to 2024 were analyzed to assess empirical evidence, theoretical critiques, and policy implications. The research integrates data from regions with high natural background radiation and scrutinizes the ethical dimensions of radiation protection policies.

The LNT Model and Its Foundations

The LNT hypothesis is rooted in the Life Span Study (LSS) of Hiroshima and Nagasaki A-bomb survivors. However, critiques argue that exposure doses in the LSS were underestimated due to residual radiation from radioactive fallout ("black rain") [8]. This underestimation undermines the LNT model's validity, especially for low-dose radiation (LDR), which may exhibit hormetic effects, such as reduced risks of age-associated diseases (e.g., Alzheimer's, Parkinson's,
and cancers) [6].

Critiques of the LNT Model:

1. Empirical Challenges: Data from high natural background radiation regions, such as Kerala (India) and Ramsar (Iran), show no detectable increase in cancer incidence, despite significantly higher radiation levels [9].
2. Policy Implications: The Fukushima Daiichi Nuclear Power Plant accident illustrates the socio-economic costs of strict LNT adherence. The evacuation caused more harm than the radiation itself [8].
3. Scientific Oversights: The LNT model prevents the exploration of hormetic therapies, potentially delaying advancements in medical treatments forchronic diseases [2].

Alternative Risk Models:

The critique of the LNT hypothesis has led to the exploration of alternative risk models, each with unique implications:

1. Linear with Threshold (LT): Suggests a dose below which there is no significant risk. This model aligns with empirical observations in low-dose exposure studies [3].
2. Superlinear: Proposes higher-than-expected risks at low doses. While rare, this model emphasizes caution in radiation exposure policies [4].
3. Sublinear: Indicates diminished risk at lower doses compared to linear predictions, suggesting that current regulations might overestimate low-dose risks [1].
4. U-Shaped: Demonstrates a risk reduction at low doses, followed by an increase at higher doses. This aligns with hormetic principles, where low doses may stimulate protective biological responses [6].
5. Hormesis: Posits that low-dose radiation is beneficial, triggering adaptive responses that improve overall health. This model challenges traditional risk assessment paradigms but lacks broad regulatory acceptance [5].

Discussion:

Model Selection and Policy Implications

The choice of risk model significantly influences radiation protection policies and public health outcomes. For example, European indoor radon studies reveal that model choice affects the calculated detriment attributable to radon exposure, emphasizing the importance of accurate risk assessment methods [4].

Ethical Considerations

Calabrese et al. [2] argue that blind adherence to the LNT model raises ethical concerns, especially when evidence supports alternative models. Misaligned policies based on LNT may result in unnecessary socioeconomic burdens and hinder scientific progress.

ICRP Position

The International Commission on Radiological Protection (ICRP) continues to support the LNT model as a precautionary framework for radiation protection. The ICRP emphasizes that the LNT model serves as a practical tool to minimize risks in the absence of definitive evidence for alternative models, underscoring the need for continued research and dialogue in this field.

The Graded Approach: A Core Principle

The graded approach is fundamental to how regulators operate. It means that the level of regulatory scrutiny, resources invested, and safety measures implemented are proportionate to the assessed risk. This principle is applied across various industries, not just radiation protection.

LNT and the Perception of Risk

The LNT model, by assuming any exposure carries some risk, can lead to a perception of hazard that may not align with the actual magnitude of risk at low doses. This presents a challenge for regulators because:

- Public Perception and Fear: The LNT reinforces public fear of any radiation exposure, even at very low levels. This can lead to demands for extremely stringent (and costly) regulations, even when the actual risk is negligible.
- Resource Allocation: If all radiation exposure is treated as equally hazardous, it can lead to misallocation of resources, with excessive focus on minimizing tiny risks while potentially neglecting more significant hazards.

3. How Regulators Deal with the Tension

Regulators employ several strategies to reconcile the LNT with the graded approach:

- ALARA Principle: The "As Low As Reasonably Achievable" (ALARA) principle is a key tool. It recognizes that while any exposure carries some risk (as per LNT), it's not always practical or necessary to eliminate every last trace of radiation.
  ALARA seeks to minimize exposures to levels that are reasonably achievable, considering economic and social factors.

- Dose Limits and Exemptions: Regulators set dose limits for occupational and public exposure, based on the LNT but also considering practical constraints. They also define exemptions for very low-level exposures that are considered trivial. This helps to avoid excessive regulation of minimal risks.
- Risk-Informed Decision Making: Regulators are increasingly moving towards risk-informed decision making, which involves a more comprehensive assessment of risks, considering both the probability and consequences of different scenarios. This allows for a more nuanced approach than simply relying

- Ongoing Research: Regulators should support and encourage research into low-dose radiation effects to improve scientific understanding and inform future policy decisions. This acknowledges the limitations of the LNT and the need for more refined risk assessment models.

Conclusions: This paper does not advocate for any specific risk model but highlights the profound implications of model selection. As radiation science evolves, revisiting foundational assumptions and embracing evidence-based approaches is essential for advancing public health, policy-making, and scientific innovation. Regulators are aware of the limitations of the LNT and the potential for it to lead to an overestimation of risk at low doses. They address this by employing the graded approach, using tools like ALARA, dose limits, or risk-informed decision making. While the LNT remains a cornerstone of radiation protection, regulators are constantly seeking to refine their approaches based on the latest scientific evidence and a balanced consideration of risks, benefits, and societal values.

Dose Calculation Model for Narrow Beam

Fried Y., Oren Y., Shukrun R.H., Ben-Shlomo A. and Epstein L.

As part of the safety assessments of a radiation facility, it is necessary to calculate the dose rates around a linear accelerator. The advantage of a linear accelerator is the ability to use beams of varying energies and shapes. The shape of the beam requires special attention when calculating dose rates, and affect the necessary safety protocols and shielding requirements.

Conventional methods for shielding design and dose calculations are suitable for broad beams (as published by the NCRP and IAEA). The IAEA and NCRP methodology follows the inverse square law and take into account the attenuation in the walls, the buildup, occupancy and use factors, but when we compared the dose rates calculated by these methodologies to dose rates calculated by Monte Carlo simulations, we could not reproduce the simulations results. We found that these methods are not suitable for very thin fan beams.

We discovered that the very thin width of the beam causes unique effects, different to the behavior of broad beams:

1. The Inverse-square law cannot be applied correctly when calculating dose rates from narrow beams.
2. The reported TVL values in the literature are applicable to broad beams, and take the buildup and scattering inside the shielding into account. In narrow beams the scattering inside the shielding is different and the broad beam TVLs do not apply; using the reported TVL values would result with an overestimation of the dose rates.

In our work, we propose a new model for dose rate calculations for narrow beams that considers their unique behavior. We used our model to calculate the expected dose rates for several selected cases with different shielding designs and validated the model against Monte Carlo simulations using the FLUKA Monte Carlo code. Finally, we present TVLs for narrow beam in different materials.

FLUKA Evaluation of B4C Surface Coating for Minimizing Air Activation in the SARAF Phase II Target Room

Y. Korotinsky, L. Epstein, I. Eliyahu, R.H. Shukrun, M. Brandis

Background: The Soreq Applied Research Accelerator Facility (SARAF) is a linear accelerator designed to accelerate proton and deuteron beams toward a liquid Gallium-Indium target. Upon impact at the target, fast neutrons with energies reaching 47 MeV are produced. One Ga-In target is situated within a dedicated target room, constructed primarily from concrete, that encompasses an air volume of ~30 m3. Neutrons emitted from the target scatter within the room and are moderated by interactions with the concrete walls, floor, and ceiling. A fraction of these scattered neutrons is reflected back into the room, with a lower energy spectrum that includes thermal and epithermal energies. These neutrons produce significant activation of the air within the room.

Purpose: A critical aspect in the facility'sradiation safety design is the activation rate of air within the target areas. This is mainly to ensure worker safety and to protect against the release of radioactive air into the environment. This study assesses the air activation inside the room and the effect of coating the surfaces of the room with Boron Carbide (B4C), as a technique to mitigate the accumulation of activation products generated by thermal neutron interactions.

Methods: The FLUKA Monte Carlo code was employed to simulate neutron transport and the geometry of the room, aiming to estimate the activity concentrations of selected air activation products. An in-depth spectral analysis was carried out on both the incident and reflected neutron energies. Different configurations of B4C surface coatings were examined and compared.

Results: Our findings indicate that using B4C coating, regardless of the configuration, decreases the activity concentration of 41Ar and 14C by at least an order of magnitude. Expanding the coating to additional surfaces (from four to five) decreases the concentration by a factor of 1.6 to 2.5. In contrast, enhancing the coating thickness from 0.5 to 5 cm has a negligible impact.

Discussion and Conclusions: Applying a B4C surface coating is notably successful in decreasing the activity concentration of isotopes generated by thermal and epithermal neutrons. Considering the comparably small benefit of coating five surfaces rather than four, and the negligible effect of coating thickness on the concentrations of 41Ar and 14C in the air, we recommend employing the most feasible, economical and structurally robust coating arrangement. Introduction of B4C coating does not alter the air concentration of other activation products formed by interactions with high-energy neutrons. Thus, reducing their concentrations necessitates alternative strategies such as room air ventilation (during and after irradiation) combined with appropriate cooling timesto allow decay over several half-lives before room entry or air release.

Session 3 - Thermo-Hydraulics

Moderator: Alex Rashkovan

The study of transient heat transfer mechanisms and two-phase flow during Post Flow Instability Dryout Accident

A. Chakmon, G. Ziskind and Y. Aharon

The present work describes a transient computational code for prediction of the heat transfer regimes and the channel wall temperature during a channel transient heating. An experiment in water flow inside a stainless steel tube, 1 m long and 8.3 mm in diameter, was used to validate the model. The heated channel was connected in parallel to a large bypass to simulate redistribution of the flow due to Onset of Significant Void (OSV). During the experiment, the flow rate, the channel power and the local channel wall temperature were continuously measured. The model is based on correlations from the literature for each heat transfer regime, in the single and two phase flow zones, and conservation equation on each axial segment along the channel. The Knoebel Critical Heat Flux correlation was used for distinguishing between pre- and post-CHF zones, where a film heat transfer correlation was used. A new correlation is proposed for the post-CHF regime based on the calculated void fraction in that zone. An over-prediction of the model was obtained in the single phase calculations, whereas in the two phase zone a good agreement was obtained for the temperature values and trend.

1.Introduction: In reactors safety analysis, one of the accidents which are always analyzed is the Loss of Flow Accident (LOFA). That accident is caused by Station Blackout (SBO) or primary coolant pump locked rotor. In the first sequence, when the reactor was de-energized, the pumps immediately began to cost down and the flow rate through the fuel channels begins to decay. In a very short time, during that flow reduction, shut down of the reactor power takes place and the safety of the fuel element is assured. In the second sequence, the flow through the main pump stops almost immediately. In that case, the flow rate through the reactor core is immediately decreased, proportionally to the influence of each pump on the total flow rate. The reactor continues to operate in a full power for a short period of time, with a reduced flow rate, and then shut down occurs. Those thermohydraulic conditions may lead to Onset of Flow Instability (OFI) in the reactor core and redistribution of the flow rate between the cooling channels, which may lead to burnout of the fuel element. Analysis of the channel cooling during that period is important in the safety analysis of the reactor.

In the present work, an analytic model was derived to evaluate the fuel element wall temperature in transient conditions during a partial loss of flow scenario. The model is based on various correlations from the literature for the void fraction and the heat transfer and conservation equations of the channel. A transient heating experiment of water flow inside a stainless-steel tube was used for validation of the model and that was the geometry on which the model was written.

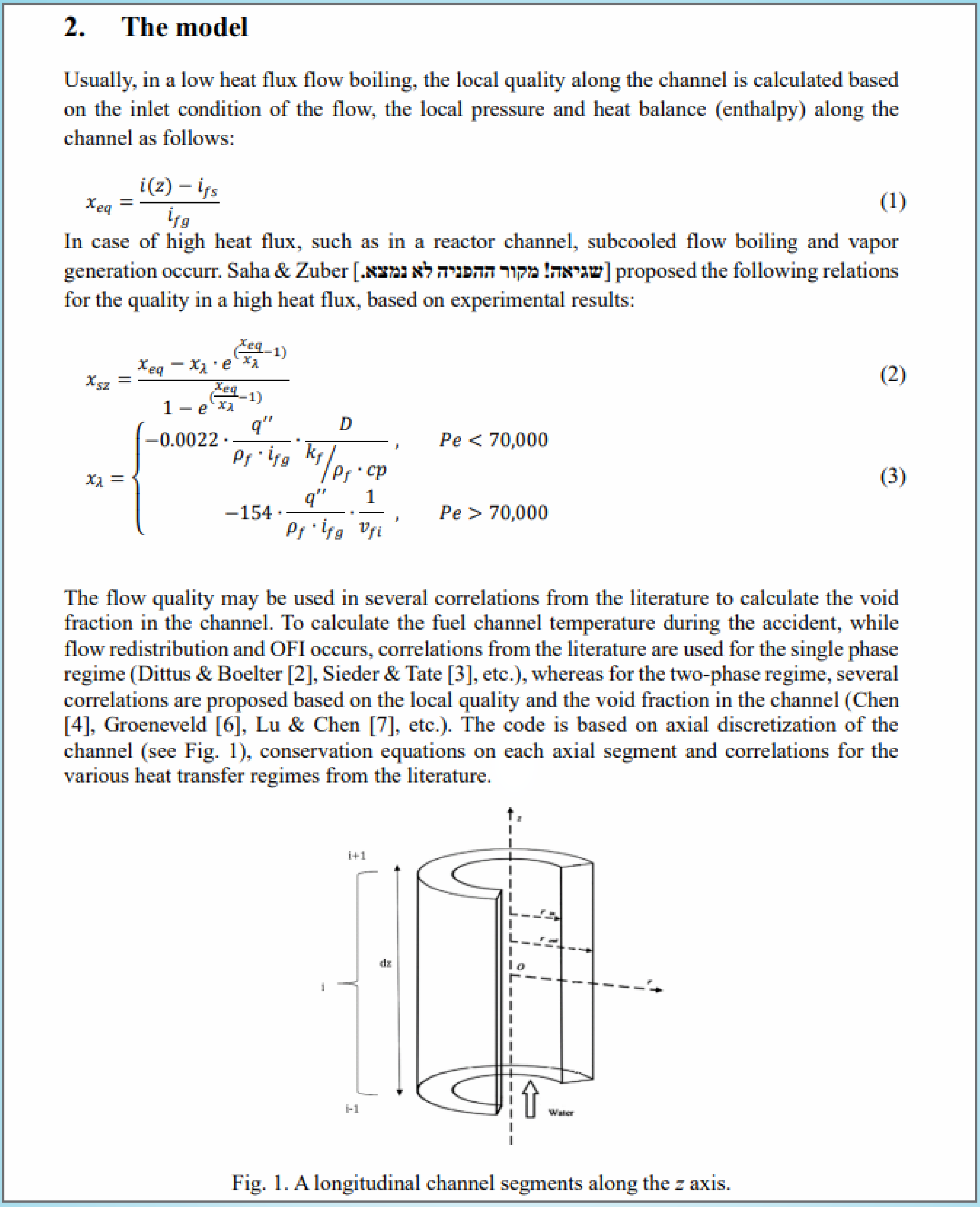

2. The model

Usually, in a low heat flux flow boiling, the local quality along the channel is calculated based on the inlet condition of the flow, the local pressure and heat balance (enthalpy) along the channel as follows:

$$x_{eq}=\frac{i(z)-i_{fs}}{i_{fg}} \tag{1}$$

In case of high heat flux, such as in a reactor channel, subcooled flow boiling and vapor generation occurr. Saha & Zuber [שגיאה! מקור ההפניה לא נמצא.] proposed the following relations for the quality in a high heat flux, based on experimental results:

$$x_{sz}=\frac{x_{eq}-x_{\lambda}\cdot e^{\left(\frac{x_{eq}}{x_{\lambda}}-1\right)}}{1-e^{\left(\frac{x_{eq}}{x_{\lambda}}-1\right)}} \tag{2}$$

$$x_{\lambda}=\begin{cases}-0.0022\cdot\dfrac{q''}{\rho_f\cdot i_{fg}}\cdot\dfrac{D}{k_f/\rho_f\cdot cp}, & Pe<70{,}000\\[2ex] -154\cdot\dfrac{q''}{\rho_f\cdot i_{fg}}\cdot\dfrac{1}{v_{fi}}, & Pe>70{,}000\end{cases} \tag{3}$$

The flow quality may be used in several correlations from the literature to calculate the void fraction in the channel. To calculate the fuel channel temperature during the accident, while flow redistribution and OFI occurs, correlations from the literature are used for the single phase regime (Dittus & Boelter [2], Sieder & Tate [3], etc.), whereas for the two-phase regime, several correlations are proposed based on the local quality and the void fraction in the channel (Chen [4], Groeneveld [6], Lu & Chen [7], etc.). The code is based on axial discretization of the channel (see Fig. 1), conservation equations on each axial segment and correlations for the various heat transfer regimes from the literature.

Fig. 1. A longitudinal channel segments along the *z* axis.

3. The experimental apparatus: The schematic diagram of the test apparatus is shown in Fig. 2. The test section is a stainlesssteel tube with the dimensions of L × Din = 1000 mm × 8.3 mm, which was directly heated by high-current from a power supply. The water flowed vertically upwards, in parallel inside the test section and through a larger bypass. The total flowrate and the flowrate through the test section were measured continuously The exit pressure was always near atmospheric by keeping the water tank open to the atmosphere. The supplied voltage and current were measured during the experiments to evaluate the channel power. Four K-type thermocouples were used to measure the outside channel temperature during the experiment at four levels along the channel, as described in Fig. 2.

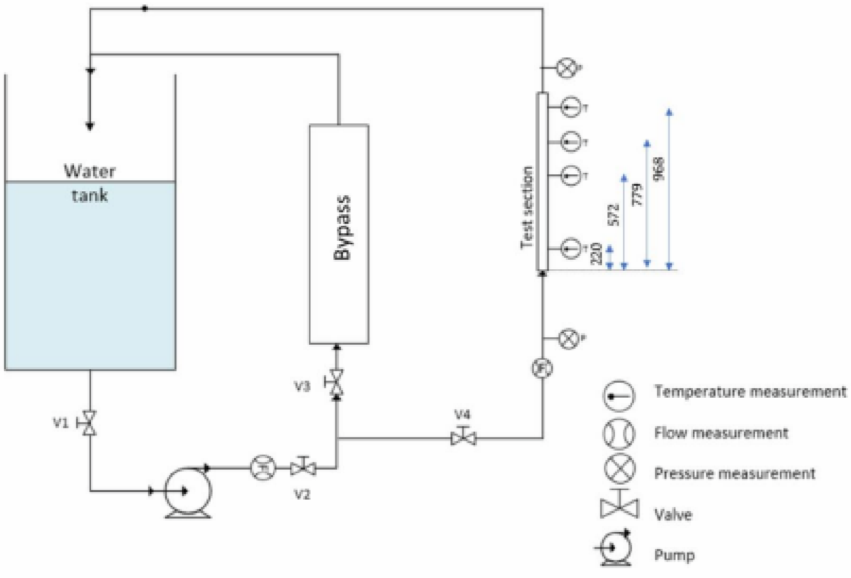

Fig. 2. Schematic diagram of experimental system.

During the experiment, the channel power was increased gradually while keeping the flow rate and the inlet temperature almost constant. At a certain power, a sudden decrease of the flow rate inside the heated channel occurs due to boiling and two-phase flow inside the heated channel, which increase the channel flow resistance and redistribution of the flow rate between the heated channel and the bypass. In those conditions, the wall temperature starts to increase continuously.

4. Model validation:

To compare the model to the experimental results in the single-phase region, the transient equations and correlations of Sieder & Tate [3] were used. Fig. 3 shows an example of a comparison between the outer calculated wall temperature and the experimentally measured values during the power variation (thick green line in the figure) at the single-phase zone of the experiment.

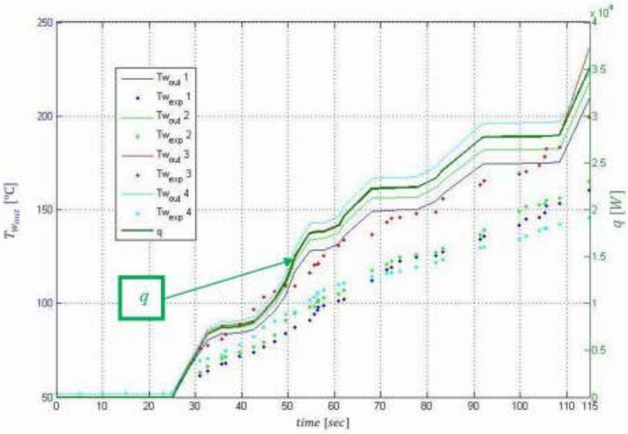

Fig. 3. The external wall temperature measured experimentally and calculated according to the correlation of Sieder & Tate at the different heights (T1-T4).

At the two-phase conditions relevant correlations were used in the model for the heat transfer coefficient, whereas in the case of post-Critical Heat Flux conditions, correlations for film boiling mechanism were used. Figure 4 shows a comparison between the calculation code results and the experimental values for the entire experiment duration. This code makes use of the correlations that were chosen in the previous stages as follows:

- Single-phase zone - Sieder & Tate.
- Two-phase zone before crossing the critical heat flux threshold - Lu & Chen.
- Two-phase zone after crossing the critical heat flux threshold and void fraction $\alpha>0.9$ - the correlation proposed in this work. The critical heat flux threshold was defined according to the Knoebel [7] correlation.

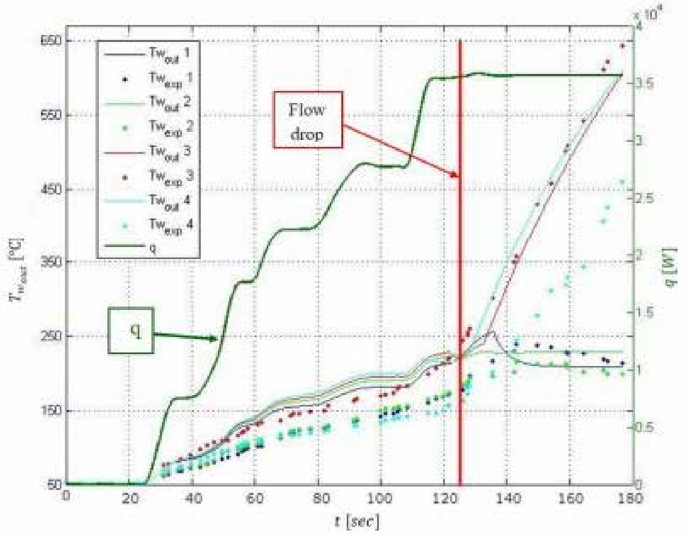

Fig. 4. An overall comparison between the model and the experimental results.

The model presents an over prediction at the single-phase flow regime (partially due to measurement accuracy) and a good match at the two-phase regime. A relatively smooth transition from single-phase to two-phase regime and a critical heat flux condition are obtained from the model which were obtained at the higher zone of the channel.

5. Conclusions: present work describes a transient computational code for prediction of the heat transfer regimes and the channel wall temperature during a transient heating of the channel. Several correlations were used to calculate the wall temperature at single-phase and two-phase conditions. Based on the present work the Sieder & Tate correlation was proposed to be used for the single-phase zone. For the two-phase zone, Lu & Chen correlation is proposed, whereas the Knoebel correlation was used for calculating the Critical Heat Flux threshold. In the case of exceeding the CHF, a correlation for film boiling was used. A new correlation was proposed for the post-CHF conditions, based on the calculated void fraction in the channel, to get a weighted heat transfer coefficient. The proposed model gives a prediction option to be used in case of boiling crisis in various applications focusing on a Safety Analysis Reports (SAR) of nuclear reactors.

Numerical study of flow, heat transfer and nucleate boiling over a wavy wall

Tal E., Ishay L., Ziskind G.

Background: One of the most effective methods to enhance heat transfer in forced convection is through modifications of the wall which is in contact with the fluid [1], [2]. A wavy wall, for example, can increase heat transfer capacity by tens of percent while maintaining a moderate increase in pressure drop compared to other geometries. Despite the overall enhancement in heat transfer, specific regions experience impaired performance due to boundary layer separation and the formation of reverse flow [3]. These regions emerge after the wave peak, where local temperatures are expected to rise above the average surface temperature [4]. This phenomenon is particularly important when the working fluid is a liquid that may start to boil at these hot spots along the wavy surface. In applications where boiling is undesirable, such as research nuclear reactors, where water serves as the coolant for fuel rods, it is imperative to characterize the flow regime and examine the effects of geometry, bulk flow in the channel, wall thermal conductivity and other parameters.

This research presents a numerical study of flow dynamics, heat transfer and the onset of nucleate boiling (ONB) on wavy walls. The study aims to evaluate the impact of surface waviness on heat transfer enhancement and identify regions prone to nucleate boiling initiation. The findings are of importance for nuclear reactors, where accurately predicting and managing ONB is crucial for ensuring reactor safety and operational efficiency.

Methods: The current study employed Computational Fluid Dynamics (CFD) to model turbulent flow and heat transfer over wavy surfaces. The Reynolds-Averaged Navier-Stokes (RANS) equations were used in conjunction with two turbulence models: the k-ε (standard & realizable) model and the k-ω SST model. These models were chosen for their ability to capture complex flow features characteristic of wavy geometries [5]. Additionally, for modeling the onset of nucleate boiling, the RPI model was utilized under the definition of two-phase flow using the Eulerian method, with bubble growth coefficients and inter-phase interaction forces explicitly defined.

A comprehensive validation of the numerical approach was carried out, examining channels with wall waviness of $\alpha = 2\alpha/\lambda = 0.2$ and 0.25 across a Reynolds number range from 5,000 to 36,000. The modeling results were compared with experimental and numerical data from the literature, including comparisons of flow velocities, heat transfer, and onset of boiling on both smooth and wavy walls.

Results: The simulations demonstrated that wavy surfaces can improve the overall heat transfer by up to a factor of two compared with smooth surfaces, particularly at wave crests where flow reattachment enhances heat transfer and increases the local Nusselt number. Conversely, wave troughs experienced localized flow separation and reverse flow, leading to higher temperatures and an increase the probability to onset of nucleate boiling.

Among the turbulence models examined, the k-ω SST model exhibited better accuracy in predicting the flow regime and heat transfer. Two-phase flow simulations indicated that wavy surfaces may reduce the mean wall temperature by several degrees compared to smooth surfaces. This reduction is significant in practical applications, as it improves thermal performance. However, thermal hotspots near wave troughs, due to recirculation zones, presents safety challenges.

The local Nusselt number distribution along the wavy surface exhibited distinct trends: high values were observed at wave crests due to colder bulk water that reaches the surface in the reattachment region, improving heat transfer. On the other hand, in wave trough regions, the presence of low-velocity and recirculating flow leads to reduction in the local Nusselt number, as shown in figure 1. These findings emphasize the importance of optimizing wave geometry along with thermal conductivity to address the heat flux distribution, particularly in nuclear reactor fuel rod cooling applications.

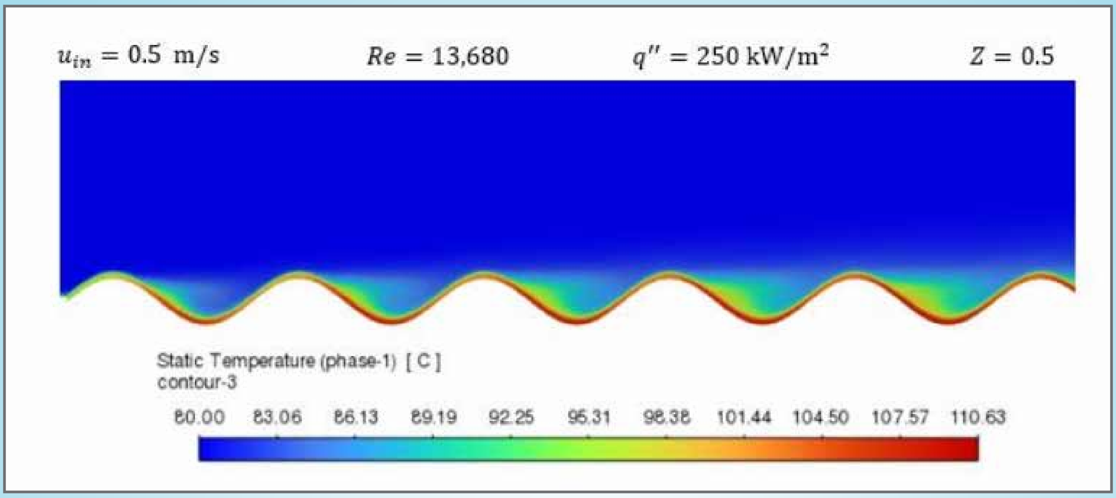

Figure 1: Temperature contour at the mid-channel plane

Additionally, three-dimensional numerical two-phase modeling was conducted for channels with both smooth and wavy walls at Reynolds numbers ranging from 6,000 to 32,000, using water at a subcooling of 20°C. Various heat fluxes were defined, ranging from relatively low heat flux values corresponding to a single-phase flow, to higher heat fluxes where nucleate boiling and two-phase flow were observed. The results of these simulations were compared with experimental data, showing good agreement, particularly for the k-ω SST model, across both single-phase and two-phase regimes.

From the two-phase modeling, it can be noted that for the examined cases, a wavy wall results in an average temperature difference between the wall and fluid that is approximately 3°C lower than that of a smooth wall. However, hot spots were identified in the wave troughs near the side walls of the duct, where the temperature equaled or even exceeded the average temperature of a smooth surface. This suggests that while the average heat transfer coefficient increases for a wavy wall, the onset of nucleate boiling (ONB) may still occur at similar heat fluxes as those observed in smooth channels. A comparison of boiling curves for both cases did not reveal a significant improvement for the wavy wall, indicating that ONB appears under comparable heat flux conditions.

Discussion and Conclusions: This study addressed heat transfer from wavy surfaces in thermal applications and revealed that although thermal enhancement is achieved, local hotspots are created. The k-ω SST turbulence model demonstrated good capability in capturing detailed flow and thermal characteristics, making it a reliable tool for modeling and design optimization in heat transfer applications. A comparison of boiling simulations between smooth and wavy walls did not indicate that modifying the surface geometry significantly improves heat transfer or delays the ONB. However, this study examined only a specific wavy surface with an amplitude-to-wavelength ratio of $\alpha = 2\alpha/\lambda = 0.25$. Additionally, recent advancements in two-phase boiling models offer improved capabilities. Therefore, future work should implement these models (as done in the present work) on a range of wavy surfaces and employ updated boiling models to enhance accuracy and applicability.

Characterization of Heat Transfer and Friction Coefficients in a Closed Loop Thermosyphon Flow

D. Saban, Y. Weiss, Y. Aharon, A. Koyfman, S. Gaillot, E. Lo Pinto, M. Katz

Zohar experimental device is a water closed loop system designed to simulate the thermosyphon cooling during the re-irradiation phase in LORELEI experiment, studied for Jules Horowitz Reactor project. Zohar is made of concentric annular channels, thermally connected. A central heating element represents the fuel pin while peripheral heaters simulate gamma heating in the pressure flask. For the first campaign, experiments were conducted with a central heating power range of 1÷4 kW. From several temperature measurements in Zohar, thermosyphon flow rates and convective heat transfer coefficients at the heater wall were derived. An analytical model of the loop was also developed, using correlations from the literature. In the model, friction factors were adjusted to match measured water temperature distribution and flow rate. Comparisons revealed the heat transfer correlation from Vliet (1969) [1] gave the best agreement between model and measurements. Still, a correction coefficient to the friction factor was needed.

1. Introduction: Natural convective flow can be found in many engineering applications such as solar systems for water heating, turbine blade cooling, geothermal energy production and electronic chip cooling. In nuclear reactors, natural convection is used as passive cooling mechanism which increases the safety and reliability of the reactor. LORELEI experimental setup in Jules Horowitz Reactor (JHR) is dedicated to the study of fuel during a Loss of Coolant Accident (LOCA). The main objective of LORELEI (Light-water One-Rod Equipment for LOCA Experimental Investigation) is to study the thermomechanical behaviour of fuel during such an accident and the fission products source term. Prior to the experimental phase, the fuel sample needs to be irradiated in order to generate measured level of fission products. The fuel is irradiated in a closed capsule and cooled by closed loop thermosyphon. This research aims to study the cooling mechanism in a closed loop capsule by thermosyphon flow, and especially the thermosyphon mass flow rate generated as a function of the power generated in the fuel pin, the heat transfer coefficient and the friction losses.

2. Experimental Loop: The experimental system is schematically shown in Figure 1. It includes a pressure vessel, a cooling exchanger that removes the heat generated in the vessel, and a Helium gas system that keeps single-phase conditions by increasing the pressure above the water. The vessel height is 1970 mm and it is made of two connected concentric annular channels: an inner “hot” channel and a peripheral “cold” channel. The channels outer diameters are 25 mm and 78 mm, respectively. In the centre of the hot channel, a 9.5 mm diameter central rod is located, holding a 600 mm long heating element that simulates the nuclear fuel pin with a maximum power of 4 kW. Cooling channels are positioned around the vessel and remove the power from the vessel in two sections, above and below the peripheral heating element level. The heat generated by the central heating element induces thermosyphon flow in the vessel, water flows upward in the hot channel around the central heating element and downward as it cools in the cold peripheral channel. The water flow rate of the thermosyphon flow is determined by the balance between the driving force (buoyancy forces) and the friction forces along the flow loop. 23 thermocouples measure water temperature along the loop, and central heater wall temperature.

3. Experimental Results: Typical experimental results are presented in Figure 2. The left side of the figure presents the water temperature along the loop channels for a heating power of the central rod 3972 W. The blue line depicts the axial water temperature distribution in the inner channel, while the red line depicts the temperature in the peripheral channel. The thermosyphon mass flow rate is calculated from equation

(1) thanks to temperature measurements of water by two thermocouples located along the heating element, assuming no heat transfer between the hot and cold channels.

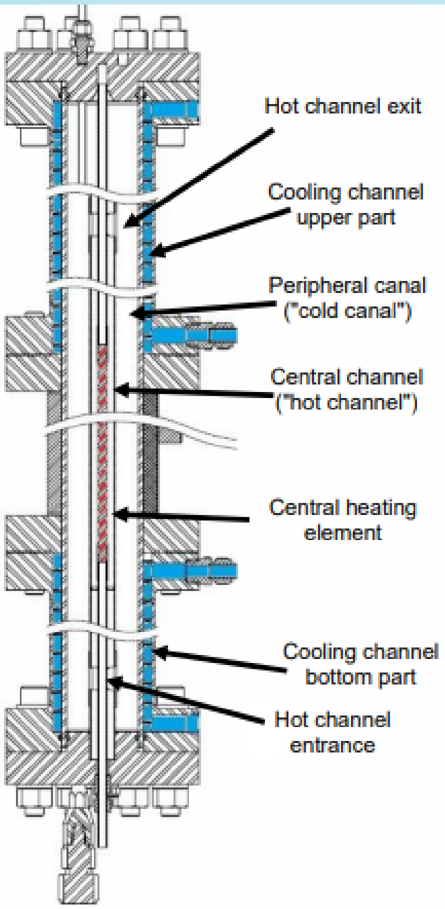

Figure 1: Schematic figure of the experimental column

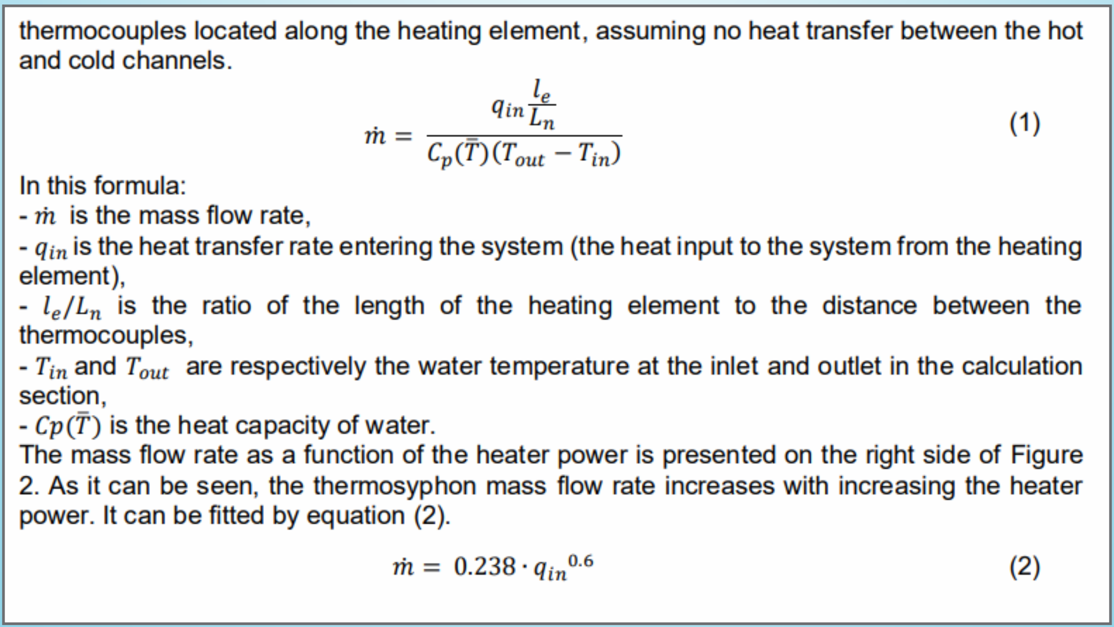

thermocouples located along the heating element, assuming no heat transfer between the hot and cold channels.

$$\dot{m} = \frac{q_{in}\frac{l_e}{L_n}}{C_p(\bar{T})(T_{out} - T_{in})} \qquad (1)$$

In this formula:

- $\dot{m}$ is the mass flow rate,
- q_{in} is the heat transfer rate entering the system (the heat input to the system from the heating element),
- l_e/L_n is the ratio of the length of the heating element to the distance between the thermocouples,
- T_{in} and T_{out} are respectively the water temperature at the inlet and outlet in the calculation section,
- $Cp(\bar{T})$ is the heat capacity of water.

The mass flow rate as a function of the heater power is presented on the right side of Figure 2. As it can be seen, the thermosyphon mass flow rate increases with increasing the heater power. It can be fitted by equation (2).

$$\dot{m} = 0.238 \cdot {q_{in}}^{0.6} \qquad (2)$$

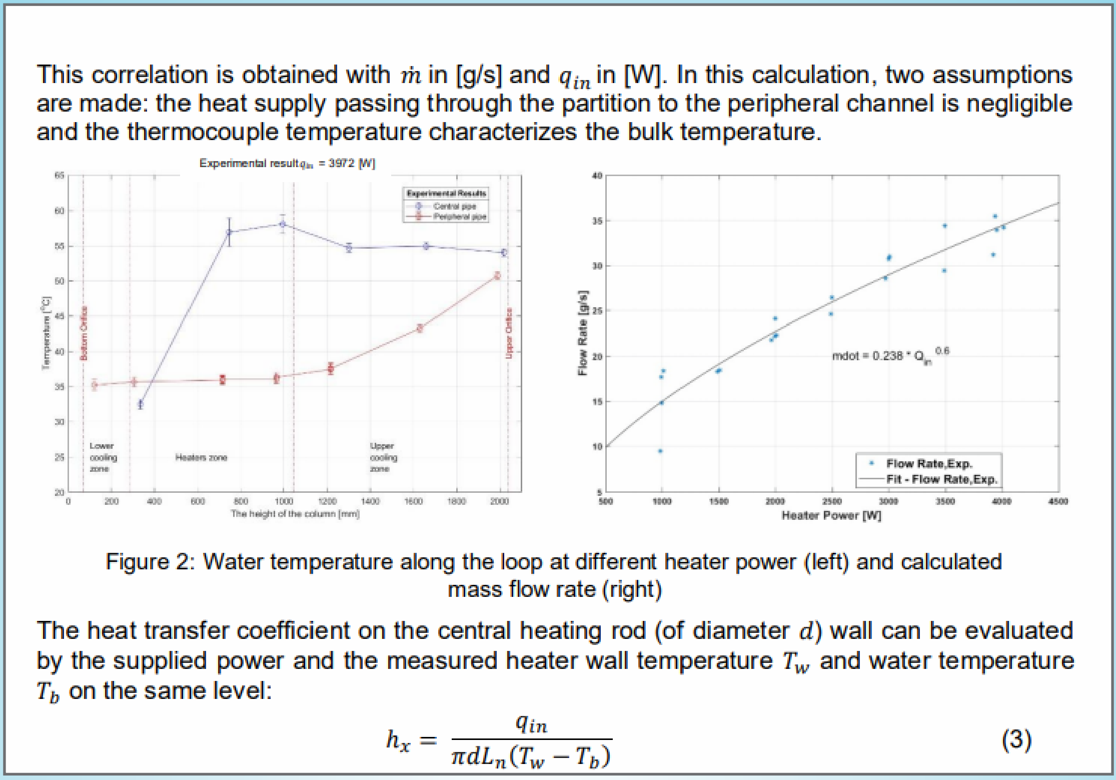

This correlation is obtained with $\dot{m}$ in [g/s] and q_{in} in [W]. In this calculation, two assumptions are made: the heat supply passing through the partition to the peripheral channel is negligible and the thermocouple temperature characterizes the bulk temperature.

Figure 2: Water temperature along the loop at different heater power (left) and calculated mass flow rate (right)

The heat transfer coefficient on the central heating rod (of diameter d) wall can be evaluated by the supplied power and the measured heater wall temperature T_w and water temperature T_b on the same level:

$$h_x = \frac{q_{in}}{\pi d L_n (T_w - T_b)} \qquad (3)$$

As studied in the literature review, the flow regime in thermosyphon flow in pipes is forced pipe flow. Using the calculated mass flow rate, the average velocity can be calculated for the inner channel cross section and Reynolds number can then be evaluated.. The Reynolds number obtained shows that the flow in the central channel is laminar in most of the power range, i.e. *Re* < 2500 up to a power of 3 kW, and above this power and up to 4 kW the flow is in the transition zone. Based on the wall temperature measured on the central heater wall, a Nusselt number *Nud* was calculated as a function of the Reynolds number, as presented on the left side of Figure 3. Another heat transfer mechanism that could be examined along the heater length is natural convection over a vertical cylinder. Nusselt number *Nux* was calculated where the distance x is the position of the thermocouple along the heating element. Rayleigh number Ra^* was calculated using wall and bulk flow thermocouples, assuming uniform heat flux on the heating element. On the right side of Figure 3, *Nux* is presented as a function of Ra^*, fitted with a known correlation(equation (4) from reference [1]) for heat transfer coefficient in natural.

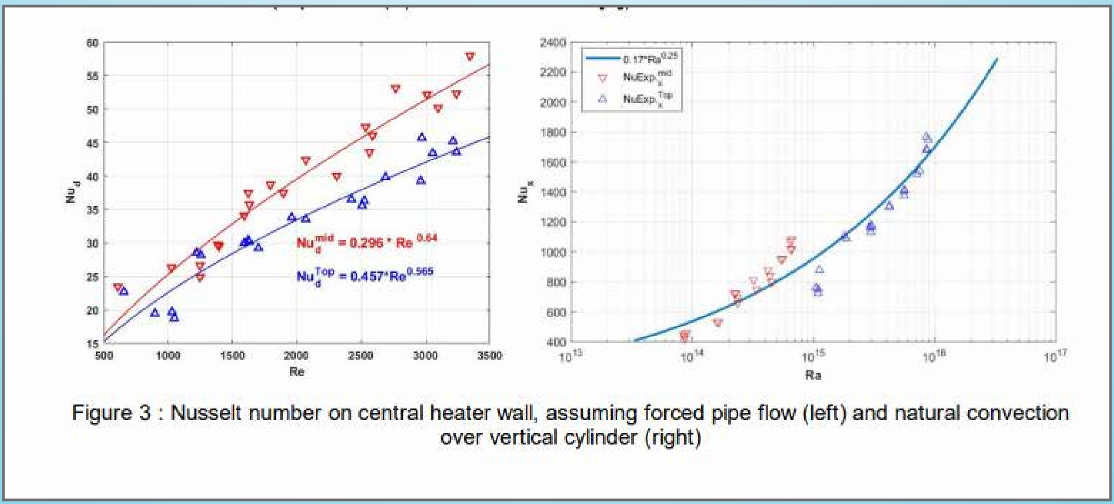

Figure 3 : Nusselt number on central heater wall, assuming forced pipe flow (left) and natural convection over vertical cylinder (right)

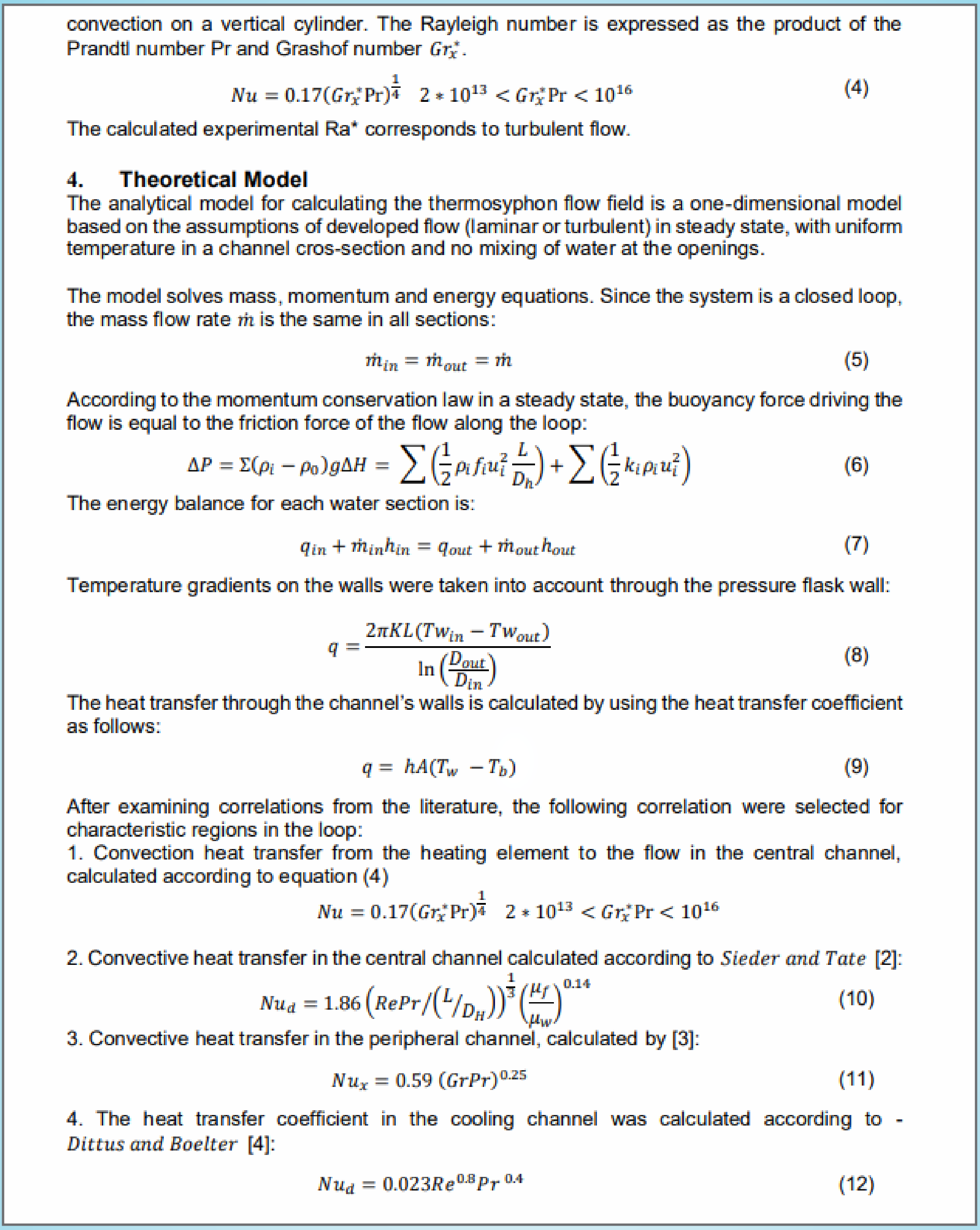

convection on a vertical cylinder. The Rayleigh number is expressed as the product of the Prandtl number Pr and Grashof number Gr_x^*.

$$Nu = 0.17(Gr_x^* \mathrm{Pr})^{\frac{1}{4}} \quad 2 * 10^{13} < Gr_x^* \mathrm{Pr} < 10^{16} \tag{4}$$

The calculated experimental Ra* corresponds to turbulent flow.

4. Theoretical Model

The analytical model for calculating the thermosyphon flow field is a one-dimensional model based on the assumptions of developed flow (laminar or turbulent) in steady state, with uniform temperature in a channel cros-section and no mixing of water at the openings.

The model solves mass, momentum and energy equations. Since the system is a closed loop, the mass flow rate $\dot{m}$ is the same in all sections:

$$\dot{m}_{in} = \dot{m}_{out} = \dot{m} \tag{5}$$

According to the momentum conservation law in a steady state, the buoyancy force driving the flow is equal to the friction force of the flow along the loop:

$$\Delta P = \Sigma(\rho_i - \rho_0) g \Delta H = \sum \left(\frac{1}{2} \rho_i f_i u_i^2 \frac{L}{D_h}\right) + \sum \left(\frac{1}{2} k_i \rho_i u_i^2\right) \tag{6}$$

The energy balance for each water section is:

$$q_{in} + \dot{m}_{in} h_{in} = q_{out} + \dot{m}_{out} h_{out} \tag{7}$$

Temperature gradients on the walls were taken into account through the pressure flask wall:

$$q = \frac{2\pi K L (Tw_{in} - Tw_{out})}{\ln\left(\frac{D_{out}}{D_{in}}\right)} \tag{8}$$

The heat transfer through the channel's walls is calculated by using the heat transfer coefficient as follows:

$$q = hA(T_w - T_b) \tag{9}$$

After examining correlations from the literature, the following correlation were selected for characteristic regions in the loop:

1. Convection heat transfer from the heating element to the flow in the central channel, calculated according to equation (4)

$$Nu = 0.17(Gr_x^* \mathrm{Pr})^{\frac{1}{4}} \quad 2 * 10^{13} < Gr_x^* \mathrm{Pr} < 10^{16}$$

2. Convective heat transfer in the central channel calculated according to *Sieder and Tate* [2]:

$$Nu_d = 1.86 \left(RePr/\left({}^{L}/_{D_H}\right)\right)^{\frac{1}{3}} \left(\frac{\mu_f}{\mu_w}\right)^{0.14} \tag{10}$$

3. Convective heat transfer in the peripheral channel, calculated by [3]:

$$Nu_x = 0.59\ (GrPr)^{0.25} \tag{11}$$

4. The heat transfer coefficient in the cooling channel was calculated according to - *Dittus and Boelter* [4]:

$$Nu_d = 0.023 Re^{0.8} Pr^{\ 0.4} \tag{12}$$

5. Discussion: The left graph in Figure 4 shows a comparison between the measured and calculated temperature variation in the flow, for a heater power of 2000W. As it can be seen, the computational model qualitatively predicts the water temperature in the tank. The calculated water temperature change in the tank (along the heating element) is smaller than the measured temperature difference, indicating that the calculated mass flow rate is higher than the actual one. This deviation is shown in the right plot in Figure 4, the calculated mass flow rate is compared to the measured flow rate. Since the thermosyphon flow rate is determined from a balance of buoyancy forces with friction forces, the deviation in friction forces can result from the correlation used for the friction factor and local friction losses at the upper and lower openings.

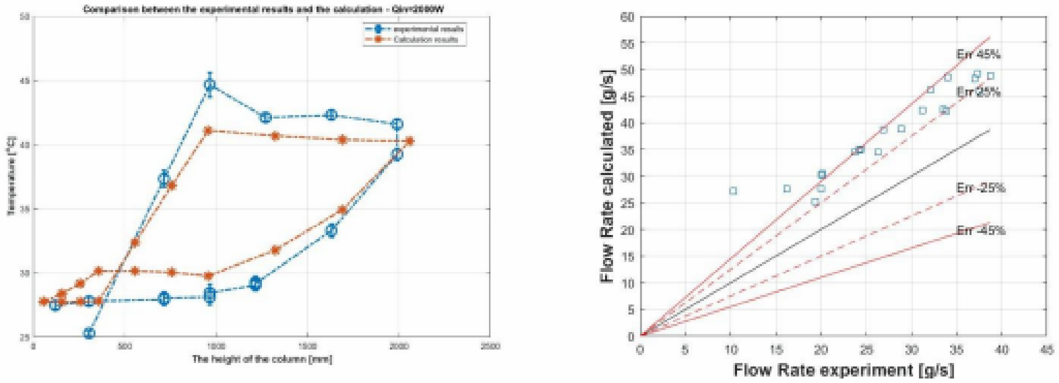

Figure 4: Comparison between measured and calculated water temperature, heater power 2kW (left). Calculated mass flow rate vs. measured flow rate (right)

In order to estimate the deviation in the friction force, a correction factor was applied on the right side of equation (6). Figure 5 presents on the left the calculated mass fow rate for a correction factor of 1 and 3 in black and red lines, respectively. It can be seen that a good fit is obtained with the experimental values. On the right side of Figure 5, the calculated mass flow rate is presented as a function of the measured flow rate. It seems that for a power higher than 1.5 kW, a correction factor of 3 predicts the experimental flow rate with an accuracy of 15%.

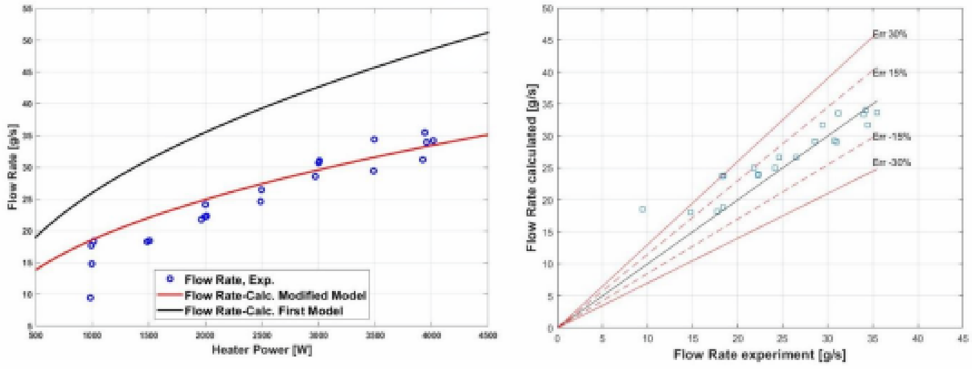

Figure 5: Comparison of mass flow rate as a function heating power between initial and corrected model (left). Calculated mass flow rate vs. measured flow rate for a correction factor of 3 (right)

6. Summary and Conclusions: This work examined the behavior of a closed-loop thermosyphon flow and characterized the heat transfer and friction coefficients in a vessel simulating LORELEI experimental setup in Jules Horowitz Reactor (JHR). A series of experiments were performed for several input powers of the central heating element, inducing thermosyphon flows. Temperature measurements included water temperature and heater wall temperature. A one-dimensional analytical model was developed to calculate the mass flow rate and water temperature. The analytical model predicts closely the temperature gradients along the loop. The flow rate is overestimated by 25-40%, indicating that the friction losses in the system are higher than predicted. A correction factor of 3 on the friction forces reduce the deviation to 15%. For a heating power of 1000÷4000 W, the water flow rate in the system is 15-35 g/s and the water velocity in the central channel around the heating element is 4.5-8 cm/s. In this power range, the flow is laminar for a heating power lower than 2500 W and transitional up to 4000 W. In order to calculate the heating element wall temperature, the correlation for heat transfer coefficient in natural convection, 0.17 $Ra^{*}0.25$, can be used.

Experiments and modeling of cooling circles and cooling tower for nuclear reactors

Z. Sahray, I. Zucker, S. D. Amar, Y. Shaposhnik and Y. Soffer

The inlet temperature of a nuclear reactor is of importance for normal operation and safety purposes. This temperature is affected by different parameters, and is maintained to a desired value by controlling these parameters. Cooling circles and towers are used in the operation of the reactor in order to determine the inlet temperature to the reactor. Controlling the parameters of the cooling circles is usually limited, as it depends on the hydraulic components of the circles (pumps, heat exchangers and flows). One of the most common parameters which affects the effectiveness of the tower is the angular velocity of the fans in the cooling towers. A thermodynamic equilibrium model for multiple thermohydraulic circles was developed, accounting for the variety measured parameters in each circle and specifically for the calculated tower constant. The model was validated by changing the reactor state, and performing experiments in different environment conditions. Figure 1 presents the model results of the ratio between the temperature difference to the maximum possible temperature difference in color-bar as a function of pairs of wet-bulb temperature (*y*-axis) and scaled fans frequencies (*x*-axis).

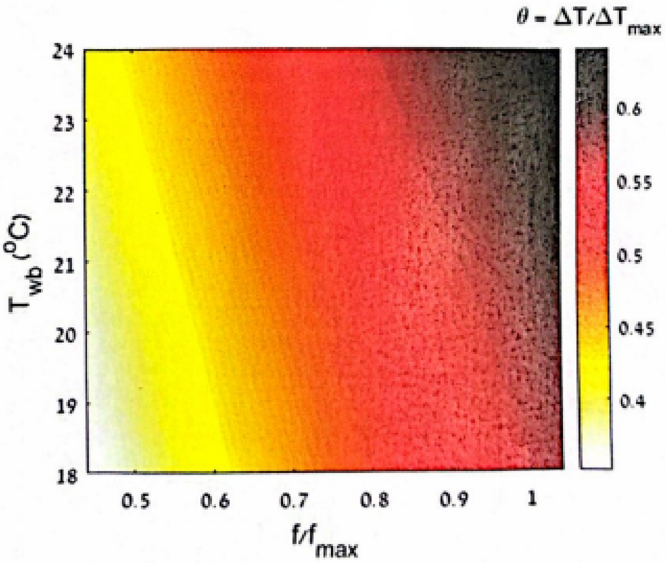

Figure 1 – Model results of the scaled temperature difference as a function of the wet-bulb temperature and scaled fans frequencies.

Metal Ignition in Nuclear Fuel Channels

E. Elias[1], D. Hasan[1], Y. Nekhamkin[1], J. Dayan[1], H. Haustein[2]

1 Faculty of Mechanical Engineering, Technion, Israel
2 Department of Mechanical Engineering, Tel Aviv University

Theoretical analysis of thermochemical steam-metal reactions at the exposed section of a fuel channel during a hypothetical Loss of Flow accident has been conducted. A dimensionless criterion is derived to define the limiting thermohydraulic conditions that could lead to metal ignition and potential destruction of the upper section of a fuel channel. This criterion is tested theoretically over a wide range of parameters using a detailed heat and mass transfer model. Results indicate that cladding ignition can be predicted from known initial and operational conditions, without the need to solve the full channel transient equations. A significant finding is the direct prediction of the minimum necessary coolant mass flow rate to prevent cladding ignition for given decay power and reactor pressure. The proposed ignition criterion can simplify reactor safety protocols and has the potential to enhance current safety requirements, which currently have focused primarily on maximum allowable cladding temperature.

1. Introduction: The concept of metal ignition was initially introduced by Khaikin et al. [1] and later expanded by the authors [2], who applied the classical Semenov [3] combustion analysis to derive a set of conjugate heat and mass balance equations at a heated metal surface. These equations described the time evolution of temperature and oxide layer thickness on a small metal particle in a constant-temperature oxidizing gas environment.

In this work, we extend the classical combustion approach to address the unique conditions present in a partially exposed nuclear fuel channel during a Loss of Flow Accident (LOFA). We employ an innovative scheme to derive a reduced set of non-dimensional heat and mass balance equations, enabling the formulation of a dimensionless ignition criterion. This criterion accounts for decay heat release, steam flow rate, and the varying thermal conditions along the oxidizing cladding. The resulting ignition criterion incorporates both geometrical and thermal conditions, which can potentially lead to uncontrolled oxidation during a severe accident. The subsequent sections detail the proposed model and compare its results with comprehensive ASYST [4] predictions across a broad spectrum of conditions pertinent to Loss of Flow Accidents (LOFA) in Pressurized Water Reactors (PWR). It is demonstrated that the new criterion enables the a priori prediction of runaway cladding failure based solely on initial and operational conditions.

2. Metal ignition criterion in a flow channel: To understand the interrelated physical and chemical processes occurring at the steammetal interface during LOFA, we examine a heated pipe, of length Dz, representing the upper section of an oxidizing fuel channel. This pipe is heated by nuclear decay heat and cooled by steam entering at a specified mass flow rate and saturation temperature corresponding to the local reactor pressure. The system behavior can be described by the following set of mass and energy balance equations for three regions: steam, metal cladding, and oxide layer.

$$\begin{aligned} & M_S \frac{dh_S}{dt} = 2\pi R\Delta z \cdot H\left(T_C - T_S\right) - \dot{m}_{in}\left(h_S - h_{ig}\right) && \textit{Steam} \\ & \frac{dT_C}{dt} = \frac{q'\Delta z}{M_C C_C} + \frac{Q_0}{a_C C_C}\frac{d\delta}{dt} - \frac{H}{a_C \rho_C C_C}\left(T_C - T_S\right) && \textit{Cladding} \qquad (1) \\ & \frac{d\delta}{dt} = \frac{k_r}{\delta}\exp\left(-\frac{B}{T_C}\right) && \textit{Oxide Layer} \end{aligned}$$

where M expresses mass, h is enthalpy, R is pipe's radius, a cladding's thickness, C is specific heat, q' is linear decay heat power, Q_0 is heat of reaction, B is activation energy, k_r is pre-exponent reaction rate, H is convective heat transfer coefficient, δ is the thickness of oxide layer and the subscripts S, C and g refer to steam, cladding and saturated steam, respectively. The steam equation in Equation set (1) neglects momentum transfer considering only heat and mass transfer. Parabolic oxidation law is used to describe the thickness of oxide layer.

Integration of Equation set (1) for an arbitrary set of inlet and operational conditions relevant to a severe LOFA transient yields steam and metal temperature evolutions, as illustrated in Fig. 1, The plot reveals a critical minimum value of inlet steam flow rate (approximately 0.3162 g/s) below which the metal temperature escalates dramatically, leading to a runaway or ignition situation. Under these conditions, it is reasonable to assume that the cladding would eventually fail, as qualitatively observed during the Fukushima reactor accident [5].

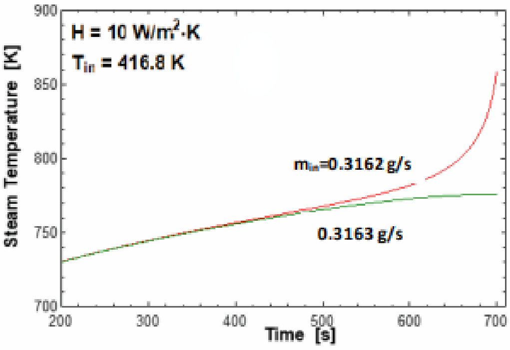

Figure 1: Steam temperature vs. time for near-critical inlet mass flow rates.

Metal ignition generally depends on several parameters that may include including pressure (inlet steam temperature), steam inlet flow rate, nuclear decay power, length of the exposed channel, and convective heat transfer coefficient, among others. This paper aims to derive a comprehensive ignition criterion that accounts for all relevant parameters. To achieve this, the number of independent variables' set (1) must first be reduced and expressed in a non-dimensional form. We begin by restating the steam equation in Equation set (1) in terms of steam temperature, rather than steam enthalpy.

$$
\begin{gathered}
t_{res,S}\frac{dT_S}{dt} = \xi T_C - \left(\xi + 1\right)T_S + T_{in} \\
where: \\
\xi = \frac{2\pi R\Delta z H}{\dot{m}_{in} C_S} \quad ; \quad t_{res,S} = \frac{M_S}{\dot{m}_{in}}
\end{gathered}
\tag{2}
$$

Here ξ is a non-dimensional heat transfer coefficient and $t_{res,S}$ is steam residence time. The steam specific heat, C_S, and mass, M_S in Equation (2) are assumed constant. Additionally, as observed in Fig. 1, and other similar results [5], the steam and cladding temperatures passs through an inflection point prior to ignition i.e.,

$$
t_{res,S}\frac{d^2T_S}{dt^2} = \xi\frac{dT_C}{dt} - \left(\xi + 1\right)\frac{dT_S}{dt} = 0
\tag{3}
$$

Equation (3) yields a relationship between the cladding and steam temperature evolution prior to ignition, providing critical insights into the thermal behavior the system, as,

$$
\frac{dT_S}{dt} = \gamma\frac{dT_C}{dt} \quad , \qquad \gamma \equiv \frac{\xi}{\xi + 1}
\tag{4}
$$

Since the evolution of steam temperature is linked to the rate of metal heating, Equation (4) can be used to eliminate the steam equation from the original set (1). This reduction simplifies the system from three equations to the classical set of two dimensionless heat balance equations for the metal and oxide layer.

$$
\begin{gathered}
\frac{d\theta}{d\tau} = \frac{d\eta}{d\tau} - \frac{\theta}{\omega} \\
\frac{d\eta}{d\tau} = \frac{1}{\eta}\exp\left(\frac{\theta}{1 + \beta\theta}\right)
\end{gathered}
\tag{5}
$$

Appropriate initial conditions for Equation set (5) are,

$$
at\ \tau = 0 \qquad \theta\left(0\right) = 0\ ,\ \eta\left(0\right) = \eta_i
\tag{6}
$$

In the following η_i was based on $\delta_i = 10^{-8}\ m$ as suggested by Khaikin [1].

The dimensionless parameters in Equation set (5) are defined below in set (7) The first equation in Equation set (5) represents a lumped parameter heat balance over a thin-walled metal pipe. The right-hand side balances the exponential thermochemical heat generation in the cladding with the rate of steam convective cooling. The parameter ω specifies the ratio between the rate of heat accumulation in the metal (over a characteristic time, t_*) and the heat transferred to the surrounding steam. The second relation in Equation set (5) describes the temporal evolution of the normalized oxidized layer thickness, η.

$$\eta=\frac{\delta}{\delta_*};\quad T_*\equiv T_{in}+\frac{q'}{2\pi R}\frac{2\pi R\Delta zH+\dot{m}_{in}C_S}{\dot{m}_{in}C_SH};\quad \theta=\frac{B}{T_*}\left(\frac{T_C}{T_*}-1\right)=\frac{1}{\beta}\left(\frac{T_C}{T_*}-1\right);\quad \tau=\frac{t}{t_*};$$
$$\delta_*=\frac{C_C\,a_C\,\beta T_*\left(1+\phi\right)}{Q_0};\ \beta=\frac{T_*}{B};\quad t_*=\frac{\delta_*^2\,e^{1/\beta}}{k_r};\quad \phi=\frac{H}{a_C\rho_C C_C}\frac{M_S}{\dot{m}_{in}}\gamma\kappa;\ \kappa\equiv\frac{1}{\xi+1}; \tag{7}$$
$$\omega=\frac{1}{H}\frac{a_C\,C_C\,\rho_C}{t_*}\frac{1+\phi}{\kappa}$$

In Equation set (5) there are two variables, θ an η and two parameters, β and ω. The first parameter, β, is a dimensionless characteristic temperature defined by the initial and operational conditions, while the parameter ω is the sought ignition parameter. For a given value of β, there exist a critical parameter $\omega=\omega_{cr}$, whose value essentially determines whether the system undergoes metal ignition ($\omega>\omega_{cr}$) or an extinction process($\omega\le\omega_{cr}$). Physically, it indicates whether the heat input rate at the metal surface exceeds or falls below the rate of convective cooling. Consequently, depending on the value of ω, the metal temperature could either stabilize or escalate uncontrollably.

Previous studies [1, 2] have delineated the critical value of ω_{cr} as a function of β. Subsequent investigations by the authors [5] revealed that, under conditions pertinent to LOFA, the critical value approximates $\omega_{cr}=1.6$. Utilizing this critical value, the parameters defined in Equation (7) can be employed to compute the minimum steam flow rate required to induce metal ignition for a given set of inlet and operational conditions. This computation is achieved without the need to solve the differential balance equations presented in Equation set (5).

Thus, by properly manipulating the heat balance equations, we have defined an ignition criterion that can be used to identify safety issues during LOFA, based on the a priori known initial and operational conditions. In the following section, we outline the procedure used to estimate the minimum steam mass flow rate at the exposed section of a fuel channel and verify the results in comparison with predictions from the safety code ASYST.

3. Results and discussions

To verify and examine the utility of the developed ignition criterion, we analyzed the transient response of an idealized fuel channel, schematically illustrated in Fig. 2, using the ASYST reactor safety code [4]. A thin-walled pipe was modeled to simulate a single fuel channel within a square lattice array of rods, defined by a specific pitch and rod outer radius. As water flows upward through the channel, it heats up and boils. Depending on the residual nuclear decay power, inlet temperature, pressure, and mass flow rate, the upper section of the channel may become exposed and either heat up gradually or experience a dramatic temperature escalation (ignition) due to intense runaway thermochemical reactions.

A series of ASYST simulations were conducted over a wide range of inlet and operational conditions to

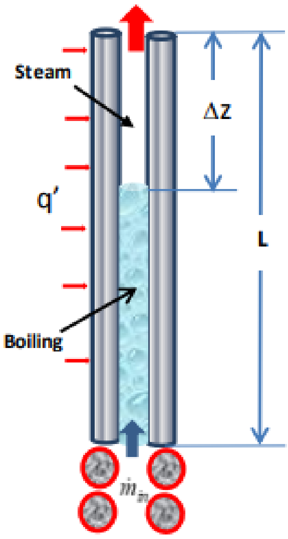

Fig. 2: Schematic representation of the fuel-channel

determine the critical inlet mass flow rate that leads to ignition in the upper section. The results, summarized in Fig. 3, depict the ASYST-calculated critical mass flow rates as a function of the total decay heating at the channel's surface, presented as scattered data points. The data in Fig. 3 correspond to a pressure of 4 bar and a channel length of 3.6 m.

Critical inlet flow rates were subsequently predicted independently for the same inlet conditions using the new ignition criterion. This was achieved by solving directly the relations in Equation set (7) with 1.6 w w= = cr . The predicted results, depicted as a continuous line in Fig. 3, demonstrate excellent agreement with the ASYST results (depicted as dots), which are based on the repeated solution of a set of differential balance equations within the channel.

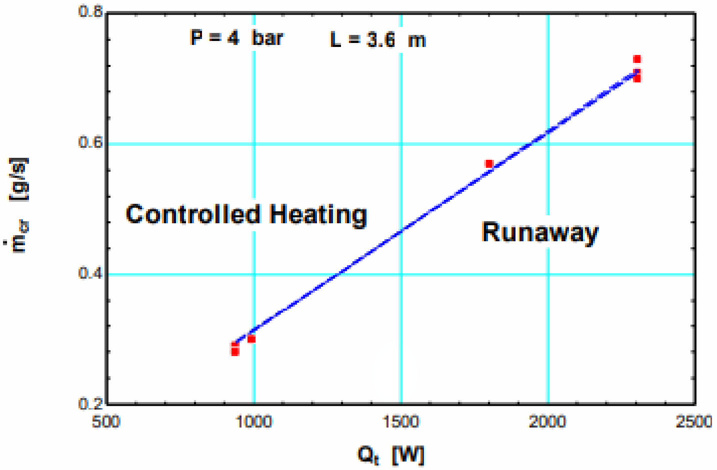

Fig. 3: ASYST calculated (dots) vs. ignition-criterion predicted (line) critical inlet flow rates for P = 4 bar and L=3.6 m

The applicability of the ignition criterion was further investigated by extending data comparison and verification to a broad spectrum of inlet conditions relevant to Loss of Flow Accident (LOFA) scenarios. Critical inlet flows were predicted for pressures up to 20 bars and for channel lengths as short as 2.4 meters. In applying the ignition criterion, the convective heat transfer coefficient was calculated using the Dittus-Boelter correlation [6]. Transport and thermodynamic properties were evaluated under superheated steam conditions. ASYST calculations were compared to predictions from the ignition criterion, as illustrated in Fig. 4. The two methods demonstrated good agreement once again.

4. Conclusions: Thermal runaway criteria are crucial for determining the onset of runaway phenomena, constructing safety diagrams, and designing appropriate accident mitigation procedures. This paper extends the classical concept of the ignition criterion to provide an a priori prediction of the minimum inlet flow rate below which ignition conditions occur at the upper section of a heated flow channel. The new dimensionless criterion, outlined in Equation set (7), is based on the known channel configuration, inlet conditions, and pressure.

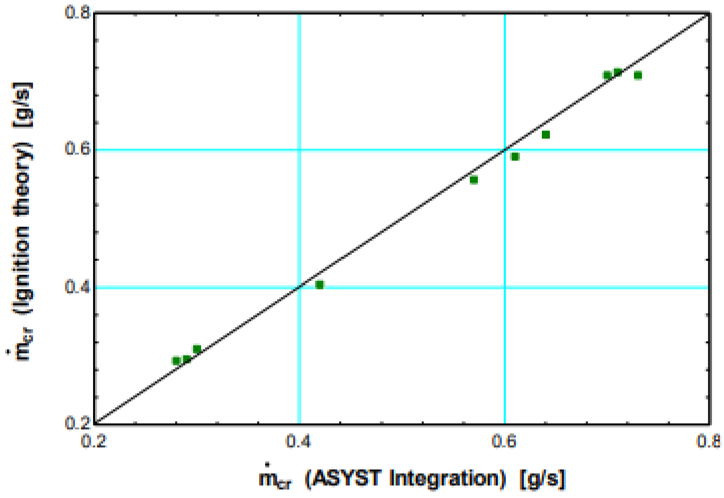

Fig. 4: ASYST calculated vs. ignition-criterion predictions of critical inlet flow rates for various pressures and channel lengths

A closed-form definition of an ignition criterion was achieved through a novel mathematical procedure that simplifies the classical three-equation model of heat and mass balance in the fuel channel to a set of two dimensionless equations. This model was applied to study the thermal behavior of an exposed section of a PWR-like fuel channel subjected to decay heat and metal-steam reactions at its surface. The results demonstrate the utility of the derived dimensionless ignition criterion for predicting runaway situations across a wide range of operational parameters. These findings enable the a priori prediction of runaway oxidation in the channel based on known inlet and operational conditions. It is suggested that the present model can be readily applied to predict runaway conditions in other abnormal events, such as air or steam oxidation of nuclear fuel cladding during dryout loss of flow in spent fuel storage pools. Forecasting runaway conditions in metals interacting with superheated steam may prove vital for the design, control, and safety assessment of high-power systems.

Acknowledgments: The work was supported by the Pazy Foundation. We appreciate the ISS/Academia cooperation that enabled to have the ASYST-THA code at our disposal.

Three-dimensional Vortex and Gas Entrainment Numerical Analysis in Rotating Liquid Flow with a Free Surface

S.D. Amar, D. Portnikov, A. Rashkovan, G. Ziskind

In nature and engineering, fluid movements involving swirling patterns, or vortices, are common occurrences. Some flows involve free-surface vortices that can potentially lead to a phenomenon termed gas-entrainment (GE). Intense rotation of free-surface flows, which unintentionally results from the underlying physical effects, can create gas cores that penetrate the liquid, leading to the formation of gas bubbles. These bubbles can then be drawn into the rotating equipment, causing cavitation or other damage. In nuclear reactors, especially Sodium Fast Reactors (SFR), entrained gas bubbles pose risks to safe plant operation due to fluctuations in reactivity. Similarly, in Light Water Reactors (LWR), during loss-of-coolant accidents (LOCA), gas entrainment into emergency core cooling system (ECCS) pumps can result in significant damage or malfunction.

There is no validated tool that can predict the free-surface profile of the gas core prior and subsequent to the GE. This study focuses on experimental and numerical investigation of flows with unsteady free-surface vortices that can potentially lead to gas entrainment.

An experimental work, performed in a dedicated experimental setup built in the present study, is used to measure the free-surface profiles by high-speed camera. The free-surface profiles are used to validate the numerical approach. The three-dimensional numerical tool incorporates Large Eddy Simulation (LES) to capture turbulence, with Volume-of-Fluid (VOF) approach to simulate free-surface profiles.

The model predicts with high accuracy the free-surface profiles in cases with and without GE, observed experimentally. Then, the detailed simulation results for this type of flows are analyzed quantitatively, using radial, axial and tangential velocity components.

This work is based on a recently published article (Amar et al. 2024). The experimental and numerical achievements in this study can serve as a tool both to predict the free-surface flow profiles with high accuracy and to prevent gas entrainment in the engineering systems.

Session 4 – Radiation Protection and Environmental Risk Assessment

Moderator: Lior Epstein

Radiation Protection Aspects and Optimization of Spent Nuclear Fuel Transportation for Research Reactors

Gross R., **Epstein L., Heflinger D., Taub M., Gabrieli G., Krakovich A., Brandis M.**

Keywords: spent nuclear fuel, radiation protection, FLUKA. Transportation of Spent

Nuclear Fuel (SNF) is a complex task where safety and radiation protection (RP) are of high concern. SNF contains various radioactive isotopes, originating from fission of fissile materials (typically, 235U) in the fuel. At the end of the reactor lifetime, the nuclear fuel is stored in a cooling pool to allow for the decay of short-lived fission products and decrease the radioactivity and consequently, the decay heat emanating from the fuel assemblies. Afterwards, the SNF is transported to a storage facility.

The process of transporting SNF involves placing the fuel assemblies in transfer casks and loading them into transport containers. In this work, we calculate the expected doses to the workers involved and suggest optimization of the loading scheme to reduce the dose rates in the process for a typical open-pool research reactor.

The dose rates were calculated using the FLUKA Monte Carlo code according to the geometries, materials composition and radionuclides inventory of the SNF.

Patient and Medical Team Doses from Embedded Radioactive Fragment in Radiological Dispersal Device Scenarios

Shukrun R. H., Datz, H., Zalevsky Z., and Epstein L.

Background: Radiological terrorism refers to the deliberate use of radioactive materials to harm a targeted population. Although no such events have been reported to date, the potential for radiological terrorism remains a significant concern. Following the detonation of a Radiological Dispersal Device (RDD), a unique exposure pathway emerges - embedded fragments containing radioactive materials. Addressing this type of trauma injuries calls for a detailed understanding of both the radiological and the conventional hazards. This study provides dose assessments from embedded fragments containing radioactive materials, representing a wide energy range: 60Co, 90Sr, 137Cs, and 192Ir.

Methods: We present a computational method for dose calculations using the computational adult male and female reference phantoms published by the International Committee for Radiation Protection (ICRP). We considered three exposure scenarios, each representing a radioactive fragment located in a different area of the body: head, torso, and leg. For each scenario, the doses were calculated for four radioactive sources: 60Co, 90Sr, 137Cs, and 192Ir. Four dose quantities are considered for each scenario: the local and organ absorbed doses, and the effective doses to the patient and to the medical staff treating the patient.

Results: The local and organ absorbed doses vary considerably between the different scenarios, ranging between several orders of magnitude. Local doses range between 1-1000 Gy/h per 1 GBq, organ doses range between 0.01-100 mGy/h per 1 GBq. The fragment containing 90Sr deliver the highest local dose due to the emitted beta particles, but also present a rapid decrease in dose beyond 1 cm from the source. High doses were reported in organs closer to the gamma emitting fragments. Bone marrow, one of the most radiosensitive organs, is expected to receive an absorbed dose of up to 20 mSv/h per GBq from a fragment containing 60Co and embedded in the torso.

The effective dose rates for the patient range from 0.3 to 22 mSv/h per 1 GBq, with 60Co providing the highest doses. A fragment located at the torso leads to an effective dose higher than that of a fragment located in the foot or head, regardless of the considered isotope. Medical personnel near a patient with radioactive fragments are expected to receive non-negligible doses, which decrease with the distance from the patient. For example, standing 30 cm away from a patient with an embedded fragment containing 10 GBq of 60Co could lead to exposure exceeding the threshold dose set by the IAEA for emergency responses, 500 mSv, within five hours. The same fragment could lead to exposure exceeding 20 mSv whithin 12 minutes.

Discussion and conclusions: The presented study aim to provide dose assessments due to an embedded fragment following an RDD event. While each patient and scenario are different, our results can help understand the complex factors contributing to the dose calculations, assisting in real time prioritization of fragment removal. The dose assessments are essential in minimizing radiation exposure to patient and staff and can improve preparedness for such an event.

Tungsten base materials selection for shielding and balancing In medical and nuclear field

Dov Chaiat

Tungsten-based materials are increasingly becoming the go-to choice over lead for shielding and balancing in the medical and nuclear industries. While lead is cost-effective, it falls short in shielding effectiveness, mechanical strength, heat resistance, longevity, and design flexibility. Plus, lead's hazardous nature demands stringent health and safety precautions due to its toxicity.

In contrast, tungsten materials are environmentally friendly and significantly reduce health risks associated with lead exposure. They allow for thinner shields without sacrificing protection, thanks to their high density (Fig.7). Tungsten is hard, durable, and resistant to surface damage. It's also easy to sterilize and maintain, ensuring a clean and safe working environment—crucial in medical settings.

Categories of Tungsten Materials:

1. Tungsten Powder
   - Fine tungsten particles with high packing density.
   - Used in steel-encased radiation shields or heavy concrete for structural shielding.
2. Pure Tungsten
   - Density of 19.25 g/cm^3: available in foils, sheets, discs, and rods.
   - Ideal for compact, high-performance shielding components.
3. Tungsten Alloys
   - Alloys like W-Ni-Fe, W-Ni-Cu, and W-Cu (density: 16.5-18.6 g/cm^3).
   - Customizable via machining, sintering, or Tungsten Injection Molding (TIM) for specific magnetic and nonmagnetic requirements.
4. Poly-Tungsten
   - Composite materials with densities of 10-13 g/cm^3, matching or surpassing lead.
   - Manufactured via injection molding or 3D printing for intricate and flexible designs.

Applications in the Medical Industry: Collimators, detection shielding, X-ray tubes, shielding curtains, syringe shields, radiotherapy equipment, and medical isotope production (Fig. 1-6).Tungsten is widely used in X-ray tube anodes for efficient heat dissipation and X-ray generation. It serves as a radiation shielding material in radiotherapy rooms and medical imaging facilities. Tungsten alloys are essential for gamma radiation shielding, surgical instruments, and imaging devices such as CT and PET scanners, owing to their strength, durability, and radiation-absorbing properties. Additionally, lead-free poly-tungsten composites provide an eco-friendly alternative to toxic lead in radiation shielding products, including X-ray panels, radiation therapy devices, and protective aprons.

Applications in the Nuclear Industry: Gamma-ray shielding, waste management systems, radioactive waste containers, collimators, and nuclear reactor piping systems (Fig. 1, 3-6).Pure tungsten blocks or sheets are used to shield equipment and personnel from radiation in nuclear reactors and waste storage facilities. Tungsten is also employed in reactor liners and components that require high melting points and resistance to radiation damage. Tungsten alloys play a critical role in control rods for managing fission, as well as in radiation shielding for neutron and gamma protection. They are also used in fusion reactor components, where they withstand extreme temperatures and high radiation flux. PolyTungsten composites provide advanced radiation shielding for nuclear reactors and efficient containment Systems for high-level radioactive waste, ensuring safety for personnel and sensitive equipment. Rubbertungsten composites can be used to create flexible barriers.

Advancements in Additive Manufacturing: Technologies like 3D printing enable the creation of complex tungsten base components, broadening design possibilities and enhancing performance (Fig. 3).

Tungsten for Plasma-Facing Components in Fusion Reactors: Tungsten's unique combination of properties makes it indispensable for advancing fusion energy technology, providing the robustness required for sustainable and efficient plasma containment.

In conclusion, tungsten-based materials provide unparalleled performance, safety, and environmental benefits compared to lead, supporting innovative advancements in the medical and nuclear sectors.

Seismic Analysis of Non Structural Components Based on Observation Data

Stav Kontarovich

Critical facilities in general, and especially nuclear facilities, require to maintain functionality and operability of critical systems during and / or after strong earthquakes. National standards provide requirements and guidance on design and analysis of buildings and structures (such as bridges, storage tanks, towers, ...). There's no equivalent national standard that provide mandatory requirements and guidance on design and analysis of non-structural components such as generators, pumps, instruments, valves and etc. Therefore, while common industry practices can provide some assurances on the durability of buildings to withstand strong earthquakes, there's very high uncertainty about the durability of non-structural equipment in strong earthquake motions. Analysis of safety critical equipment to withstand seismic loads is a common practice in the nuclear industry, especially in the design and analysis of nuclear power plants. The most common standard that address the issue is ASME QME. The standard allows to perform seismic qualification based on the following methods: Computational analysis, laboratory testing and observation data analysis. Electric Power Research Institute (known as EPRI) in collaboration with the Nuclear Regulatory Commission devised a comprehensive methodology to perform seismic qualification analysis based on observation data. The Study conducted by the author used the EPRI methodology to assess the seismic fragility of nonstructural equipment and provide analysis on the operability and functionality of safety related infrastructures.

The analysis included the following steps:

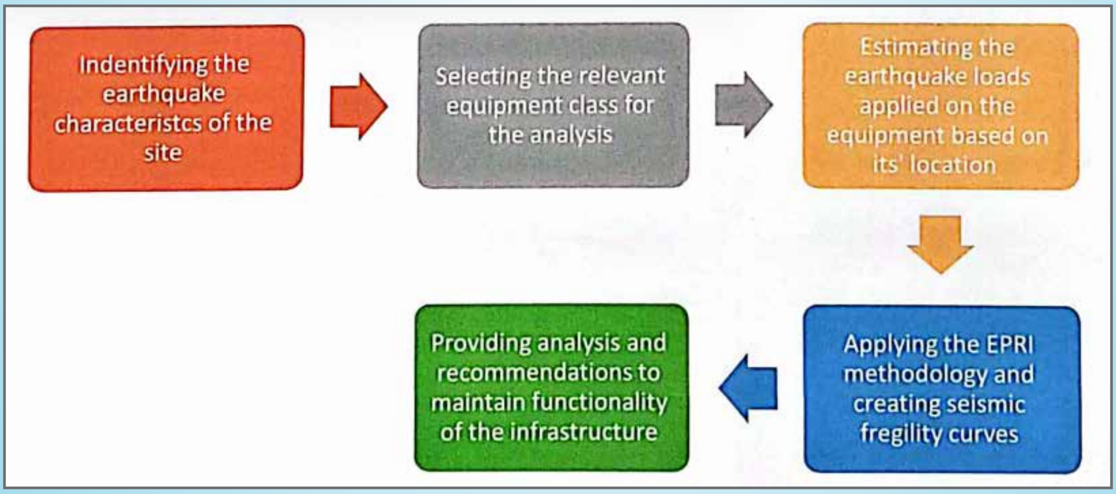

infrastructure Applying the EPRI methodology and creating seismic fregility curves The presentation will provide detailed description of the analysis and its' conclusions and recommendations to maintain functionality of the safety related infrastructure during and after strong earthquake motions.

Define Yamin Plain Wind Velocity Persistence and Long Term Correlations

S. Moshel and R. Neuman

We discovered unusual dynamic anticorrelations in wind patterns near the surface within the boundary layer (60 and 90 meters above ground). These anticorrelations become more pronounced during the summer months. This phenomenon can be attributed to the interactions between different air streams that lead to eddies and turbulent mixing, which may relate to a unique occurrence known as a low-level jet originating from the Mediterranean Sea, primarily observed in certain conditions; see (Kutsher, Haikin, Sharon, & Heifetz, 2012).

We focused on the temporal patterns of wind velocity and the persistence of the low level of the boundary layer using meteorological data from four wind sensors located at heights of 12 meters, 30 meters, 60 meters, and 90 meters in the Yamin plain, 100 m pole. Wind sensors were placed at different heights to capture variations in wind speed, direction, and temperature. We used the Detrended Fluctuation Analysis (DFA) method to define long-term correlations on a time scale by determining the fluctuation variation.

We found a significant variation in the wind velocity profile within the boundary layer at different heights on the pole. It became increasingly anti-correlated by height, specifically, as it moved upward from the sensor located at 60 meters height. This suggests that the wind velocity measured at 60 meters may act as a critical point in this scenario. The wind at a height of 90 meters was significantly more anti-correlated. This unusual wind profile is expected to affect the near-ground dispersion process and risk assessments.

Advanced Nuclear Siting- New Opportunities in the Israeli Case Study Presentation Abstract Submitted to the INS 31

Ami Nagler, Danny Grossman

To meet the challenges of energy security in the coming decades, Israel must prepare for a Nuclear energy build-out. After much work in the 80's and 90's an area suitable for a large (Giga scale) nuclear power plant was allocated near Shivta (in the South of Israel). Small modular reactors (SMRs) and Generation IV reactors offer the potential for significant advances in nuclear energy technology. Among these advantages are smaller safety distances (EPZ), improved seismic tolerances, and the reduced need for water sources nearby. We explore the siting areas in Israel for "traditional" vs. advanced nuclear power plants using ANSASadvanced nuclear siting-as-a-service expert system. SMRs and advanced Nuclear manifest a tight coupling between specific technologies, reactor sizes, and suitable siting locations. This can significantly impact the selection process of procuring a nuclear power plant. The presentation will show that using the latest Israeli regulatory guidelines and several examples of advanced reactors (vs. "traditional") opens many interesting possibilities for nuclear sites in Israel, previously excluded for large reactors.

This work is funded in part by the Ministry of Energy Chief Scientist project 223-11-012

Session 5- Simulation & Numerical Methods

Moderator: Erez Gilad

Benchmarking of the SPERT-III E-core experiment with the Monte Carlo codes TRIPOLI-4, TRIPOLI-5 and OpenMC

Antoine Dervaux[1], Shai Kinast[2], Matthieu Lemaire[1], Vincenzo Di Blasi[1], Coline Larmier[1], Davide Mancusi[1], Cyril Patricot[1], Andrea Zoia[1]

1 Université Paris-Saclay, CEA, Service d'Études des Réacteurs et de Mathématiques Appliquées, 91191, Gif-sur-Yvette, France

2 Department of Physics, Nuclear Research Center Negev, 8410501, Beer Sheva, Israel

A code-to-code verification of the SPERT-III reactor in its E-core configuration is presented using the Monte Carlo codes TRIPOLI- 4®, TRIPOLI-5® and OpenMC. A SPERT-III E-core model was originally developed for the Monte Carlo code TRIPOLI-4® and will be the baseline of our analysis The simulation results obtained for the main reactor physics parameters (neutron effective multiplication factor, rod worth, reactivity coefficients and kinetics parameters) with TRIPOLI-4®and OpenMC using different nuclear data libraries are compared and analyzed. Additional verifications are carried out with the nextgeneration Monte Carlo code TRIPOLI-5®, which is currently under development by CEA and IRSN (France). This work summarizes a joint study that was conducted within an international research collaboration between CEA ParisSaclay (France) and the Nuclear Research Center Negev (NRCN, Israel), and is a stepping stone towards future multi-physics simulations exploring the SPERT-III reactor power excursions, including thermal-hydraulics feedback.

Simulating the Impact of Electrostatic Fields on Electron Beam Additive Manufacturing Processes

Elroei Damri[1,2], Eitan Tiferet[2,3], Itzhak Orion[1]

1 *Department of Nuclear Engineering, Ben-Gurion University of the Negev, Beer-Sheva, 84105, Israel*
2 *Nuclear Research Center (NRCN), P.O. Box 9001, Beer-Sheva 84190, Israel*
3 *AM R&D Center, AM Center, Rotem Ind. Mishor Yamin 86800, Israel*

Background: Additive manufacturing (AM), commonly known as 3D printing, is a transformative technology capable of producing intricate components and structures from various materials. This technique involves layer-by-layer fabrication, directly creating complex geometries from metal powder beds. Ideally, the electron beam's kinetic energy is entirely converted into thermal energy, melting the powder. However, in real-world applications, the electron beam's interaction with cold powder particles can generate electrostatic charges due to the presence of a nanometer-thin oxide layer on the powder. This study investigates the significant influence of charging and the resulting electrostatic field on the AM process.

Methods: The EBM process approximated the electrostatic field using COMSOL Multiphysics simulations. Subsequently, EGS5 Monte Carlo simulations were used to analyze the impact of this field on process dynamics by defining electric fields on the metallic grains' surface.

Results: The simulations revealed significant findings. The simulations revealed that the electrostatic field within the EBM process is substantially stronger than previously reported, exerting a more significant influence on the process than other operational forces like momentum or friction. The magnitude of this field is influenced by various factors, including grain size and sintered grains. This electrostatic field affects electron scattering, thereby impacting energy deposition to the powder grains.

Discussion and conclusions: The simulations were instrumental in identifying the factors influencing the magnitude of the electrostatic field and demonstrating its dominance within the EBM process. This study found that specific characteristics, such as increasing the grain diameter of the powders, can enhance energy deposition efficiency under the same field conditions. These findings highlight the crucial role of the electrostatic field in optimizing the EBM process and understanding its underlying mechanisms.

Development and Benchmarking of a Relativistic Point Detector in Openmc

Itay Horin

Background: Monte Carlo simulations are widely used for neutron transport analyses, but estimating neutron flux at a point often requires specialized methods. Traditional point detectors rely on approximations or nonrelativistic approaches, which may not be suitable for high-energy neutron scenarios. There is a growing need for efficient and accurate methods to handle these challenges, particularly in complex shielding analyses and scenarios with poor simulation statistics.

Methods: This study introduces a relativistic point detector tally within the OpenMC framework. The detector incorporates full relativistic kinematic calculations to accurately estimate neutron flux at a point. Benchmarking was performed using single and multiple collision tests to validate the implementation against conventional methods.

Results: The relativistic point detector was successfully implemented in OpenMC. Validation tests demonstrated excellent agreement with traditional methods, confirming the accuracy and efficiency of the detector. These results highlight the suitability of the detector for high-energy neutron transport simulations.

Discussion and Conclusions: The development of a relativistic point detector enhances OpenMC's capabilities, providing a powerful tool for neutron flux estimation in challenging scenarios. By addressing limitations in simulation statistics and inefficiencies in traditional Monte Carlo methods, this advancement enables more precise analyses for complex shielding and high-energy neutron applications.

Comparison of Moment Closure and SDE Approximations of the Logistic Model

E. Magali, C. Dubi

1. Background: The Logistic Model in Equation 1 is a natural extension of the point kinetics model, where further growth is stymied as the neutron population grows. This often occurs due to feedback, where as the system heats up due to neutron interactions with the medium, the reactivity drops, which occurs for populations with relatively high number of neutron interactions.
$dN\ dt = \alpha N - \epsilon N2 + I$ (1)

The deterministic logistic model also has a corresponding stochastic branching process model, where the population growth takes into account the stochastic nature of the possible interactions, which is governed by a death and birth rate laws as per Equation 2:
$\gamma(N) = a1N - b1N\ 2$
$\lambda(N) = a2N + b2N\ 2$ (2)

where γ, λ are the birth and death rates of the point system, and ai , bi are non-negative system parameters. The (integer) number of progeny in a given birth, called the multiplicity, is also taken to be a random variable that follows a probability vector $(p\nu) \infty\ \nu=0$, which does not depend on the population size. The external source I is often stochastic in nature as well, and can be modeled by an immigration term in the branching process, where new individuals enter the system in a given time interval according to a Poisson behavior. The stochastic logistic model is thus of interest when the population size is large enough for the feedback to have a noticeable effect and while the stochastic behavior can still be differentiated from a purely deterministic model. This stochastic system is of interest in other fields of science, such as biology [1]. The full branching process can be cumbersome to model, so approximations are often used. In one family of such approximations, a set of cumulant equations is derived from the master equation, and a closure is assumed where the last cumulant is set to 0. These moment closure approximations yield a set of ODEs for the cumulants of the distribution, and from the values of these moments a specific distribution is chosen. These approximations leave a few things to be desired. First, the choice of a specific distribution given k cumulant values is somewhat arbitrary. Second, the solution gives a distribution at each time step, but does not yield a method to approximate specific realizations of the branching process.

We propose a different approximation, using Stochastic Differential Equations (SDEs), which we construct from first principles. SDEs are gaining traction as approximations to the stochastic behavior of neutron populations, especially in point systems [2, 3, 4, 5]. An SDE follows the general form of Equation 3:
$dX = \mu(X, t)dt + \sigma(X, t)dW$ (3)
where W is a Wiener process. SDEs can be easily numerically solved to obtain realizations of the system, which can be used directly. In some cases, they can also be analytically solved, which yields the distribution at any given time.

2. Methods: The master equations for the branching process are simply given in Equation 4:
$dAn\ dt = -An(t)\ a2n + b2n\ 2 + a1n - b1n\ 2 + I$
$+ (1 - \delta n,0)An-1(t)I$
$+ An+1(t)(a2(n + 1) + b2(n + 1)2\ ) +$
$nX-1k=1\ An-k(t)\ a1(n - k) - b1(n - k)\ 2\ \ p\nu(k)$ (4)

We derive a partial differential equation for the probability generating function of the branching process, given in Equation 5:

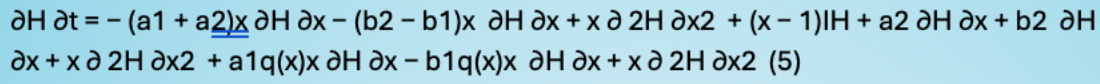
∂H ∂t = − (a1 + a2)x ∂H ∂x − (b2 − b1)x ∂H ∂x + x ∂ 2H ∂x2 + (x − 1)IH + a2 ∂H ∂x + b2 ∂H
∂x + x ∂ 2H ∂x2 + a1q(x)x ∂H ∂x − b1q(x)x ∂H ∂x + x ∂ 2H ∂x2 (5)

where q(x) is the probability generating function for the multiplicity. From this, the ODEs for cumulant equations are directly derived. The SDE model is written from first principles to be as in Equation 6:
dX = Idt − a2X + b2X2 − ν a1X − b1X2 dt + r I + X h a2 + b2X + ν 2 (a1 − b1X) i dW (6)

We then prove that its first two cumulant equations are identical to those derived from Equation 5. Given this approximation in hand, we then compare our model to a Saddlepoint Approximation used in biology [1] and a Gaussian approximation. In the Saddlepoint Approximation, which we will mark as K3, the fourth cumulant is set to 0, i.e. κ4 ≡ 0. Similarly, the gaussian approximation is marked as K2, as its third cumulant is set to 0. For small enough populations, Equation 4 can be solved if we assume that the population cannot grow too much above the carrying capacity, which gives us a reference solution for the branching process itself. We then compare moments of the SDE model (by simulating many realizations) to the other approximations against the reference. We will also compare the CDF of the different models, for different system parameters and at different times as the system goes from its initial condition to its stationary distribution around its carrying capacity.

3. Results: We currently have data for only some of the comparisons we intend to cover in full presentation. The relative error from the reference value for the SDE model and the moment closure approximations for the first two cumulants is given in Figure 1a and the absolute error in the third cumulant is given in Figure 1b. The values for the SDE were taken from 105 realizations. The SDE model is (up to our statistical significance) comparable in the first two moments to the K3 approximation and out-performs the K2 approximation. We hope to be able to differentiate the accuracy of SDE model from the K3 model in terms of their variance by the time of our presentation. The system values in this comparison are taken from data meant for mammals in Europe [1], which is why their time is measured in years. In our full paper we intend to show similar comparisons for other system parameters where the SDE is both more likely to fit (when the carrying capacity is large) as well as cases where it is expected to have worse performance. In our full paper we intend to include comparisons for the CDFs as well, especially around the initial time where we see a major difference in the relative skewness, as well as around the time of maximal skewness, and around the stationary solute.

4. Discussion and Conclusion: The SDE model we derived from first principles provides realizations that approximate the branching process itself. The model's third cumulant grows slowly compared to the reference but catches up fairly quickly before the system.

reaches its carrying capacity. Otherwise, the SDE model is comparable to the K3 model, but requires neither a somewhat arbitrary choice to obtain its distribution at any given time and can be used to generate realizations (sample paths) directly. In conclusion, the SDE model seems to be a fair candidate as an approximation to the stochastic logistic model. Future work to find a bound on its error could eliminate the need to test its accuracy against the reference for cases of interest and give a better mathematical understanding of its nature.

Development of a 2D PWR diffusion model with thermal coupling for control optimization

Y. Ben-Galim, Y. Weiss, E. Gilad

1. Background: Transient analysis of the neutron flux distribution and the thermal-hydraulic variables is necessary for control systems parameter optimization and analysis of accident development in a nuclear reactor. The former usually utilizes scalar-based mathematical models employing the point-kinetics equation and a simplified zero-dimension thermal-hydraulic model. In the latter, simulations are performed using advanced 3D models and codes for the neutron flux and thermal-hydraulic calculations. The spatial neutron flux distribution and thermal-hydraulic models are rarely used to analyze the transient response in conjunction with control logic models. Hence, control optimization often ignores the spatial power distribution and spatial neutron flux perturbations. Moreover, the effect of the control logic parameters is hardly examined in the analyses of accidents' evolution. This study introduces a 2D transient diffusion model for evaluating neutron kinetics (NK) coupled with a corresponding thermal-hydraulic (TH) model. The model also incorporates the control logic, which manages the control-rods movement to maintain the desired reactor power. The primary cooling system was modeled as well.

2. Methods: The methodology incorporates a mathematical model containing a set of two-dimensional neutron diffusion equations with two precursor groups and a thermal-hydraulic model for evaluating the fuel and the coolant temperatures within the core. A simplified primary coolant system (PCS) model is included as well. The adopted control algorithms are based on Westinghouse's power control algorithm [1] for average coolant temperature regulation. The Proportional-Integral (PI) controller effectively governs the core's inlet temperature by regulating the steam generator's secondary side water level and steam flow [2], [3] or pressure [4]. In this study, the model for the primary coolant system, adopted from [4], consists of delays in the lower and upper plenum, the hot and cold leg, and the steam generator inlet and outlet plenum.

The heat exchanging section of the steam generator model consists of five nodes: two for the primary fluid, two for the metal tubes, and one for steam. The proposed two-dimensional model enables a relatively fast spatio-temporal analysis compared to full-core three-dimensional calculations. Moreover, the model allows for studying spatial perturbations within the core's radial direction while maintaining a 0D-transient model for the primary cooling system and the control logic. The model was developed in MatlabTM

3. Results: The chosen reactor in this study is based on the EPRI1 9/9R PWR benchmark [5]. The validation of the static 2D NK diffusion model is presented in T, showing the difference between the proposed model and the benchmarks. The eigenvalues in the table are of the two cores, EPRI9 and EPRI9R, including all FAs and the baffle-reflector. As seen from the table, the model results with fine mesh agree with the benchmarks, thus validating the suggested static algorithm in the NK model.

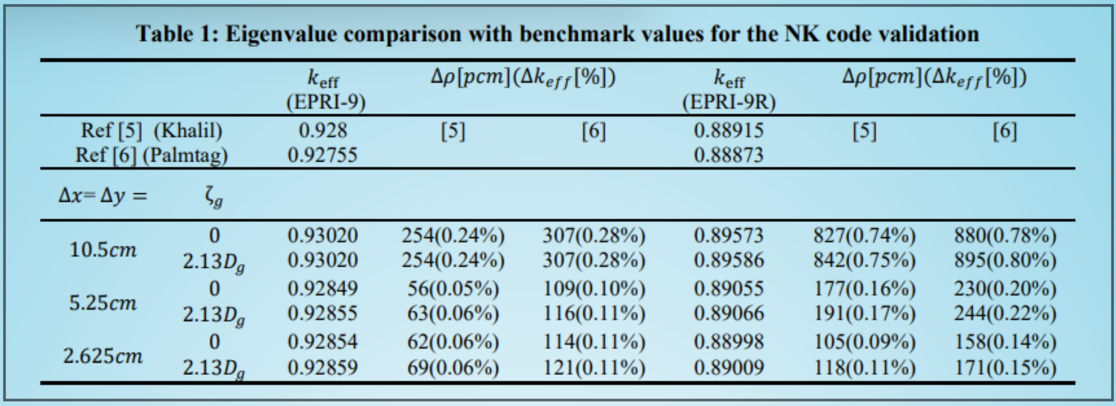

Table 1: Eigenvalue comparison with benchmark values for the NK code validation

		k_{eff} (EPRI-9)	$\Delta\rho[pcm](\Delta k_{eff}[\%])$		k_{eff} (EPRI-9R)	$\Delta\rho[pcm](\Delta k_{eff}[\%])$	
Ref [5] (Khalil)		0.928	[5]	[6]	0.88915	[5]	[6]
Ref [6] (Palmtag)		0.92755			0.88873		
$\Delta x = \Delta y =$	ζ_g						
$10.5cm$	0	0.93020	254(0.24%)	307(0.28%)	0.89573	827(0.74%)	880(0.78%)
	$2.13D_g$	0.93020	254(0.24%)	307(0.28%)	0.89586	842(0.75%)	895(0.80%)
$5.25cm$	0	0.92849	56(0.05%)	109(0.10%)	0.89055	177(0.16%)	230(0.20%)
	$2.13D_g$	0.92855	63(0.06%)	116(0.11%)	0.89066	191(0.17%)	244(0.22%)
$2.625cm$	0	0.92854	62(0.06%)	114(0.11%)	0.88998	105(0.09%)	158(0.14%)
	$2.13D_g$	0.92859	69(0.06%)	121(0.11%)	0.89009	118(0.11%)	171(0.15%)

The verification of the transient computations in the model was accomplished for a homogeneous 2D reactor with reflective boundary conditions (infinite core) having a medium with the parameters of FA F1 compared with a transient 0D numerical solution of the same equations (employing $\nabla f(x, y) = 0$) in MathematicaTM using the NDSolve function. The comparison for the evaluated NK (thermal and fast fluxes) and TH (fuel and coolant temperature) variables is presented in figure 1 and for selected PCS variables in figure 2. In each figure, the left side shows the simulation results side-by-side. The blue line ('2D') represents the result from the proposed model, and the orange line ('$\partial/\partial r \rightarrow 0$') represent the results from the MathematicaTM simulation. The right side of each figure presents the ratio between the simulation's variables defined as: $(f(2D)\ f(\partial\ \partial r \rightarrow 0) - 1)$. Note that PCS variables such as the steam pressure is affected by all the transients described in this work (NK, TH, PCS, etc.), and having a negligible error compared with a different code indicates that the overall computation is verified.

4. Discussion: This research introduces a novel tool that simulates two-dimensional NK-TH transients coupled with two control logic algorithms for the core's thermal power and the steam generator's pressure. In most PWR control logic optimization studies, spatial models are not considered. The suggested tool also incorporates the effect of the PCS and the control logic algorithms on the system. The neutron diffusion part of the code was validated against the EPRI benchmark. The transient modeling was verified by comparing our model results with a solution of the same equations in different software.

Reactor Optimization by Reinforced Learning

Deborah Schwarcz, Nadav Schneider, Gal Oren and Uri Steinitz

Monte Carlo (MC) methods are widely used for neutronic calculations in nuclear reactor design. However, optimizing reactor parameters remains computationally challenging due to the high degrees of freedom. Traditional evolutionary algorithms explore multiple parameters but often struggle to identify global optima. In contrast, reinforcement learning, when integrated with MC simulations, presents a promising alternative for efficient reactor optimization. In this work, we use a novel technique that combines machine learning with neutronic calculations called the OpenNeoMC platform. We present a system designed to evaluate reinforcement learning methods in reactor optimization. This benchmark involves optimizing a research reactor unit cell by adjusting fuel density and water spacing to maximize neutron flux while maintaining reactor criticality. The optimization landscape features two distinct local minima, making it a challenging test case for traditional algorithms. We employ multiple algorithms to explore the solution space and assess their ability to converge to the global optimum. Our findings emphasize the advantages of reinforcement learning in reactor optimization, particularly in scenarios where multiple local optima hinder traditional methods. By leveraging reinforcement learning, we achieve more robust and optimal solutions, contributing to advancements in nuclear reactor engineering. Future studies should explore these approaches in higher-dimensional parameter spaces and compare their performance with existing optimization techniques. This research paves the way for more efficient and effective reactor design and operation.

Session 6 – Radiation Detection & Measurements

Moderator: Alon Osovitsky

Low Level Activity Measurements of 241Am in Environmental and Biological Liquid Samples Utilizing Liquid Scintillation Counter

S. Cohen[1], Z. Akerman[1], R. Gonen[1], L. Carmel[1], M. Brandis[2], S. Tsroya[1]

1 Nuclear Research Centere-Negev, P.O.Box 9001 Beer Sheva 84190, Israel
2 Radiation Safety Department, Soreq Nuclear Research, 818000 Yavne, Israel

Radiopharmaceutical labs are responsible for the chemical preparation and production of different radioisotopes including the alpha emitter 241Am. The liquid waste created at these facilities is stored in tanks and routinely monitored by a counting system. Liquid wastes containing certain beta emitters at low activity concentrations can be discharged to waste water treatment plant (WWTP) for further disposal according to Israeli environmental laws and regulation limits. However, alpha emitters are restricted and cannot be discharged to WWTP due to their high radiotoxicity.

Today, 241Am is characterized and measured by low background gamma spectrometry systems with minimum detectable activity (MDA) and decision level (DL) of ~500 [mBq/l] and 250 [mBq/l] (MDA=2×DL), respectively. However, the derived recording level (RL) for an annual internal monitoring interval utilizing biological samples (e.g., Urine) is RL(241Am)=0.15 [mBq/l]. In addition, low concentration of 241Am are measured during nuclear decommissioning and nuclear forensics activities. Therefore, there is a need in reliable, high efficiency, low background counting systems for accurate activity measurements of 241Am.

In the present study, the MDA of 241Am in both acidic water solutions and urine samples were measured utilizing the liquid scintillation counting (LSC) system "Quantulus 1220". The effect of different LSC detection parameters on 241Am MDA were analyzed including: detector absolute efficiency, different types and volumes of scintillation cocktails and sample quenching.

It was found that the absolute detection efficiency of 241Am alpha decay in LSC Quantulus 1220 is ~100% as was found for other alpha emitters [1]. Increasing the scintillation cocktail volumes in both acidic water solutions and urine samples decreases the quenching effect causing a shift of the 241Am peak to higher channels with improved energy resolution. In addition, the results suggest that the observed shift to higher channels of both 241Am peak center and width is linear with increasing spectral quench parameter of external standard (SQP(E)) value. Therefore, low level activity of 241Am can be calculated at different SQP(E) range without an observable peak. However, background counts increase with increasing cocktail volume, causing higher MDA\DL. No statistical differences were observed between the two types of scintillation cocktails: Ultima Gold XR and Ultima Gold AB [2]. Analysis of different detection and counting parameters (e.g., background, efficiency, sample volume, etc.) suggests that the optimal sample to liquid cocktail volume ratio (ml) is 2:10. At this ratio, the calculated DL that was found for the Quantulus 1220 system at 3 days counting time for both water acidic solutions and urine samples is 0.26 [mBq/l] and 0.36 [mBq/l], respectively. These values are higher than the derived recording level required for internal monitoring but enable determination of low level activity of 241Am at LSC systems for liquid waste and environmental samples at different quenching values.

A System for the Detection and Quantification of Effluent Releases of Positron-Emitting Isotopes

Druzhyna S.[1], Mirzakandov R.[1], Semyonov N.[1], Samuel K.[3], Wengrowicz U.[1,2], Ginzburg D.[1]
[1] R......
[2} N......
[3} I.….

Background: Cyclotrons are used to produce radioisotopes for the Positron Emission Tomography (PET). During processing, radioisotopes are released into the environment through the ventilation ducts of the facility. It is necessary to monitor radioactive positron-emitting gases released into the environment through the exhaust duct. This paper describes the main design considerations for a detector developed at Rotem Industries for this purpose. The lifespan of positrons is very short, with only tens of microseconds until the positrons lose most or all of their kinetic energy and annihilate with an electron in the medium, causing the emission of two photons with an energy of 511 keV. This energy is equal to the rest mass of the electron or the positron. The energy penetration of these photons is very high, and it is challenging to differentiate between activity within the exhaust stack and "noise" from outer sources, such as photons emitted at the production site. In addition, it is necessary to identify positron-emitting isotopes, as different allowed release limits are set by the regulations for each isotope. Therefore, merely measuring 511 keV photons is not sufficient, as this energy does not reveal the initial energy of the positron and, consequently, does not permit the identification of the specific radioisotope. The measurement system that was developed is intended to be installed in the exhaust duct at positron production sites. The system is based on a pair of detectors for coincidence purposes: a) a NaI(Tl) scintillation detector PM11 [1-] calibrated to an energy window of 511 keV for annihilation photons detection and b) a positron detector based on a plastic scintillator coupled to a silicon photomultiplier (SiPM) photosensor and positioned in front of PM11 (from the perspective of the released effluents). Both detectors are connected to a data collection system, the Rotem WebiSmarts [2-]. The developed positron-gamma coincidence measurement system and the data collection unit are shown in Figure 1. The software module 'WebiMissions" provides an advanced reporting capability: a) report only on effluent within the exhaust duct and b) identification of the following positron-emitting isotopes: F-18, Ga68, O-15, C-11, N-13. Readings from the PM11 gamma detector within the desired energy window indicate the presence of positrons, but only simultaneous readings from both types of detectors attest to the emission of radioactive gases through the exhaust stack. The identification of positron-emitting isotopes is a much more complex task. Similar to beta decay, positron emission is not monoenergetic and is characterized by a maximum energy specific to each isotope. Additional considerations for the positron detector include reducing the sensitivity to energetic photons to optimize positron-to-gamma discrimination. This leads to optimal calculations of the scintillator thickness, which allows the positron to transfer all of its kinetic energy and allows maximum passage of the annihilation photons created in the plastic scintillator to the gamma detector. The placement of a SiPM on the side of the plastic scintillator has proven to be an effective means for collecting scintillation light, which also enables the free passage of 511 keV photons to the gamma detector. Identifying the energy of the maximum emission intensity of each isotope is very problematic because of the influence of adjacent events, pile-up effects, Compton electrons from background radiation, etc. However, identifying the maximum energy of the measured positrons, assuming that only a single positron-emitting isotope is released into the exhaust duct, has proven to be a much more reliable method. Because the ionization and electron excitation properties that cause scintillations are very similar for positrons and electrons, beta sources can be used to calibrate the detector. This calibration method links the sampled channel in the MCA to the energy transferred by the positrons in the scintillator.

Methods: Plastic scintillators are commonly used in the industry to detect and measure beta emitters and are also suitable for positron counting. Their main advantageous properties for beta measurements include high sensitivity to beta particles, fast response time, chemical stability that ensures durability and consistent performance over time, and ease of shaping and machining to desired forms [3-]. A low gamma-ray response can be achieved with a smaller thickness, which will aid in distinguishing between beta particles and gamma radiation. The diameter of the plastic scintillator in the developed detector was 2", geometrically matching the diameter of the gamma detector, PM11, behind it, allowing the packaging of both detectors in a mechanically rigid and convenient housing for easy installation in the exhaust duct at positron production sites. Because the dimensions of the SiPM are significantly smaller than the surface area of the scintillator, it is crucial to attach it firmly to the scintillator and ensure the quality of the reflector that wraps the scintillator. The use of Mylar™ at the scintillator's front is crucial for maintaining external light tightness; however, it must have a minimal possible thickness to prevent energy loss of the positrons passing through it to the sensitive area of the scintillator. In addition to the scintillator properties described above, it should be noted that the emission wavelengths of plastic scintillators typically fall within the range of 400-450 nm. SiPMs are designed to efficiently detect light in this wavelength range, making them a suitable choice for detecting the scintillation light produced by plastic scintillators. SiPMs are pixelated devices that are composed of numerous microcells. Each microcell is a series combination of an avalanche photodiode (APD) operating in Geiger mode and a quenching resistor (RQ). When a SiPM absorbs a photon, the resultant charge carrier can trigger an avalanche in the gain region, producing 105 -106 carriers. This avalanche generates a current pulse with charge Q flowing through the SiPM terminals. The SiPMs are externally biased to ensure that each APD operates above its breakdown voltage, where the cathode is positively biased with respect to the anode. The difference between the biasing and breakdown voltages is known as the overvoltage (OV); a higher OV results in a greater SiPM gain. Therefore, the primary adjustable parameter that controls the SiPM operation is the bias voltage.

The breakdown voltage of the SiPMs is dependent on temperature. To ensure a consistent response among the same type of positron detectors and to maintain stability across a wide temperature range, the developed detector incorporates a temperature sensor and digital potentiometer for the dynamic regulation of the bias voltage.

The polarity of the output pulse from the SiPM depends on whether the anode or cathode is used for readout. An output pulse from the cathode results in a negative pulse, whereas that from the anode results in a positive pulse. In the developed circuit, the cathode is connected to a positive voltage supply, and the pulse from the anode output is directly connected to the Vin - input of a Transimpedance Amplifier (TIA) [4-]. TIA is one of the recommended methods for converting a SiPM photocurrent pulse to a voltage pulse. TIAs can amplify very small input currents, making them sensitive enough to detect low-level signals and ideal for use with sensors such as photodiodes, APD, or SiPMs. They are designed to minimize noise and ensure that the output signal is clean and accurate. Their fast response times are crucial for the rapid processing of the short decay time of plastic scintillators and the fast response of SiPMs. TIAs operate linearly over a wide range of input currents, and their gain is primarily determined by the feedback resistor, Rf.

As shown in Figure 2, the SiPM photocurrent (Iph) pulse is converted to a voltage pulse relative to Rf, but with inverse polarity: Vout=-Rf×Iph. The pulse-processing circuit includes another inverting amplifier, causing the voltage pulse to have a positive polarity. This amplifier also functions as a buffer, and its analog output pulse can be sampled using an external multichannel analyzer (MCA). Additionally, it was connected in parallel to a series of comparators, each with a different reference voltage controlled by a microprocessor using a digital potentiometer (EPOT). This setup enabled the creation of a series of energy windows.

Based on the assumption that only a single nuclide is used at a PET imaging site at any time, it is possible to set a series of energy windows according to the maximum energy of the emitted positron. The highest energetic positron-emitting nuclide for PET applications is Ga-68, with an Emax of 1899 keV; the energy threshold for this window is set to 1750 keV, slightly above the maximum energy of O-15, with an Emax of 1730 keV. Pulse counts in this energy window indicate the detection of positrons originating from Ga-68. Similarly, the lower threshold of the next energy window was set to 1230 keV, which is slightly above the maximum energy of the positrons emitted from N-13 with an Emax of 1200 keV. Counting pulses in this energy window without readings in the highest energy window indicates the emission of O-15. The energy windows for other PET nuclides were calibrated in a similar manner.

Results: The analog output pulses from the developed detector were measured using an external MCA. The detectors were calibrated using beta-emitting isotopes Sr-90\Y-90 with an Emax of 546-2280 keV and Cl-36 with an Emax of 710 keV. A Sr\Y-90 spectrum measured by MCA, presented in Figure 3 matches the theoretical spectrum of beta emission from these isotopes[4- 5-]. Because PET imaging uses a limited number of radionuclides, the energy windows presented in the Rotem WebiSmarts software allow reliable and simple identification of radioactive gas emissions of positron emitters released into the air through the exhaust duct at PET isotope production sites.

Discussion and conclusions: Initially developed system [6] of Stack Monitoring System for PET Medical Cyclotron Facilities showed promising results for on-line system implementation. Further re-design includs adjustment of electronic components, finalization of assembly process and optimization of data processing and allows to achieve stable performance and reliable monitoring of gas effluent of cyclotron facility that compatible to the requirements of international standards that determines common characteristics of the system in the field [7]. Further reporting of the results for system performance based on response to the nuclear material of interest (F18, Ga68) and compatibility to the international standard will be published elsewhere.

Figure 1 - WebiSmarts system consisting of beta/positron and gamma radiation detector and data collection unit

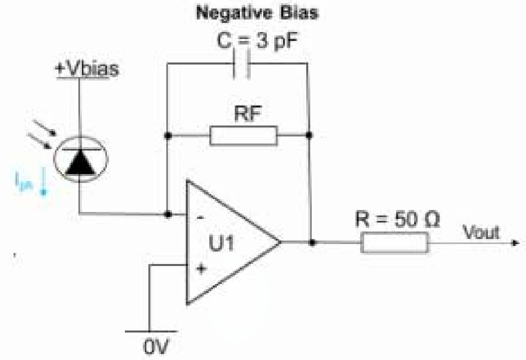

Figure 2 - Direct SiPM photocurrent to voltage pulse using a Transimpedance amplifier (TIA) [2]

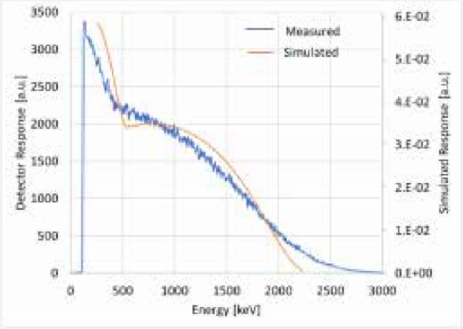

Figure 3 – Rotem beta/positron output signal for Sr/Y-90 source measured with external MCA [5].

Advanced High-Sensitivity Multi-Layer Neutron Detectors Utilizing LiF:ZnS(Ag) Scintillators for Homeland Security Applications

Ilan Cohen Zada[1,2], **Itzhak Orion**[2], **Michael Faziev**[1], **Tamar Kalman**[1], **Hila Shulgin**[1], **Dimitry Ginzburg**[3], **Shay Dadon**[1], **and Alon Osovizky**[1,3]

1 Electronics & Control laboratories, Nuclear Research Center Negev, Israel
2 Ben-Gurion university of the Negev
3 Radiation detection Department, Rotem Industries Ltd, Israel

This study introduces an innovative multi-layered neutron detector design utilizing LiF:ZnS(Ag) scintillator and a transparent neutron moderator. Each scintillator layer is integrated with a neutron moderator that also serves as a light guide for the Silicon Photomultiplier (SiPM) sensor. This configuration presents a promising alternative to 3He tube, addressing the ongoing shortage of 3He gas. The design is highly scalable, enabling flexible scale-up configurations to meet specific user requirements. Moreover, it offers significant improvements in sensitivity and operational data.

To measure neutrons using 3He or LiF:ZnS(Ag) sensors, neutrons need to be thermalized by a moderator. The final detector sensitivity is determined by the intrinsic sensitivity of the neutron sensor and the efficiency of the moderation process. This moderation process reduces the number of neutrons reaching the detector surface in two ways:

1. Direction Change: As neutrons move through the moderator, they collide with the moderator material, transferring some of their kinetic energy and changing their direction. Moderating materials like hydrogen, which has a similar mass to a neutron, cause significant direction changes during collisions.
2. Neutron Absorption: Neutrons can be absorbed by the moderator through a neutron capture process, which reduces the number of neutrons available for detection.

By adding active neutron sensor layers within the moderator, detection efficiency can be increased by measuring thermalized neutrons before they are scattered or absorbed by the moderator. This method takes advantage of the correlation between low-energy neutrons and scattered neutrons. The initial focus of the research was optimizing a single-layer detector configuration to maximize sensitivity while maintaining effective gamma-ray rejection capabilities. The optimization involved several parameters, including the size and location of the light sensor, as well as the type of reflector used. The optimized single layer is then replicated to form a multi-layer structure, mitigating the limitations of the LiF: ZnS (Ag) scintillator, namely its opacity, which restricts the thickness and efficiency of traditional detectors. By employing thin scintillator layers in each component, the proposed design minimizes light attenuation while simultaneously enhancing sensitivity through the cumulative effect of the multiple layers.

Experimental results demonstrate a substantial improvement in detection efficiency compared to the single-layer setup. The multi-layer design not only enhances neutron detection but also improves the differentiation between neutron and gamma signals. This was achieved through a detailed analysis of count rates across the layers, enabling the prediction of the source direction and providing valuable operational insights. Specifically, the multi-layer configuration achieves a 329% increase in sensitivity relative to a single-layer setup, while maintaining extremely high gamma rejection performance. The proposed detector offers several advantages over traditional solutions. The use of the LiF:ZnS(Ag) scintillator, which is a non-hygroscopic and stable material, addresses the limitations associated with conventional neutron detectors. Additionally, the design improves neutron moderation efficiency by minimizing neutron loss during the moderation process, which is a common challenge in thermal neutron detection.

Overall, this research introduces a promising new direction in neutron detection technology, combining the benefits of multi-layered configurations with the high neutron capture crosssection of LiF:ZnS(Ag). This paves the way for more efficient, cost-effective, and versatile neutron detection systems across various applications, including homeland security.

Keywords: Neutron Detection, LiF:ZnS(Ag), Silicon Photomultiplier, Gamma Ray Rejection, Neutron Moderation, 3He Alternative.

Subdividing Scintillator-based Compton Cameras with Constant Readout Channels for Improved Spatial Resolution

Z. Davidov[1,3], **M. Ghelman**[2], **A. Osovizky**[2,3] **and Nir Shlezinger**[4]

1 Israel Atomic Energy Commission (IAEC)
2 Electronics and Control Laboratories, Nuclear Research Center Negev (NRCN)
3 Department of Health Physics Instrumentation, Rotem Industries Ltd.
4 School of ECE, Ben-Gurion University of the Negev

A scintillator-based Compton camera (CC) is a γ-ray detector, often utilized for medical imaging, astronomy, and homeland security. In these applications, high spatial resolution is vital for accurately identifying tumors, resolving distant celestial objects, and guiding decontamination efforts following nuclear incidents. Degradation of the spatial resolution is significantly caused by uncertainty in the interaction positions within the camera. The accuracy of the interaction positioning depends on the size of each scintillator, often referred to as a voxel. Decreasing the voxel's size reduces the positioning uncertainty, which in turn, improves the spatial resolution of the reconstructed image. Decreasing voxels size will decrease the CC volume, which in turn, will reduce its sensitivity. Therefore, we suggest not changing the volume of the CC during this process. This results in the addition of voxels, which in turn requires more readout channels. The addition of readout channels increases power consumption, required electronics, and acquired data to process.

In this study, we introduce a novel approach to divide the volume of a CC into more voxels without adding more readout channels. This is achieved by connecting each readout channel to groups of voxels. When acquiring events from groups of voxels, it is impossible to determine in which of the group's voxels the event occurred. Thus, in addition to the true event, many "pseudo" events are considered in the data set.

This concept is illustrated in Figure 1. The addition of the "pseudo" events implies that the assumptions on the data acquisition procedure based on which the widely-in-use Maximum likelihood expectation maximization (MLEM) algorithm is designed, no longer hold, necessitating its adaptation. We utilize knowledge about the groups' formation to develop a new image reconstruction algorithm that extends the MLEM for voxels-grouped CC. We evaluated the resolution enhancement achieved with voxel grouping through simulations. Using the GEANT4-based Architecture for Medicine-Oriented Simulations (GAMOS) software, we simulated setups with single and two adjacent 137Cs γ sources. Various voxel grouping sizes were tested to assess spatial resolution improvement with increased voxel count through grouping. The resulting Compton images are shown in Figure 2 and Figure 3 for grouping sizes of $G = \{1, 4, 16\}$ and a constant number of readout channels $R = 50$. The results systematically demonstrate that voxels grouping method with our extended MLEM leads to better γ-ray sources localization and separation without adding more readout channels. This novel approach holds the potential for developing high spatial resolution, costeffective, and mobile CCs.

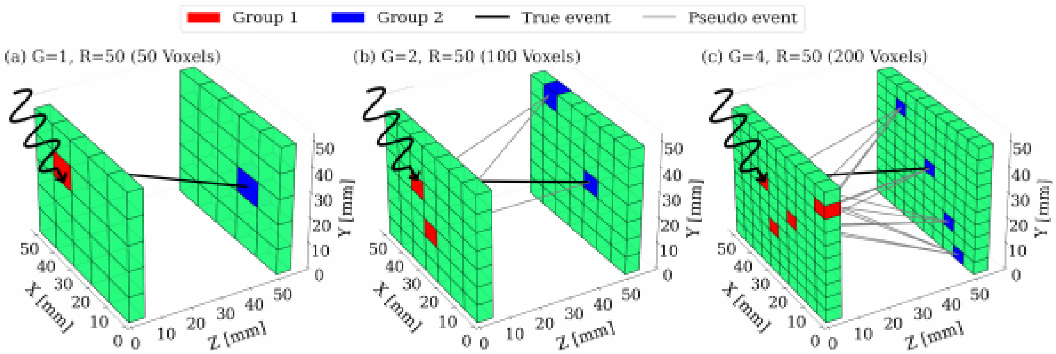

Figure 1: Subdivision of the CC with (a) 50 voxels and 50 readout channels (1:1 readout ratio). The number of readout channels is fixed at $R = 50$, with voxel grouping at different group sizes: (b) $G = 2$ for a CC with 100 voxels, and (c) $G = 4$ for a CC with 200 voxels. Each configuration involves a single true event triggered by an incident photon, with pseudo events in (b) and (c).

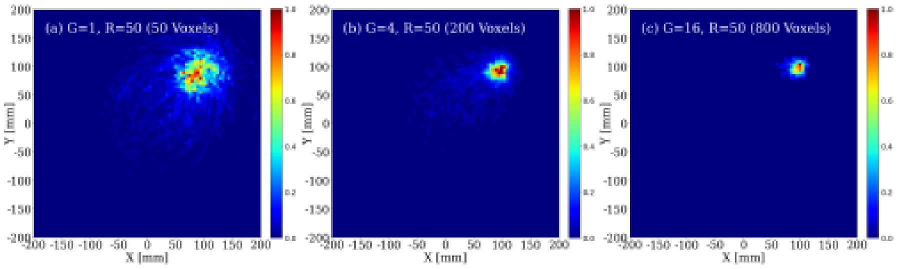

Figure 2: Reconstructed images of ^{137}Cs point source located at (100 mm,100 mm) from 1500 recorded events using a CC with 50 readout channels and (a) 50 voxels, G=1 , (b) 200 voxels, G=4, and (c) 800 voxels, G=16. (a) is 1:1 ratio readout , whereas the proposed Grouping method was applied for (b) and (c).

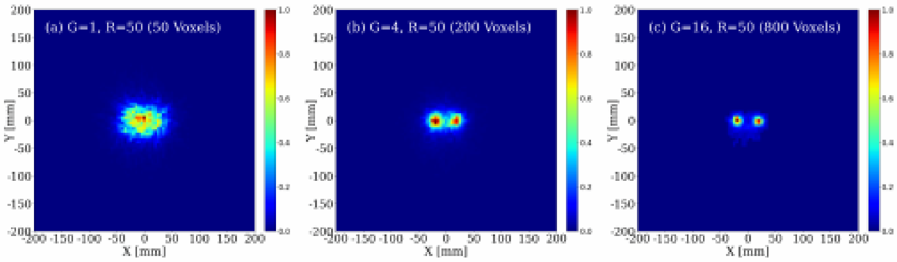

Figure 3: Reconstructed images of two ^{137}Cs point sources located at (± 20 mm,0) from 1500 recorded events per source using a CC with 50 readout channels and (a) 50, G=1 , (b) 200, G=4, and (c) 800 voxels, G=16. (a) is 1:1 ratio readout , whereas the proposed Grouping method was applied for (b) and (c).

Optimization of light-cone geometry for scintillation light collection to silicon photomultipliers in fast neutron multiplicity counting

M. Faziev[1,2], Y. Ifargan[2], Y. Yehuda-Zada[2], D. Smadja[2], E.O. Cohen[3], and L. Arazi[1]

1 *Unit of Nuclear Engineering, Faculty of Engineering Sciences, Ben-Gurion University of the Negev*
2 *Electronics & Control laboratories, Nuclear Research Center Negev, Israel*
3 *Physics Department, Nuclear Research Center Negev, Beer-Sheva, 84190, Israel*

Passive neutron multiplicity counting (NMC) is essential for monitoring fissile samples in nuclear facilities for radiation protection and nuclear waste treatment. Traditional NMC uses 3He tubes embedded in polyethylene moderators, but limited 3He supply has driven interest in fast-neutron multiplicity counting (FNMC),based on organic scintillators. FNMC enables direct measurement of coincident signals, with potential advantages over traditional NMC.

In this work we explore a key aspect of FNMC systems: the potential benefit of using light concentrators ("light cones") to enhance the light collection efficiency of centimeter-size plastic scintillators when using millimeter-size silicon photomultipliers (SiPMs) for light readout. We designed and assembled a dedicated measurement setup with a 2×2×5 cm3 plastic scintillator coupled to a light cone of various dimensions and read out using a calibrated photomultiplier tube over an active area of 6 × 6 mm2 . Our measurements, complimented by a dedicated realistic Monte-Carlo simulation, show that, counter-intuitively, for centimeter-size scintillators, there is no advantage in using light cones for increasing the light-collection efficiency to a mm-scale photosensor. The optimal configuration is rather a direct contact between the photosensor and scintillator (where the entire outer surface of the scintillator is coated by a reflector, except for the area in direct contact with the detector.) Further computational simulations reveal that light cones offer an advantage in a different aspect: when coupled to scintillators of larger dimensions than used in our experiments, light cones improve the time resolution of particle detection. The longer the light cone (i.e., the smaller its opening angle), the better the time resolution.

The conclusions drawn from this study contribute to the design optimization of both future FNMC systems and fast-timing detectors in experimental nuclear and particle physics. We will present our measurement setup as well as a complimentary Monte-Carlo simulations apparatus, and the surprising results of our study

Optimizing Silicon Passivated Implanted Planar detector for Alpha detection – Resolution Investigation

Eliran Evenstein*, Oriya Sabag*, Shoval Zoran, Gil Atar, David Rubinstein,
Ilan Goldward, Mantefardo Alefe, Ohad Westreich, Doron Choen-Elias and
Moran Bin-Nun

This study introduces a high-resolution alpha detector utilizing Passivated Implanted Planar Silicon (PIPS) technology. By systematically investigating the effects of detector diameter, source-detector distance, and dead layer composition, we demonstrate that tailoring these parameters can significantly enhance energy resolution. The proposed ring contact design further optimize detector performance, making PIPS detectors a robust choice for alpha-particle detection applications.

Passivated Implanted Planar Silicon (PIPS) detectors have gained popularity for alpha-particle detection due to their high crystalline quality, excellent carrier transport properties, and cost-effectiveness. These detectors maintain functionality even after exposure to high radiation doses, such as 105 Gy irradiation. Energy resolution, the precision with which the detector can distinguish between different energies of incident particles, is influenced by factors such as the dead layer thickness, electronic energy loss straggling, leakage current, and the incident angle of particles. This study systematically tests these variables and explores different detector diameters and source-detector distances to enhance energy resolution. We also investigate the effects of different dead layers, including SU8, metal, and SiO2, and propose improvements such as a ring contact design and a shallower junction to minimize interference and improve resolution.

PIPS detectors with diameters of 3 mm, 6 mm, 18 mm, and 24 mm were fabricated using standard CMOS processes on an n-type high resistivity silicon substrate. Alpha particle detection spectrometry measurements were performed using a BSI Amber-2 alpha spectrometer under air or vacuum. The SRIM software simulation package was employed to predict the energy loss of ions for various device configurations. Measurements at a fixed distance of 10 mm with a 5 mm radius Am241 source showed minimal resolution differences between edge cases (3 mm and 24 mm). Source-detector distance measurements under air and vacuum conditions demonstrated that shorter distances increase detection rates but may introduce background radiation and environmental interferences. Longer distances reduce background noise but lower particle flux and detection efficiency.

The dead layer, a region where ionizing radiation deposits energy without producing a measurable signal, significantly influences detection efficiency, particularly for low-energy particles. Thicker dead layers shift the energy threshold, making it harder to detect low-energy particles. SRIM simulations predicted energy loss in various device configurations, showing the impact of dead layer composition on detection efficacy. The source diameter influences the uniformity and intensity of the particle beam. A smaller source diameter produces a more focused beam, enhancing resolution and sensitivity. A larger source diameter generates a more diffuse beam, leading to a more uniform detector exposure but potentially weaker signals. Precise control systems are required for optimal performance with larger source diameters.

Dual-source energy calibration under vacuum demonstrated stable channel readout. The study's results highlight the importance of tailoring device parameters to achieve optimal detection efficiency and resolution, making PIPS detectors suitable for a wide range of alpha-particle detection applications. In summary, this research underscores the versatility and efficiency of PIPS detectors in alpha-particle

detection. By meticulously analyzing and optimizing key parameters, we have not only enhanced the detectors' performance but also paved the way for their application in various fields requiring highresolution and robust radiation detection. Future work can build on these findings to further refine detector design and explore new materials and methodologies to push the boundaries of detector sensitivity and efficiency.

Key words: PIPS detectors, alpha spectroscopy, high resolution,

Session 7 - Chemistry, Materials Science & Nuclear Forensics

Moderator: Erez Cohen

Active Neutron Multiplicity Counting With A Non-Poissonian Interrogation Source

E. Cohen, C. Dubi, R. Yankovich

Active Neutron Multiplicity Counting (ANMC) methods utilize an inversion formula to extract the intensity of a fission source. This is achieved by analyzing the sampled moments of the count distribution, which are generated through the process of inducing fissions in the sample using an external interrogation source.

ANMC serve as a powerful tool for quantifying fissile mass e.g., for uranium quantification in mines, fuel fabrication facilities, and reprocessing plants. Typical ANMC methods employ Poissonian interrogation neutron sources, such as AmLi, which emit a single neutron at each source event.

In this study, we expand upon the conventional formulas used in ANMC inversion to accommodate non-Poissonian interrogation sources. Specifically, we derive analytical expressions for the rates of Singles and Doubles events in ANMC systems. This advancement holds practical significance as it enables the future implementation of ANMC methods utilizing external sources with correlated neutrons, such as AmBe or 252Cf.

Aligned with established formulas, the derived formulas in this study adhere to the single-group model and incorporate the influence of fission chains through the widely recognized Bohnel method.

Methods in Metallurgical-Mechanical Integrity Assessment of Irradiated Aluminum Reactor Components

N.U. Navi, J. Cook, Y. Shaposhnik, D. Hix, D. Sahin

The National Bureau of Standards Reactor (NBSR) is a research reactor primarily utilized by the NIST Center for Neutron Research (NCNR) for neutron-based experiments. The reactor reached its first criticality in December 1967 and was initially licensed to operate at 10 MW, with an increase to 20 MW in May 1985. The mechanical and metallurgical integrity of the 5052-O aluminum (Al) vessel wall and selected 6061-T6 Al components of the NBSR were assessed. Data from the literature, combined with Monte Carlo N-Particle Transport (MCNP) mapping, indicated that by 2049, some 6061-T6 Al components are expected to exceed a thermal neutron fluence of 31×1026 m-2 , beyond which metallurgical-mechanical instability may occur. The reactor vessel wall is expected to maintain mechanicalmetallurgical stability up to 2049, with swelling estimated to be less than 0.1 %. Literature reviews are completed to utilize available tensile strength values for irradiated Al alloys to conduct stress analysis. The irradiated KIC values of 5154-O Al can be used for fracture analysis approximation of the 5052-O Al vessel wall. However, an estimated KIC value for highly irradiated 6061-T6 Al may need further verification.

Aerogel Spacer in Fission Tracks detector From star to super-star Image Processing

Babayew Rami, Yaacov Yehuda-Zada, Galit Bar, Elgad Noam, Last Mark, Jan Lorincik, Itzhak Orion, Shay Dadon, Aryeh Weiss, Galit Katarivas Levy, Halevy Itzhak

Fission Track Analysis (FTA) well known technique in nuclear forensics, enabling the identification of nuclear materials through the examination of fission tracks in SolidState Nuclear Track Detectors (SSNTDs). In our study enhances FTA by integrating advanced image processing techniques with both real and synthetic fission track data, improving detection, classification, and property reconstruction. Real data provides physical insights, while synthetic data offers controlled environments for testing algorithm performance and detector response.

Monte Carlo simulations using GEANT4 (v10.6) were employed to model fission product trajectories. Additionally, we developed the “FTA Trainer” application to generate synthetic fission track clusters on real SSNTD background images, enabling scalable and configurable data generation (36 pixels = 1 μm). These datasets were used to develop and validate image processing algorithms for pattern analysis and property reconstruction of fission track clusters. Fission Tracks Pattern Reconstruction of simulated and real star are depicted in Fig 1 and Fig 2.

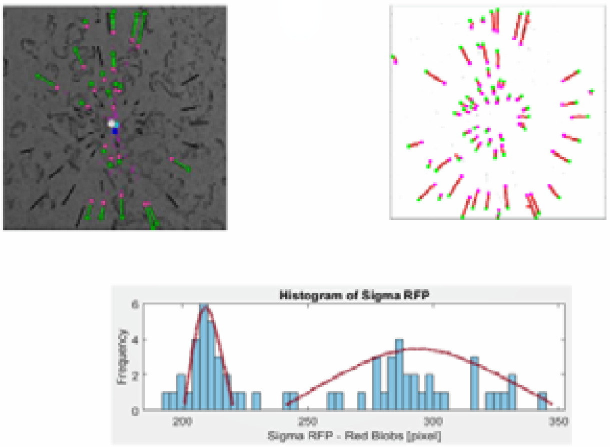

Fig. 1: Fission Tracks Pattern Reconstruction of **simulated** star.

Analysis of real fission track data (‘Soreq’ Reactor) validated our automated processing approach, revealing challenges such as noise, background artifacts, and overlapping tracks that necessitate advanced filtering. Despite limited statistics, our methodology proved effective for fission property reconstruction.

Analysis of real fission track data (‘Soreq’ Reactor) validated our automated processing approach, revealing challenges such as noise, background artifacts, and overlapping tracks that necessitate advanced filtering. Despite limited statistics, our methodology proved effective for fission property reconstruction.

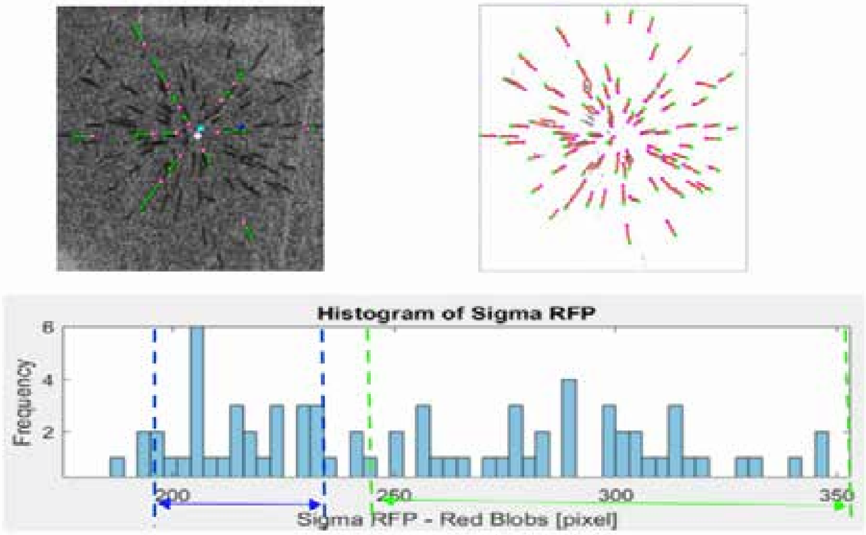

Fig. 2: Fission Tracks Pattern Reconstruction of **Real** star.

First steps on integrated **Aerogel Spacer** are shown in this preliminary work.

into the experimental setup to enhance statistical significance. Current GEANT4 simulations of aerogel-coated SSNTDs will be followed by experimental validation at the Soreq Nuclear Reactor.

Fission Tracks Pattern of simulated star with different Aerogel Spacer are shown are depicted in Fig 3. The enlargement of the Fission Tracks Pattern and the batter separation between the tracks enable better and easier analysis.

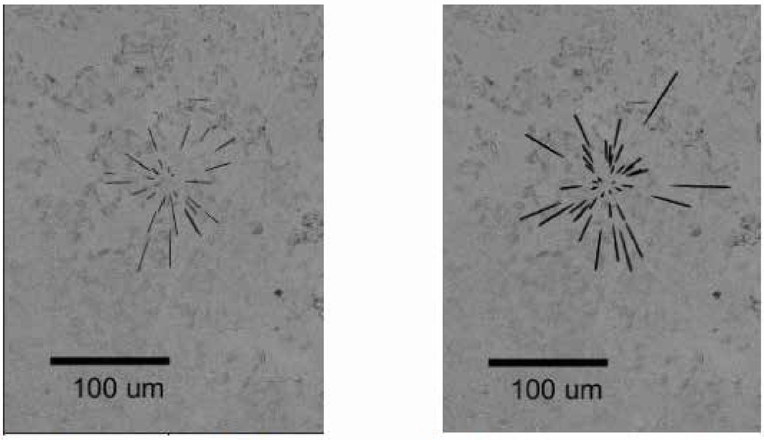

Fig. 3: Fission Tracks Pattern of **simulated** star with different **Aerogel Spacer**.

Resonant Raman scattering in f-electron, fluorite-type oxides

Tsachi Livneh

Face-centered cubic fluorite-structure oxides are uniquely capable of supporting oxygen vacancies (MO2-x) as well as incorporating oxygen within interstitial sites (MO2+x). Therefore, depending on the presence and the nature of cation multivalency, fluorite ceramics exhibit structural complexity, with technological applications spreading from nuclear fuels to solid oxide fuel cells.

Structural and electronic properties of f-electron, fluorite-type oxides of CeO2 [1] ThO2 [2] and UO2 [3, 4], explored under ambient and high pressure/low temperatures conditions, are elucidated by Raman scattering spectroscopy. Their spanned electronic structures and (multi)valent nature (Ce3+,4+, Th4+, U4+,5+,6+), dictate their resonant Raman response through Fröhlich interaction-induced multiLO scattering [1-4] (see Fig. 1 for CeO2 [1] and Fig. 2 for UO2 [4]). Remarkably, spectral analysis allows for this diverse set of oxides to be brought under a common physical framework.

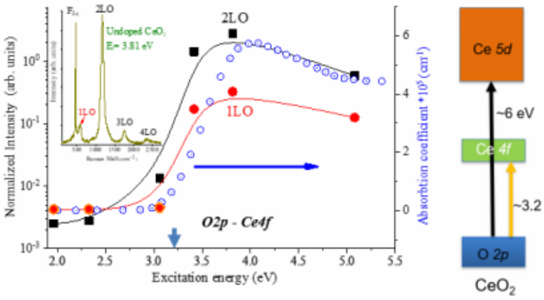

Fig. 1

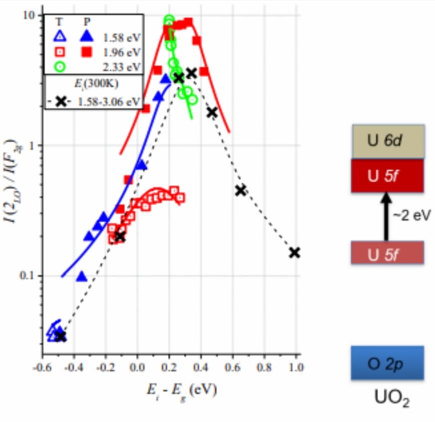

Fig.2

Order-Disorder Transitions in Cerium and Praseodymium Hydrides, Manifested in Temperature-Dependent Raman Scattering Spectroscopy

Shahar Aziza, Shmuel Hayun and Tsachi Livneh

Background: Lanthanides form a wide range of non-stoichiometric hydrides ($LnH2\leq x\leq 3$). They are extensively studied due to their potential usage in devices as a result of their tunable electronic/optical properties; "switchable mirror"devices and fast ionic conductors are two well-known applications [1] Cerium hydrides are characterized by a series of electronic and structural transitions, both composition and temperature dependent. Order-disorder transitions, driven by octahedral Hsublattice rearrangements, which,as temperature decreases, give rise to a tetragonal distortion of the cubic unit cell, was the mechanismpreviously proposed for the metal-semiconductor transition at ~245 K in the $CeH2+x$ ($0.7<x<0.8$) [2].The goal of this research is to study the effect of temperature on the interrelation between the structural features and electronic characteristics of cerium and praseodymium hydrides ($LnH2.25\leq x\leq 3$, Ln= Ce, Pr) by Raman scattering spectroscopy, using its sensitivity to fundamental structural (phase and long/short range order) and electronic properties.

Methods: $LnH2.25\leq x\leq 3$ (Ln= Ce, Pr) samples with $Dx \approx \pm 0.02$ were synthesized by exposure of polished samples of Ln metals to clean hydrogen/deuterium atmospheres. Phononic and electronic (crystal-field) Raman scattering of the samples were explored within the temperature range of 77-345 K and supported by DFT-calculated phonon dispersion curves and ab-initio calculations with an embedded cluster model. Our study is correlated with broadly explored investigations of the "twin system" of lanthanide hydrides, which is known to exhibit a highly similar temperature-composition phase diagram.

Resutls:

Fig.1

a) Temperature-dependent Raman of $CeH_{2.79}$ in the range of 198-268 K.

b) Spectra measured before (243K-cubic) and after (238K-tetragonal) the phase transition.

c) The intensity ratio of two characteristic bands that follow the phase transition, compared to DSC measured in [3].

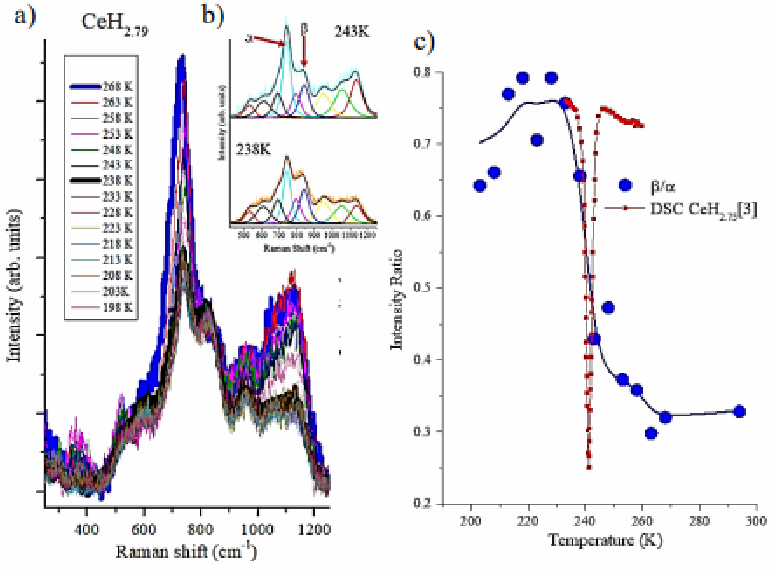

Discussion and conclusions: In this study, we demonstrate for the first time that the highly accessible experimental method of Raman scattering can closely track the phase transition in $CeH2.79$ (Fig1. a-c) and $PrH2.77$. This method allows for temperature resolution of just a few degrees by monitoring phonons attributed to the tetrahedral Hsublattice. Quite remarkably, this phase transition is also clearly manifested in electronic Raman scattering, which is also sensitive to the crystal-field scheme around the Ce3+ ions.

Raman spectrum of CeH2.94 is dominated by a band which is positioned within an energy gap in the calculated phonon dispersion curve of the BiF3-type cubic CeH3. The existence of additional (orthorhombic) phase, found both experimentally and theoretically for LaH~3 may explain this result. Indeed, displacement from the welldefined Wyckoff positions, arguably driven by H-H repulsions are found in all hydrides, but those questionably hold responsible of causing the observed PDOS spectral profile of long-range order hydrides.

It is suggested to stem from facile diffusion-like motion of Hions in between adjacent sites; as found in highly anharmonic superionic materials, dynamic sampling over a local-scale structural motif strongly modulates the average long-range structure, leading to what is spectroscopically manifested as enhanced disorder.

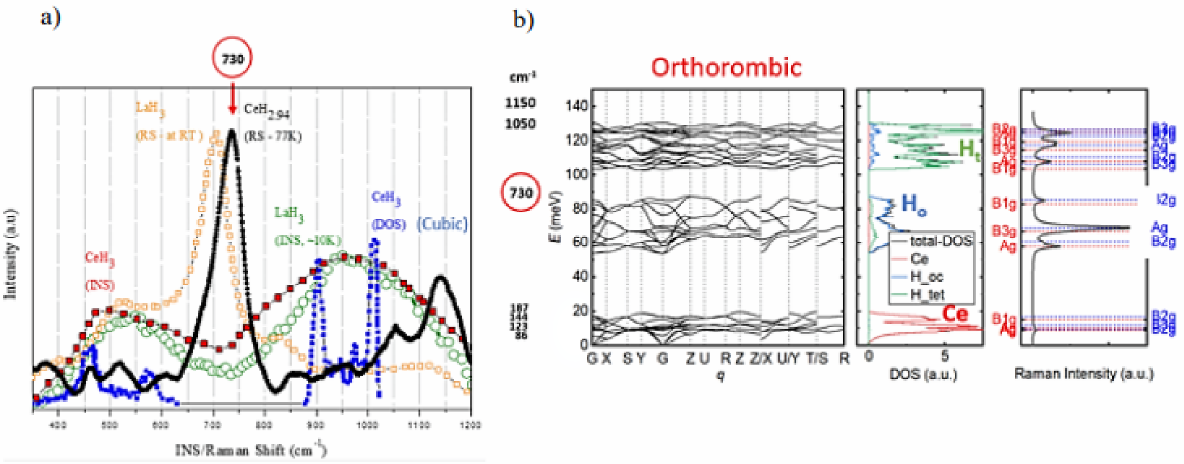

Fig.2 a. LaH_3 (RS) - Raman (orange squares) [4], $CeH_{2.94}$ (RS) - Raman (black circles) [this research], LaH_3 (INS) inelastic neutron scattering (empty circles) [5], CeH_3 (INS) inelastic neutron scattering (red squares) [6], Cubic CeH_3 (DOS) density of states (blue squares) [7]. ~705cm^{-1} and ~740cm^{-1} Raman peaks are not manifested in the cubic DOS. b. DFT calculated phonon dispersion curves of orthorhombically distorted structure (Pnma - D_{2h}^{16} (No. 62) symmetry CeH_3. Also shown are the phonon DOS and calculated Raman spectrum with the G-point Raman-allowed modes denoted with their respective symmetries.

Session 8 – Safe Management of Radioactive Waste

Moderator: Ofra Kilen Ben David

Shallow radioactive waste repositories and surface processes – importance and relevance

Noa Balaban, Jonathan Laronne, Sarah Adar, Ilay Hanegbi, Avi Bouskila

When considering risks to near-surface radioactive waste repositories, the main issue is spread of waste to the biosphere. There are two main mechanisms that pose as risks for this scenario:

The only near surface, radioactive waste disposal site in Israel is located in the Yamin Plain. The Yamin plain resides in an extreme desert, and its surface is composed of a sand rich formation. Under the current climate conditions, erosion and especially fluvial erosion during flow events and extreme floods, are the dominant processes changing the landscape in the region.

Surface properties such as lithology, slope direction, vegetation, animal activity and biocrust all have effect erosion and its rates in the Yamin Plain. Understanding these processes, while identifying the main parameters is crucial to the development of a is a long-term landscape evolution model of the Yamin Plain. This landscape model will be used to perform risk assessments on the shallow repository site, as well as for practical issues such as constant repository barrier design.

Our main prerogative is obtaining a good grasp of the hydrometric processes in this area, monitoring and establishing the connection between rainfall-runoff -sediment. Four basins of increased area (200-19,000 m2), are monitored by combining onsite hydrometric data and topographic structure from motion techniques, with an additional larger basin of almost 11 km2 on the Yamin Channel. 12 rain-runoff events were monitored in the small basin over the course of 2.5 years. Most events can be divided to multiple inter-event hydrographs, enabling, for example, to asses runoff/rainfall ratio's for different parts of the events, which at times are higher than 30%, and also specific rain thresholds as low as 0.4 mm/min for runoff initiation were identified. A runoff-sediment yield connection was also established for the small basin.

An additional study focuses on biocrust resistance to runoff. This is evaluated through a series of unique in-situ runoff experiments, which are done to characterize the role of biocrusts in gully erosion and retreat due to runoff. A unique apparatus based on the Marionet tube concept was used in a series of in-situ experiments on 13 gully head-cuts. Sequentially larger water discharges were applied to rill heads, thereby characterizing the eroding mechanism of the surface biocrust, its erodibility, and its resistance to shear stress. Parameters such as head-cut height, width, surface water velocity, plunge-pool depth, and water cross-section were monitored in each experiment.

Preliminary results show that the correlation between head-cut retreat and runoff discharge is non linear, nor is it simple. On-site and video observations as well as sample analyses reveal the occurrence of three processes: 1) As long as the biocrust is intact erosion does not occur and rill heads remain stable; 2) head-cut erosion often initiates downstream of the head, in a location where the biocrust appears to be less developed; and 3) biocrust spatial distribution patterns appear to affect the erosional processes, as does the presence of roots. It seems that water infiltration during low discharges occurs between biocrust gaps, thereby destabilizing the soil beneath, and enabling rill retreat.

These two research avenues emphasize the importance of utilizing a hydrological geomorphic-biogenic approach. A similar mechanism induces the collapse of banks during low intensity rain events with no runoff. understanding the role of biocrusts on erosional processes in arid environments, is crucial for proper landscape modeling and long term management. Some crusts remained stable, also during the highest applied water discharges.

The results are used to assess the fluvial erosional rates in the Yamin Plain and characterizing the role of biocrusts in the local hydrological regime. The acquired data will be used to construct a long-term landscape model of the area.

Challenges and solutions for a Type-A radioactive waste package based on a case study

Brandys I., Shai I., Naftolovich Y.

Introduction: Radioactive isotopes are being used in industrial processes (e.g. tank level gauges, smoke detectors) as well as in medical procedures (e.g. brachytherapy). International regulations require their proper storage and or burial thus necessitating safe and secure transport to the disposal site.

Some of the solutions are based on transporting the radioactive waste in a relative large and heavy metal container, which is not suitable to be carried by a single person. Proper design of a radioactive package, of Type-A or Type-B, can increase both the transportation simplicity as well as its safety compared to existing solutions.

As an example, a radioactive package for transporting brachytherapy 137Cs radioactive waste, in form of metal needles, is displayed. The package must comply IAEA regulations [1], considering allowed radiation levels and environmental requirements.

Case study: A durable industrial package of 420x330x174 mm external dimensions was examined. The package includes an internal shaped absorber that tightly fits gamma shielding for the 137Cs needles in order to provide the allowed external radiation levels. Three gamma shielding materials were examined: lead, tungsten and brass. The required thickness of each material was calculated for a maximum field of 2 mSv at a distance of 1 meter from the package. The dimensions of the selected package and the gamma shielding design, considering one person carriage, define the total number of needles that can be transported in each package, thus its total weight

Results; Five 137Cs needles can be transported in the designed Type-A package (Figure 1), with brass (density, p=8500 kg/m^3) as the radiation shielding material, which was chosen from manufacturing simplicity and material availability.

Figure 1. The designed type-A radioactive package

The total weight of the designed package is 10.6 kg. Along with its external dimensions, it can be carried by one person. Eight approval environmental tests, four (1-4) according to IAEA [1] requirements and four (5-8) according to Mil-STD-810 [2], were performed: (1) water spray, (2) stacking, (3) penetration, (4) raising and lifting, (5) temperature, (6) drop, (7) shock and (8) vibrations. The last three tests were more severe than required. The designed package successfully passed the environmental tests thus could be approved by the regulator as a Type-A package to transport the defined radioactive waste.

Discussion and conclusion: A simple and safe radioactive waste transport package have been designed and approved to comply international standards, thus could be approved by the regulator as a Type-A radioactive package.

Proper design of a package can provide adequate radiation protection as well as enabling safe transport of other radioactive materials. The type definition of the package depends on the transported radioactive material, its shape, form, activity and requires its performance under harsh environmental conditions according to the relevant standards.

Thermal model of geological disposal concept for radioactive sealed sources

Chricker Raz, **Levi Moshe, Klien Ben-David Ofra, Ben-Yehuda Ohad**

NRCN

Background: NRCN is used as a nuclear waste storage site. As part of its daily activities, it handles this waste, to keep public and environmental health safe both, now and in the future. One of the leading solutions for such needs is geological disposal of nuclear waste at Yamin Plain (YP), using rock properties as a long-term stable barrier against waste leakage into the environment (aquifers and/or ground surface) [1, 2].
Part of the nuclear waste is stored as sealed Cs137 sources (60 sources containing less than 2000Ci activity each), with a 30-year mid-life time. This makes it suitable for geological disposal at intermediate depth (100-150m).
These sources generate a heat capacity of up to 10W each, affecting their surrounding environment's temperature profile. Therefore, the disposal of sources in the ground must stand the thermal requirements of the geological borehole structure, to keep its structural stability over the requested time. A thermal model, which is described in this research, was developed for defining these sources' disposal configuration, considering these thermal requirements at YP.

Method: Development of a computational model, which predicts the thermal feasibility of a disposal configuration for all sources. The model is based on geological data, properties of the backfill materials, and thermal requirements. In the first phase, a literature survey was conducted to determine the thermal conductivity of soil formations and the model's sensitivity. In the second phase, the disposal borehole configuration, including the backfill materials, was incorporated into the model. In the final phase, a two-dimensional model was developed and validated for calculating the disposal configuration, while the sources were placed into one to three disposal containers (canisters).

Results: According to the results of the thermal modelling, which is based on literature data, it was found that:

1. Setting all sources in a single canister exceeds the thermal requirements.
2. Setting the sources in two canisters is marginal in terms of meeting the thermal requirements.
3. Setting the sources in three canisters with equal spacing, fully satisfies all thermal requirements, with a significant safety margin (Figure 1).

Figure 1: thermal modeling results of sources in three canisters with equal spacing inside a borehole
Discussion and Conclusion
To determine the thermal profile for geological disposal at an intermediate depth for 60 Cs137 sealed sources, a computational model was developed, based on thermal conductivity data from the literature. According to the model results, full compliance with all thermal requirements is achieved, with a significant safety margin, when the sources are contained in three canisters.
To support the calculations and the mentioned thermal profile, experimental activities are being conducted to characterize the thermal conductivity of each material in the geological borehole structure (soil, concrete). Additionally, there is ongoing development work for the sealed sources canisters.

Bibliography

[1] R. Calvo, Characterization of potential underground storage sites for radioactive waste in southern Israel - 2014 progress report, TR-GSI/05/2015, Jerusalem, February 2015.
[2] R. Calvo, O. Klein-BenDavid, Deep borehole disposal of spent fuel in Israel: Geologic feasibility status report, Report GSI/05/2018; NRCN-ND1801; SNL-784344; LA-UR-18-23564, 2018.

Borehole Disposal of Radioactive Waste in Israel - Characterization program and borehole

Ofra Klein-Ben David, Peer Gilboa, Noa Balaban and Ran Calvo

The Israel Atomic Energy Commission is assessing intermediate depth disposal of radioactive waste at the Yamin Plain (YP), located in the northeastern Negev desert region, Israel. The YP holds the Israeli national radioactive waste disposal site. Specifically, the suitability of the Ghareb Fm., of the Mount Scopus Group, residing within the vadose zone in the western YP, is being evaluated.

A comprehensive site characterization program has been underway since 2017. The program includes an in-depth literature review of the geophysics, geology, hydrology and geochemistry of the area. Rock samples from previously drilled boreholes, as well as from quarries in the area have been studied for their geomechanically, hydrological and geochemical properties.

When these preliminary studies have proven satisfactory, two seismic lines, parallel and perpendicular to the syncline axis, were run in the western YP. The seismic survey aim was to understand the detailed subsurface structure of the target zone and to assist in locating the most representative location for a characterization borehole (BH). Based on the background data together with the results of seismic survey a characterization borehole was located and drilled at the intersection of the two seismic lines. Four geological formations (Hazeva, Ghareb, Mishash and Menuha) were drilled, to a total depth of 321.5m. The Hazeva fm. was drilled using a drill bit, and rock cuttings were collected, whereas the Mount Scopus Group section (Ghareb, Mishash and Menuha fm.) was cored. One third of the cores were dipped in wax immediately after sampling, wrapped in plastic and aluminum foils and cemented in PVC tubs, in order to prevent drying, preserve to porewater fluid and keep structural integrity.

After drilling in-site analysis were preformed including the following logs: Gamma ray, Electric resistivity, Density and Caliper. Additionally, Optical televiewer (BHTV) imaging was conducted. Hydrological, single and double packer Lugeon tests were conducted as four depths in the borehole.

Core samples from the borehole were allocated to a wide range of ex-situ analysis methods mncluding, geomechanical and petrophysical characterization; mineralogical, geochemical and sorption behaviors of the rocks; porewater extraction and compositions; fracture filling dating; heat and irradiation effects on the rock and in-depth study on the organic component of the rocks.

The full program was coordinated and discussed with the regulator in order to provide the data needed for the performance assessment of this disposal area. The overall accumulated data will assist in the determination of feasibility of the Ghareb fm. to serve for borehole disposal of radioactive waste at the YP.

Geopolymers as immobilization matrices for Cs-bearing zeolites

Y. Lior-Shain*, E. Grinberg, Y. Gelbstein, M. Arbel-Haddad*

Radioactive waste streams often contain cesium radioisotopes, which may harm the environment due to their high specific activity, long half-lives and high solubility in aqueous media. In order to prevent release of cesium to the environment, it must be immobilized and encapsulated within materials that will remain stable for the long-time spans, required for radioactive decay, before being disposed in a waste repository. This study examines the ability to immobilize cesium-bearing zeolites in geopolymeric systems.

Zeolites are microporous crystalline aluminosilicates that exhibit high performance in cesium ions sorption and are used for the removal of cesium ions from the environment. Subsequent to sorption, encapsulation of the Cs-bearing zeolites becomes imperative. Geopolymers, amorphous materials with a chemical nature akin to that of zeolites, emerge as attractive candidates for this task due to their ion-binding properties and superior chemical resistance.

This work presents the structural transformations taking place following immobilization of cesium-bearing zeolites in geopolymeric-zeolite systems with varying formulation parameters (zeolite type, fraction of zeolite in the formulation, SiO2:Al2O3 molar ratio) and curing conditions (time, temperature).

The experimental methodology included phase analysis using X-ray diffraction (XRD) and microstructure characterization using electron microscopy (SEM). The cesium ion immobilization properties of the geopolymer-zeolite products were studied by standard leaching tests.

All tested samples exhibited evidence of Cs leaching from the Cs-bearing zeolites into the aluminosilicate gel during the geopolymerization process. Unlike cementitious systems, geopolymers effectively encapsulate the Cs ions leached from the originally introduced Cs-bearing zeolites within new zeolites and/or in the dense amorphous geopolymer matrix, preventing their release into the environment. Thus, geopolymerzeolite composite formulations hold promise for effective encapsulation of radioactive Cs-adsorbed zeolites.

Session 9 - Nuclear Reactors 2

Moderator: Izhar Zohar

Importance-guided evolutionary optimization for nuclear reactor core fuel management

Hadi Abuzlf & Erez Gilad

The Unit of Nuclear Engineering, Ben-Gurion University of the Negev, Israel
The Klien Institute for Nuclear Science & Engineering, Ben-Gurion University of the Negev, Israel

This study presents a novel hybrid optimization approach integrating adjoint-based neutron importance calculations with genetic algorithms (GAs) for optimizing nuclear reactor core loading patterns (LPs). The proposed method embeds deterministic adjoint-based mutation within a stochastic evolutionary framework to improve fuel assembly (FA) placement. The approach systematically reorganizes FAs to maximize the multiplication factor or minimize the power peaking factor (PPF) using the adjoint neutron flux. Benchmarking against traditional random mutation demonstrates that the hybrid method accelerates convergence and enhances optimization efficiency. However, the method offers limited performance gains for highly structured optimal configurations, such as checkerboard-like LPs. The results illustrate the potential of adjoint-based heuristics in guiding evolutionary search strategies enhancing reactor fuel management optimization.

Introduction: Optimizing in-core fuel management is a crucial challenge in nuclear reactor operation, requiring an optimal arrangement of fuel assemblies to achieve objectives such as prolonged cycle length, power flattening, and increased energy output while maintaining safety constraints. Traditional methods for LP optimization involve heuristic techniques and evolutionary algorithms like GAs. However, the vast combinatorial search space of reactor configurations necessitates innovative approaches that improve convergence efficiency. This study introduces an adjoint-based GA approach incorporating neutron importance information into the mutation operator, enhancing the stochastic search process by guiding mutations with deterministic physics-based insights.

2. Methodology:

2.1 The NuScale SMR core model

The NuScale small modular reactor (SMR) was selected as the test case for evaluating the optimization methodology. The core consists of 37 FAs in a 17×17 pressurized water reactor (PWR) lattice configuration with control rod assemblies. The homogenized multigroup neutron cross-sections for each FA were generated using the Serpent Monte Carlo neutron transport code and subsequently used in the multigroup nodal diffusion solver DYN3D for core calculations.

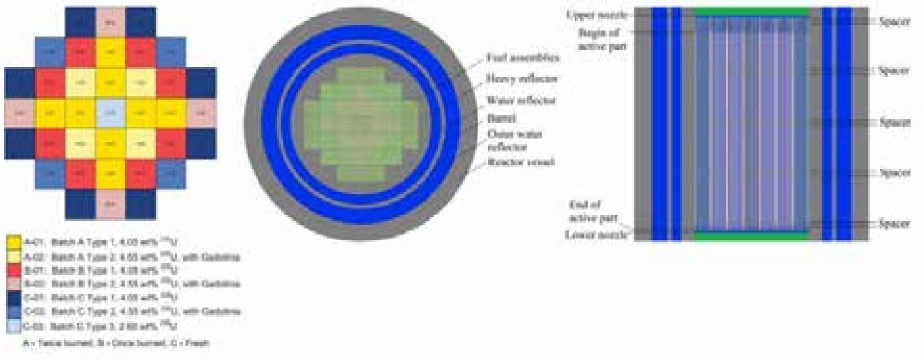

Figure 1 Layout of the NuScale SMR core design.

2.2 Hybrid adjoint-based genetic algorithm

The GA framework follows a standard evolutionary process, including initialization, selection, crossover, mutation, and elitism. The primary innovation is the integration of adjoint-based mutation, which selects FA swaps based on neutron importance derived from adjoint flux calculations. This deterministic mutation operator systematically exchanges FAs to improve reactor parameters such as keff and PPF. The LP is encoded as a vector where each gene represents an FA type and its core position. Linear ranking selection ensures balanced diversity, while geometric crossover swaps rectangular FA segments. The hybrid approach combines traditional random mutation with adjoint-guided swaps based on neutron importance rankings. The optimization runs until convergence or a predefined number of generations is reached.

3. Results

3.1 Optimization for keff maximization

Comparative analysis of standard GA and adjoint-based mutation was performed under void and reflective boundary conditions. The results indicate that adjoint-based swaps accelerate convergence and consistently achieve higher keff values than purely random mutation. The method effectively clusters high-enrichment FAs in high-importance regions, minimizing neutron leakage and enhancing reactivity.

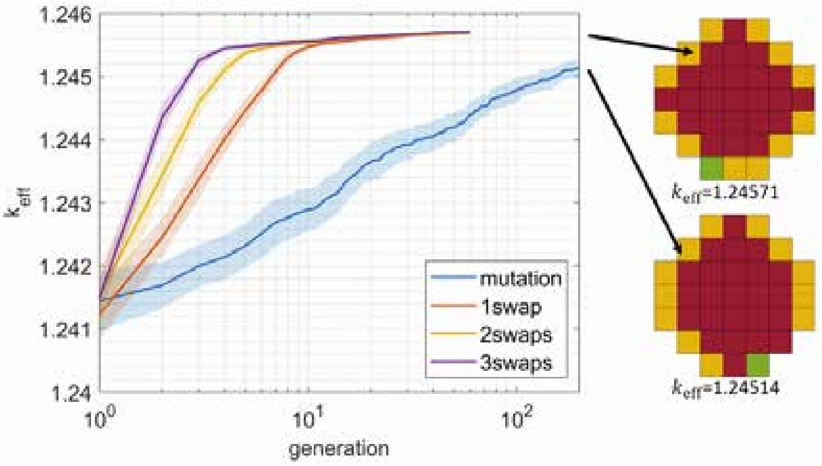

Figure 2 The evolution of the multiplication factor, k_{eff}, with void boundary conditions during the optimization for the standard random mutation and three variants of the adjoint-based mutation, with 1, 2, and 3 swaps per chromosome per generation. The results of 30 different realizations for each scenario are shown, with 20 chromosomes in each realization. The shaded regions represent the associated standard deviation of the k_{eff} value.

3.2 Optimization for PPF minimization

When optimizing for a uniform power distribution, adjoint-based swaps outperformed random mutation under void boundary conditions. However, under reflective boundary conditions, the standard GA and adjoint-based GA exhibited similar performance, likely due to the structured nature of the optimal checkerboard-like pattern.

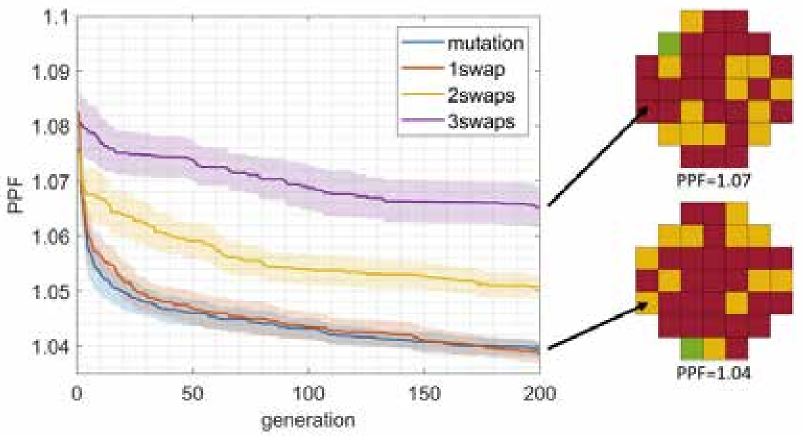

Figure 3 The evolution of the PPF with reflective boundary conditions during the optimization for standard random mutation and the adjoint-based swaps with 1, 2, and 3 swaps per chromosome per generation. Each curve is the average of 30 different realizations.

4. Conclusions

The proposed hybrid adjoint-guided GA enhances LP optimization by integrating deterministic neutron importance insights with stochastic evolutionary search. The method accelerates convergence and improves optimization outcomes in most scenarios. However, for highly constrained structured solutions, purely random approaches remain competitive. Future research will explore adaptive hybridization strategies and integration with thermalhydraulic constraints to refine nuclear reactor core optimization methodologies further.

Advancements in cross-section homogenization for rotating control drums in microreactors

Hadi Abuzlf & Erez Gilad

The Unit of Nuclear Engineering, Ben-Gurion University of the Negev, Israel
The Klien Institute for Nuclear Science & Engineering, Ben-Gurion University of the Negev, Israel

This study explores the cross-section homogenization of rotating control drums in microreactors, focusing on their neutron absorption characteristics and reactivity worth. The research is motivated by the increasing deployment of microreactors in remote and space applications, where compact and efficient reactivity control is paramount. We employ Monte Carlo simulations (Serpent) to evaluate neutron interactions and homogenize the control drum configurations for use in multigroup nodal diffusion solvers (DYN3D) utilizing the HOLOS Gen-2+ microreactor design as a test case. The results highlight the complex dependency of neutron absorption on the rotational states of adjacent drums, revealing that traditional homogenization techniques struggle with these non-linearities. Nevertheless, we demonstrate that accurate reactivity predictions can still be achieved using homogenized cross-sections in diffusion-based simulations, paving the way for more efficient computational modeling of microreactors.

Introduction: Microreactors, designed for remote deployment and autonomous operation, require novel reactivity control mechanisms that balance compactness, reliability, and safety. Due to spatial constraints, traditional control mechanisms, such as control rods, are not always feasible in microreactor architectures. Rotating control drums offer a viable alternative, allowing reactivity adjustments by changing the orientation of neutron-absorbing materials embedded in the reflector. However, the interactions between multiple control drums introduce complexities in neutron flux distribution and reactivity worth calculations. This study aims to address these challenges by developing a homogenization methodology that enables efficient modeling of control drum behavior in diffusion-based reactor physics codes.

Figure 1 An illustration of the Holos-Quad microreactor.

2. Methodology

2.1 Reactor core model

The HOLOS Gen-2+ microreactor, a high-temperature gas-cooled reactor (HTGR), is the reference model. It features 20 azimuthally arranged control drums, each comprising a 120° sector of boron carbide (B4C) within a beryllium oxide (BeO) reflector. The core's compact design necessitates precise modeling of neutron interactions for accurate control drum reactivity assessments.

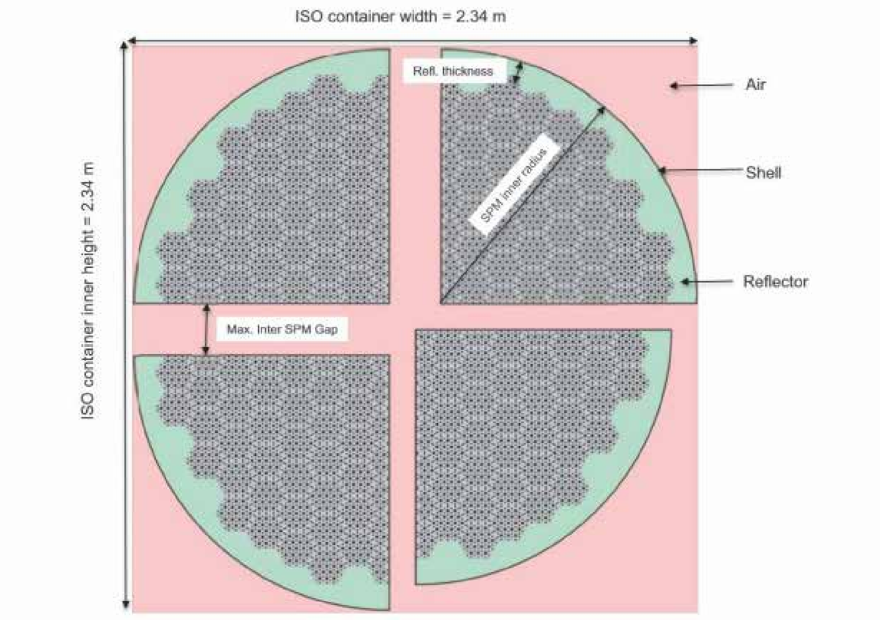

Figure 2 Radial cross-section of the core layout with 3 out of 4 SPMs withdrawn for shutdown.

2.2 Computational Tools:

The Serpent Monte Carlo code was used to perform high-fidelity neutron transport calculations, capturing detailed neutron flux distributions and interaction probabilities. The DYN3D multigroup nodal diffusion solver employed the homogenized cross-sections derived from Serpent, enabling rapid analysis of reactivity changes across different control drum configurations.

3. Results

3.1 Validation of homogenized cross-sections

The homogenized cross-sections are benchmarked against direct Monte Carlo simulations to assess their accuracy. Discrepancies in reactivity worth calculations range from 10 to 300 pcm, depending on the relative rotational states of adjacent control drums.

3.2 Effect of control drum rotation on reactivity

The study reveals a non-linear dependence of neutron absorption on control drum positioning. Specifically, adjacent drums compete for neutron flux, leading to significant variations in reactivity worth based on their combined rotational states. The most pronounced absorption effects occur when neighboring drums align their B4C sectors toward the core, whereas configurations with staggered rotations exhibit reduced neutron absorption.

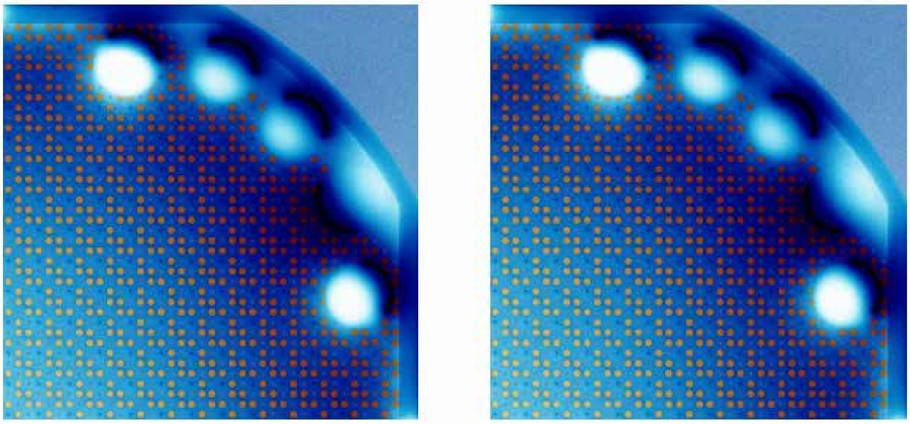

Figure 3 A visualization of the neutron flux and the fission density for different control drums rotation angles.

3.3 Comparison of Serpent and DYN3D Predictions

Diffusion-based calculations using homogenized cross-sections strongly agree with Monte Carlo results, particularly in configurations with minimal neutron flux gradients. However, deviations increase for highly asymmetric drum configurations, indicating the need for further refinement in the homogenization approach.

4. Conclusions

This study demonstrates the feasibility of cross-section homogenization for rotating control drums in microreactors. While traditional homogenization methods face challenges due to the non-linearity of neutron absorption, the proposed approach enables reasonable accuracy in diffusion-based calculations. Future work will focus on refining the homogenization process to account for localized flux perturbations and extending the methodology to transient reactor simulations. The findings improve computational efficiency in microreactor design and optimization, ultimately supporting their deployment in remote and space-based applications.

Energy Deposition Post-Shutdown in Various Components of the OPAL Reactor Core

Nir Kastin, Aviv barnea, Guy Stein

An analysis for the energy deposition post-shutdown, caused by radiation from fuel decay products and from other sources of energy, is presented for the major heated components of the OPAL reactor core, that is its guide boxes, its absorber plates and its fuel rods. The various contributors for the energy deposition in each component are identified and quantified during steady-state operation, and each of these contributors is associated with a relevant "decay heat" curve, allowing the derivation of the energy deposition in the various components post-shutdown.

It is shown that due to the much larger contribution of delayed photons to the energy deposition in non-fuel components compared to the fuel, the heat flux decay curves of the non-fuel components decay much more slowly than the heat flux decay curve of the fuel. As a result, the ratio between the heat flux decay curve of the guide boxes and its counterpart of the absorber plates is found to remain relatively similar to its value during steady-state operation, whereas the heat flux decay curve of the guide boxes turn out to be comparable within rather short and accident relevant time scales to the hottest fuel plate's heat flux decay curve. It is concluded that the design of coolant channels between fuel to non-fuel components must be carefully conducted, relying on safety related calculations for both steady-state operation conditions, and especially for the analysis of accidents of deteriorated heat transfer post-shutdown, such LOFA and LOCA scenarios. All computational estimations are obtained using OpenMC. Specifically, they are obtained using a newly developed capability that has been implemented over the course of this work for this purpose.

This capability would be suggested as contribution to the code base in the near future in order to allow widespread usage.

Temperature Measurement Using Fiber Bragg Gratings for a Nuclear Reactor Application

Schneider A. S., Kalenko S., Elimelech Y., Bokai M.

Background: Fiber Bragg Gratings (FBGs) [1] offer a promising approach for temperature measurement in nuclear reactors due to their compact size, high sensor density, and rapid response time [2]. However, measurement accuracy is significantly impacted by strain effects, necessitating a reliable anchoring method.

Methods: A novel one-sided anchoring method was developed, where fibers were fixed only at the top, minimizing strain-induced errors. Comparative experiments were performed using both one-sided anchoring and two-sided anchoring, in which the fibers were additionally secured at the bottom. The setup was vertically positioned in a water tank simulating a reactor pool with a hot layer to measure temperature gradients. The FBGs calibration was performed using PT100 sensors.

Results: Successive calibration experiments demonstrated that the one-sided anchoring method significantly improved temperature measurement reproducibility. Maximum temperature deviations between consecutive calibrations were reduced from ~1°C in the two-sided configuration to <0.5°C in the one-sided setup. As a proof of concept, static hot-layer experiments were carried out which further validated this method, showing reduced systematic discrepancies between temperature readings on different fibers.

Conclusions: The new anchoring method effectively minimizes strain effects and enhances measurement accuracy. Ongoing work aims to refine the technique by further reducing error sources such as water absorption, and temperature stabilization, ultimately improving the reliability of FBGs for temperature measurement in nuclear reactor applications.

Mathematical Foundation of the IFP method

Ben Hatzofe

Inner products of the fundamental mode of the ajoint k problem are of great importance in nuclear reactor's analysis, due to their role in perturbation theory. Thus, computing inner products of the fundamental mode of the ajoint K problem is a classic problem in nuclear reactor's analysis. Historical approaches included interpreting the adjoint problem as the transport of pseudoparticles - the "backwards" problem.

It was shown, that the backwards problem could be solved by MultiGroup methods or by continuous-energy Monte Carlo, in a process that involves advanced processing of available nuclear data. Each of these methods carries its downsides, thus an alternative approach was desired. The Iterated Fission Probability method is a different approach, that admits the extraction of adjoint fundamental mode inner products from a forward transport calculation. This method is also applicable to continuous-energy Monte Carlo and is implemented in many state of the art Monte Carlo codes. The basis of this method involves the definition of the IFP as the asymptotic amount of neutrons that will emerge from a point source. A direct consequence of this definition is that it may be estimated as the product of the multiplication factor of the point source's successive generations. A subtler consequence of the definition, is that the IFP satisfies a PDE adjoint to that of the K eigenvalue problem. The connection of these two brings forth the IFP method. In this work, we discover a different, more direct approach to derive that same relation. This approach, sheds light on several important transport concepts, like the fission source and its adjoint, and the generation operator.

This approach offers an additional insight - the relation between the notion of "passive cycles" and "number of generations". The lecture will be of pedagogic nature, and will emphasize advanced transport concepts and the application of the IFP.

Session 10 - Radiation Detection & Measurements 2

Moderator: Adi Avraham

Improving performance of PIPS detectors using advanced characterization techniques

Ohad Westreich*, Moran Bin Nun*, Shoval Zoran, Ilan Goldward, Sabag Oriya, Evenstein Eliran, Rubinstein David, Cohen-Elias Doron and Gil Atar

Introduction: Passivated implanted planar silicon (PIPS) detectors and silicon PIN diodes are widely used in radiation detection due to their excellent energy resolution, high efficiency, and stability. These detectors are essential in applications such as medical imaging, environmental monitoring, and scientific research. PIPS detectors are particularly valued for their reduced leakage currents, precise junction formation, and durable entrance windows, which enhance their overall performance and sensitivity. Leakage current, especially when detecting weak signals or achieving high resolution, is a critical factor affecting the performance of these devices.

Leakage current in semiconductor detectors is primarily composed of surface current and bulk current. Surface current arises from imperfections at the material's surface, such as oxide layers or contaminants, creating paths for current to flow across the surface of the detector. Bulk current, on the other hand, originates from defects or impurities within the bulk semiconductor material, like deep-level traps or lattice dislocations, allowing charge carriers to flow even without external bias. Separating surface and bulk leakage currents is crucial for optimizing device performance. Isolating these two components allows for targeted adjustments in manufacturing processes to address each source effectively. Surface leakage can be minimized by improving passivation processes or using better insulating materials, while bulk current can be reduced by enhancing material purity or adjusting doping profiles.

Various methods have been developed to distinguish between surface and bulk leakage currents. Temperature-dependent measurements are commonly used, as surface currents are more sensitive to temperature variations than bulk currents. Additionally, techniques like deeplevel transient spectroscopy (DLTS) and capacitance-voltage measurements help analyze bulk defects and surface-related issues separately, providing insights into improving fabrication processes.

In this study, we introduce the three-point probe (3PP) technique, an advanced method for analyzing leakage currents in silicon detectors. This method involves designing concentric ring(s) around the device with three probes: two at the p+ contact and one connected to the ground at the n+ contact. The diode is oriented vertically, and a reverse bias voltage is applied to generate the current-voltage (I-V) curve. The outer ring measures the surface current, while the inner probe captures the bulk current, effectively distinguishing between the two sources of leakage. Figure 1 illustrates the design of the detector, in top view and cross section.

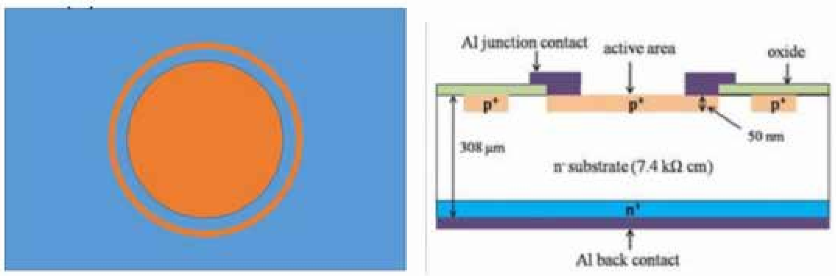

Figure1 - a) schematic 3pp with ring. (top view). b) Typical 2d-structure (Cross section)

To validate the reliability of the 3PP technique, we compare it with the peripheral-over-area method, where different PIN diodes with varying diameters are tested to assess leakage current. By comparing results from both methods, we verify the accuracy of the 3PP approach in separating surface and bulk currents, ensuring its robustness for leakage current analysis.

Understanding the sources of leakage currents is vital for optimizing detector design, particularly in high-resolution applications. By employing the 3PP technique, we offer valuable insights into improving PIPS and PIN diode detectors. Reducing leakage current enhances the performance of these devices, crucial for achieving reliable and accurate radiation detection.

Methods: Design and fabrication: A circular PIPS detector with varying diameters ranging from 10 mm to 24 mm is designed for this study, with a particular focus on employing the three-point probe (3PP) method to distinguish between surface and bulk leakage currents. The detector is fabricated from a floatzone (FZ) n-type silicon wafer with a resistivity of approximately 10,000 □·cm, a thickness of 450 μm, and a diameter of 4 inches. The PIN diode consists of a highly doped p+ silicon layer at the front, a n0 region, and a highly doped n+ layer (serving as a getter) at the bottom. A 60 nm-thick thermal $SiO2$ passivation layer is applied to the periphery of the detector to suppress surface leakage currents. For the 3PP technique, an outer concentric ring is designed around the detector to enable the precise separation and measurement of surface and bulk leakage currents. Metal contacts, consisting of a 200 nm nickel (Ni) film, are deposited on both the front side (ptype) of the detector, including the concentric ring and the p-type region, as well as on the backside (n-type) layer. These contacts form the electrical connections, ensuring good conductivity for the measurements. The contacts are connected to the extended anode and cathode, respectively. To further suppress the leakage current, a rapid thermal processing (RTP) step is employed, under a temperature of 450°C for 3 minutes with 23 Sccm N2H2 pressure. This process enhances the quality of the passivation layer, reducing surface states and improving surface current characteristics. Figure 2a shows a GDS-file of the design of the detector, featuring the concentric ring and detectors of varying sizes; Figure 2b shows one of the masks used for the lithography process. Figure 2c show a microscope image of the fabricated devices with zoom-in on p-type ring and disc.

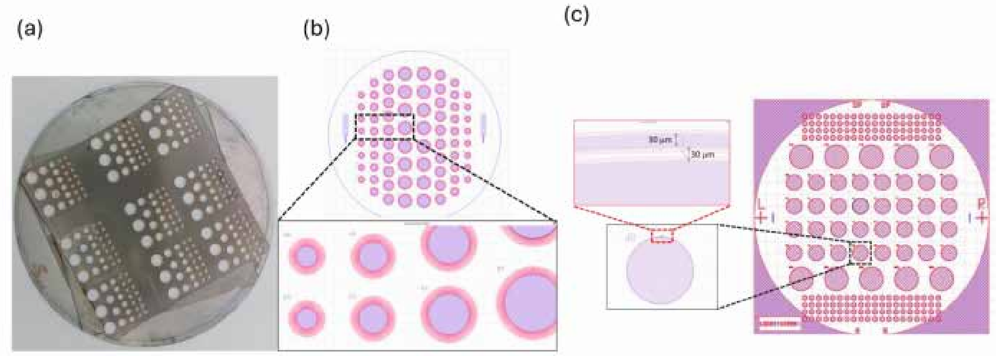

Figure 2 – a) mask, (lithography machine?) b) GDS with zoom in. c) fabricated with zoom in

IV measurements: A novel 3-point probe (3PP) current-voltage (IV) measurement technique is implemented as follows: Two probes are connected to the top n-contact–one to the detector and one to the outer ring - both grounded at 0V. A varying voltage is then applied to the third p-type contact located at the bottom of the device.

This applied bias enables the separation of current components:

- The outer ring current (Iring) captures the surface leakage current.
- The inner probe current (Idet), positioned on the inner disk, measures the bulk current.
- The bottom contact collects the total current.

We also implemented automated scanning using a Python-enabled motorized stage to measure multiple devices efficiently. This setup allows for high-throughput measurements across the wafer, enabling the characterization of many devices in a single run. A full scan of approximately 70 devices is completed in about 30 minutes.

Results and discussion: The configuration of concentric metal rings and inner probes allows for a clear separation and measurement of surface and bulk leakage currents, making it a powerful tool for analyzing and optimizing leakage current behavior in silicon detectors. An example of 3pp measurements of typical detector, and the current separation it enables is illustrated in Figure 3. Here we demonstrate the significant difference this method enables, distinguishing currents by more than two orders of magnitude. The method reveals that before the RTP process, the limiting mechanism at low voltage is bulk leakage, while at high voltage, it is dominated by surface leakage. After the RTP process, improvements are observed in the bulk current, with a significant reduction in surface leakage. Our demonstrated method offers several advantages over traditional approaches, including:

- Fast and reliable separation of leakage mechanisms.
- Precise identification of leakage sources within a single device, eliminating the need for statistical analysis.
- Real-time tracking of changes over time, such as charging effects.

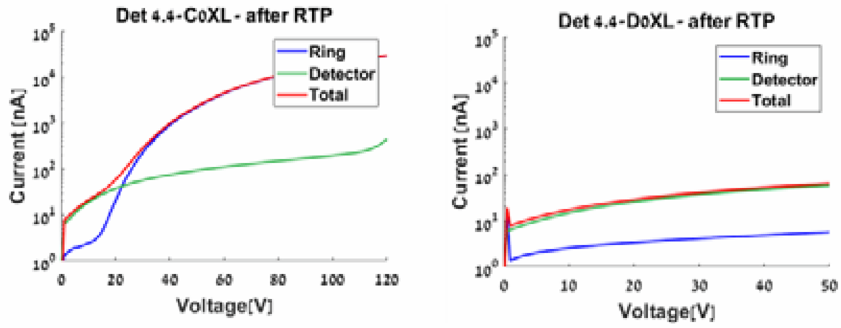

Figure 3 – IV measurements of PIPS detector using 3pp method, separating ring and detector currents, before (a) and after (b) RTP process.

Summary: In this research, we introduced a three-point probe (3PP) technique for separating surface and bulk leakage currents in silicon PIPS detectors, providing a clearer understanding of leakage behavior.

We demonstrated how this method enables the identification of leakage sources and facilitates their improvement, offering a reliable approach for optimizing detector performance in highresolution radiation detection applications.

Compared to traditional methods, the 3PP technique allows for fast and accurate separation of leakage mechanisms, precise identification of leakage sources within a single device without relying on statistical analysis, and real-time tracking of changes over time.

After processing, significant reductions in surface leakage and improvements in bulk current are observed, leading to enhanced detector performanc.

Keywords: Radiation Detection, Si PIN diode, PIPS, Leakage current.

Directional Detection of Multiple Gamma Sources Using Mutual Shielding of Scintillators

N. Ben David, M. Ghelman, E. Vax, A. Osovizky, and I. Kaminer

Background: Directional detection of gamma sources is critical for applications such as decontamination, nuclear incident response, radiological event management, and preventive security measures. In the low-energy range (<200 keV, e.g., 241Am), Compton directional detectors use passive collimation methods, such as coded apertures, which suffer from a narrow field of view, low sensitivity, and high weight [1,2,3]. Some detectors utilizing mutual shielding have been proposed for estimating the location of a single gamma source [4,5], but multi-source detection remains a challenge.

Methods: We propose a 4π directional detector for multiple gamma sources, leveraging mutual shielding of scintillators. The detector consists of 64 CsI(Tl) cubic scintillators, each 12.4 mm per side, coupled to Silicon Photomultipliers (SiPMs). The sensors are arranged in a spatial configuration optimized for both directional accuracy and sensitivity (Fig. 1). Signals from the sensors are processed by a commercial readout system.

The system's enhanced precision and efficiency could significantly improve radiation detection in dynamic and challenging environments. This work presents a comprehensive overview of the detector's design, operational principles, and analytical methodologies.

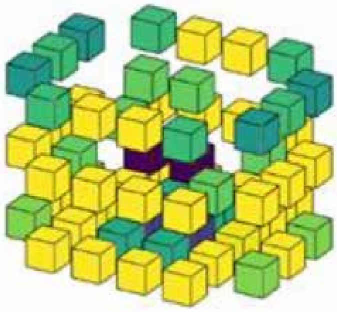

Fig. 1: Illustration of the scintillator arrangement for 4π directional detection

Results: Using an Expectation-Maximization (EM) algorithm, we estimate the flux intensity from all directions simultaneously. Initial measurements validate the system's capability to accurately determine gamma sources directions across a full 4π steradian sphere. Ongoing experiments focus on compliance with the IEEE N42.62-2023 Standard for Passive Imaging Radiation Devices (PIRDs) for radioactive and nuclear material localization.

MAXIMA-I a Coincidence System for Nuclear Decay Investigations

Sagi Nissim[1,2], **Ofer Aviv**[1], **Michal Brandis**[1], **Lior Arazi**[2], **Erez Gilad**[2]

1 Soreq Nuclear Research Centre,
2 Ben- Gurion University of the Negev

MAXIMA-I is a ground-level coincidence system developed at the Soreq Nuclear Research Center; it is designed for low-level activity measurements and nuclear decay investigations. The system combines a high-purity germanium (HPGe) detector and a liquid scintillator detector, enabling simultaneous detection of alpha, beta, and gamma emissions while providing high energy-resolution and near 100% efficiency for detecting alpha and beta detection. Data is recorded in list mode. In addition, The system facilitates a substantial reduction in background counts through the selective identification and exclusion of specific events. This capability enables the attainment of background levels comparable to those observed in certain underground facilities, thereby significantly enhancing the sensitivity of measurements. In addition, the system allows for detailed investigation of faint emissions originating from specific radionuclides, contributing to improved detection capabilities in various applications. Our presentation will cover the system's characterization and showcase its application in studying nuclear decays of 210Po, 99Mo, and 36Cl.

Whole body counter model validation using Monte Carlo simulations

Lior Epstein, Ofer Aviv, Henry B. Spitz, Zohar Yungrais, Dan Epstein, Hanan Datz

The whole body counter (WBC) at Soreq Nuclear Research Center is used for routine monitoring of occupationally exposed workers working with radioactive materials that may lead to internal contamination. The WBC is also used for dose assessments in unexpected exposures, as in incidents with suspected internal contamination. The WBC system consists of four sensitive HPGe detectors, located above and below the scanned individual.

In the current work, we present a calculation and validation of the detection efficiency of the whole body counter using Monte Carlo simulations. We compare the simulation results with measurements of radioactive sources embedded inside a torso phantom. These included point like sources and homogeneously distributed sources in the lungs. Three source types were selected for validating the model, representing a wide range of photon energies: 241Am (59 keV), 137Cs (662 keV) and 60Co (1172 keV and 1332 keV). The response of the whole body counter was simulated using the FLUKA Monte Carlo code. A torso phantom manufactured at Lawrence Livermore National Laboratory (LLNL) was CT scanned and the output file was loaded into FLUKA to create a computational phantom for implementation in the Monte Carlo simulation. The same phantom was used for the measurements. A point-like source was placed at one of 20 locations in the phantom lungs and the detection efficiency was measured in the WBC. The measurement was then compared with the calculated efficiency for each location and detector. Furthermore, the measurement efficiency for a uniform distribution of the selected radionuclides in the lungs was compared to the calculated one.

The calculated efficiency showed good agreement with the measured efficiency for the different source types and geometries. Thereby, benchmarking the computerized model. We will present the results and discuss future work and prospects in internal dosimetry in case of unintentional exposure.

Fast Neutron Detector using 4He

Amir Broide[1*], Yacov Finkelstein[2], Dvir Smadja[1], Yeshayahu Levin[1], Ilan Choen Zada[1], Micael Pazeiv[1], Moshe Ben Salomon[1], Benny Cohen[3], Udi Wengrowicz[1], Aharon Ocherashvili[4]

1 *Electronics and control laboratories Nuclear Research Center Negev, Israel*
2 *Chemistry department, Nuclear Research Center Negev, Israel*
3 *R&D Department of Nuclear Detector, Monitoring & Counting Systems, Nuclear Research Center Negev, Israel*
4 *Physics department, Nuclear Research Center Negev, Israel*
* *Corresponding author*

Keyword: Proportional Detector, Neutron, quenching gas

The increasing scarcity and high cost of helium-3 (3He) have driven the exploration of alternative neutron detection technologies, with helium-4 (4He) emerging as a promising candidate. This study examines the feasibility of using 4He proportional detectors as a substitute for 3He in neutron detection applications, focusing on tailoring the optimal gas mixture of quenching gas and 4He to achieve the best efficiency.

The optimization of quenching gases in fast neutron detectors is critical for improving their performance, stability, and longevity. Various gases, including noble gases (e.g., Ar and Ne) and polyatomic gases (e.g., methane-CH_4, isobutene-C_4H_{10}, and carbon dioxide-CO_2), are suitable candidates to serve as quenching gas. For the current study, the JRC standard of 15 Atm. total pressure of 4He-CO_2 mixture, was adopted, and a systematic trial-and-error approach was applied to tailor the most effective concentration of the CO_2 quenching gas for a fast neutron detection. The effect of CO_2 on the detector parameters, such as signal amplitude, time resolution, sensitivity, and gas breakdown thresholds, was assessed. The resulting measured trade-offs between performance and operational stability, provide the ability of selecting the mixture composition that minimizes spurious discharges while maintaining high neutron detection efficiency. This approach demonstrates the value of iterative testing in optimizing gas mixtures for specialized detector applications, offering insights into the interplay of gas properties with detector physics.

Session 11 – Nuclear Physics

Moderator: Guy Ron

Structural evolution of even-even and odd-mass atomic nuclei

N. Gavrielov

Quantum phase transitions (QPTs) in atomic nuclei manifest as abrupt structural changes in the spectrum, arising either from shape evolution or the crossing of shell model configurations along a chain of nuclei as the nucleon number varies. Over the years, extensive theoretical and experimental investigations, particularly those conducted at rare isotope beam facilities, have examined a wide array of nuclear structure phenomena, including shape evolution, shape coexistence across multiple shell model configurations, and modifications in single-particle energies. In this talk, I will present my research on these structural phenomena through algebraic frameworks. I will begin by introducing the interacting boson model (IBM) for even-even nuclei, a framework that enables the exploration of diverse nuclear phenomena while providing deep insights into the symmetry structure of nuclei, all at a low computational cost. I will discuss my work on the chain of zirconium isotopes ($Z = 40$) with neutron numbers $N = 52$–70, focusing on the emergence of intertwined quantum phase transitions (IQPTs). These transitions arise when a QPT involving configuration crossing coincides with another QPT associated with shape evolution within each configuration as the nucleon number varies. Additionally, I will introduce a novel approach developed during my time at Yale for investigating odd-mass nuclei. Using this method of interacting boson-fermion model with configuration mixing (IBFM-CM), I will present my work conducted at GANIL on the odd-mass zirconium isotopes with neutron numbers $N = 53$–63. This study reveals three key effects within this isotopic chain: shape evolution, configuration crossing, and changes in single-quasiparticle orbitals. I will then highlight the case of 99Zr, which lies at the critical point of both shape evolution and configuration crossing QPTs, and propose a resolution to a recent debate concerning the nature of its single-particle orbitals. To conclude, this work provides new insights into the interplay between shape evolution, configuration mixing, and single-particle dynamics, offering a broader perspective on quantum phase transitions in nuclear structure.

Precision Measurement of the charge radius of Be 9 Through Muonic X-Ray Spectroscopy

O. Eizenberg, S. Rathi, B. Ohayon for the Quartet Collaboration

Background: Precision muonic x-ray measurements in light muonic atoms, such as, $\mu\ Be$ 9 could now be performed with sufficient precision to extract an improved charge radius. This advancement is due to the recent progress in quantum-technology-based photon-energy sensors (calorimeters). Precise knowledge of nuclear properties such as nuclear radii are keysfor better understanding of nuclear forces, Quantum electrodynamics (QED) in strong-fields and searches for new physics. Our new collaboration, QUARTET, aims at improving the Be 9 charge radius by an order of magnitude by employing new, high-efficiency, x-ray spectroscopy magnetic calorimeters. In a proof-of-principle experiment, these detectors were employed to measure the low-lying states in $\mu\ Be$ 9 . Precision knowledge of the low-lying states is essential for determining the nuclear charge radius, as these states are significantly influenced by the nucleus .

Methods: After a successful proof-of-concept experiment in October 2023, in October 2024, the collaboration designed and conducted an experiment measuring muonic X-rays of Be 9 . The Be 9 target was placed inside a target chamber in front of a muon beam in the pi-E1 beamline at PSI, Villigen. An MMC (metallic magnetic calorimeter) was setup and placed in front of the target chamber. For Calibration, an x-ray tube was set up in front of the MMC together with a Ba-La target, providing wellcharacterized K_alpha x-ray lines from Ba and La that are close to the expected muonic x-rays from Be 9.

Discussion and conclusions: The experiment was successfully conducted, and preliminary analysis demonstrated its capability to achieve state-of-the-art high-resolution measurements with high statistics of good calibration. Further, data analysis is required to fully interpret the results.

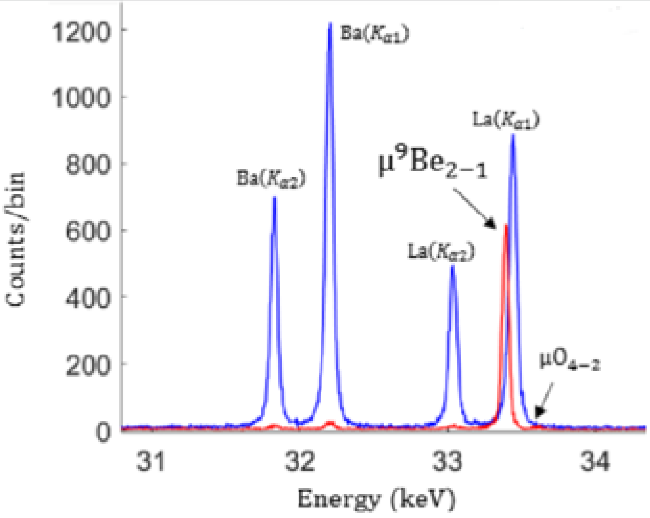

Figure 1: Zoomed-in preliminary results from the 2024 beamtime. The red color indicates events registered in a narrow time window after a muon triggered the scintillator. Blue indicates events outside this time window.

The NEXT search for neutrinoless double beta decay: status and prospects

Dr. Lior Arazi, Ben-Gurion University

The search for neutrinoless double beta (ββ0ν) decay is one of the central efforts in particle physics today. A detection of this ultra-rare phenomenon will prove that the neutrino is its own antiparticle and demonstrate, for the first time, the non-conservation of the total lepton number. It will further provide a clue for the origin and smallness of the neutrino mass, as well for the dominance of matter over antimatter in the Universe. Several collaborations in Europe and the US are preparing to search for neutrinoless double beta decays with tonne-scale detectors in the next decade with an overall budget of about USD 1B. In this talk I will focus on the NEXT program, of which BGU is a leading member, which searches for ββ0ν decay in 136Xe, using successive generations of high-pressure gaseous xenon time projection chambers. Beyond superb energy resolution - a must for any successful ββ0ν experiment - NEXT has the unique ability to record, in fine detail, the 3D images of events occurring inside the detector. This allows discriminating between two-electron signal events and single-electron background events based on the event topology.

Lastly, the collaboration pursues an extensive R&D program to develop the capability of detecting the 136Ba daughter resulting in 136Xe double beta decays inside a running TPC using specially engineered fluorescent molecules. This effort can lead to a background-free search for ββ0ν decay on the tonne-scale, with halflife sensitivities of >1028 y. This talk will present the status of the NEXT program and outline the future steps of the experiment.

Advanced in Topological Analysis for Background Reduction in Gaseus Time Projection Chamber Event Processing

Adam Redwine, Lior Arazi

Gaseus time projection chambers like those employed by the NEXT collaboration for detection of neutrinoless double beta decay offer the potential for background rejection by topological analysis. Three-dimensional reconstructions of events closely map the location and amount of energy deposition within the detector volume. Identification of the ends of individual particle tracks allows event segregation based on the relatively high energy density region associated with the Bragg Peak as compared to the relatively low energy density region associated with the ionizing particle starting location generated by a Compton scatter event. This talk will present recent developments in improvements of this topological analysis including increases in signal efficiency and decreases in background retention, as well as improvements in particle track modeling for identification of features such as delta rays and event satellites.

Session 12 - Radiation Therapy & Alpha DaRT

Moderator: Lior Arazi

The Effect of Broad Nucleus Size Distributions in Diffusing Alpha-emitters Radiation Therapy

Y. Korotinsky, L.Arazi

Background: Diffusing Alpha-emitters Radiation Therapy ("Alpha DaRT") is a new method, presently in clinical trials, which allows treating solid tumors with alpha particles. Alpha DaRT uses interstitial sources that carry μCi-level 224Ra activity below their surface, designed to release a chain of short-lived alpha emitters that spread throughout the tumor volume primarily by diffusion. The integration of Alpha DaRT in clinical practice requires the establishment of precise tumor dosimetry to accurately determine the therapeutic dose required for tumor eradication. To date, theoretical studies have focused on macroscopic dose modeling using the timedependent solutions of the Diffusion-Leakage model. The fundamental physics and a simplified theoretical framework for treatment planning have been outlined in several recent studies.

Purpose: This study extends the theoretical framework of Alpha DaRT by incorporating microdosimetry to analyze biological responses, such as cell survival and tumor control probabilities, on a microscopic scale. It is well acknowledged that the size of the nucleus and the cell's intrinsic radio-resistance, z0, are critical factors influencing cellular responses to radiation. Typically, microdosimetric studies assume uniform nucleus sizes, overlooking continuous distributions. Here, we investigate the effects of broad and continuous nucleus size distributions on cell survival and Tumor Control Probability (TCP).

Methods: We introduce a microdosimetric model to simulate alpha particle interactions within tumor cells, employing both analytical and Monte Carlo techniques. The model considers a tumor region subject to a macroscopic alpha particle dose. Cells and nuclei are modeled as two concentric spheres of liquid water, and alpha particles are assumed to follow straight lines without straggling. Tracks are classified as ``hits" if they cross the nucleus envelope at least once. Our model estimates the specific energy, z, deposited by alpha particles in cell nuclei, and quantifies biological effects through survival and tumor control probabilities. Nucleus size variability is analyzed using artificial Gaussian distributions and an empirical broad distribution inputted into the microdosimetric model.

Results: Our findings indicate that broad Gaussian distributions of nucleus sizes cause survival curves to diverge from an exponential pattern, especially beyond in-vitro study doses of a few Gy. At higher doses relevant to tumor treatments, these deviations become significant. Wider distributions lessen the survival probability gap between radio-sensitive (z0 = 0.5 Gy) and radioresistant (z0 = 1 Gy) cells. Including an empirical nucleus size distribution in TCP calculations, focusing on minimal nucleus size threshold Rth variations from 0.5-2 μm, shows that deviation from an exponential trend at high doses remains similar to that of Gaussian PDF. As Rth increases, the survival curve reverts to an exponential form. Variations in Rth notably impact TCP curves, with D50 (the dose for TCP = 50%) rising from 12.6 Gy at Rth = 3 μm to 18.1 Gy at Rth = 2 μm, and then sharply to 44.5~Gy at Rth = 1 μm. The D50 disparity between radiosensitive and radioresistant cells narrows from 6.1 Gy at Rth = 2 μm to 3 Gy at Rth = 1 μm.

Conclusions: The remarkable TCP sensitivity to variations in Rth highlights the necessity of establishing a realistic threshold on the minimal nucleus size distribution of clonogenic cells. Very small nuclear dimensions, particularly in dividing cells, seem implausible. Most literature sets the reasonable minimum nucleus radius at 2 μm, which we also adopt, recognizing it may still represent extremely small, possibly non-clonogenic nuclei. Reducing Rth lessens survival probability disparities between radio-sensitive and radio-resistant cells. However, with Rth = 2 μm, the D50 difference remains significant (~ 6.1 Gy), making the impact of z0 noteworthy.

Measurements of the effective diffusion length of 224Ra decay products in healthy tissues in Diffusing alpha-emitters Radiation Therapy

Lior Epstein, Mirta Dumancic, Maayan Vatarescu, Ishai Luz, Arindam Roy, Elad Flaisher, Itai Jacoby, David Castel, Ofer Magen, Niv Dana, Yoav Roa, Amir Sherman, Nir Edry, Stephanie Oren, Lior Moss, Saleem Eden Bari, Kobi Aharoni, Tomer Cooks, Israel Gannot, Itzhak Kelson, and Lior Arazi

Background: In Diffusing alpha-emitters Radiation Therapy ("Alpha DaRT"), as in all radiation cancer therapies, treatment planning aims at effective dose delivery to the tumor while sparing dose from healthy tissues. Alpha DaRT uses alpha particles, emitted from the decay products of 224Ra, for the treatment of solid tumors. The 224Ra sources carry an activity of a few µCi and are placed interstitially. When 224Ra decays, it releases a chain of short-lived atoms emitting alpha particles. These atoms diffuse around the source and through their decay, they create a treated volume measuring a few mm in diameter. The size of the treated volume necessitates the use of multiple sources in a lattice form and specific treatment planning to ensure that the tumor will receive the maximum dose while sparing healthy tissues. The treatment plan - in particular the distance between the lattice points, depends on the effective diffusion length of the atoms inside the tumor and surrounding tissues.

Purpose: Several studies have measured the effective diffusion length in different tumor types and found it to be in the range of 0.2-0.6 mm. In the current work we measure the diffusion length in healthy tissues, which is an important factor for treatment planning - a shorter diffusion length would necessitate the use of more radioactive sources in the tumor periphery to obtain full coverage while longer diffusion length would imply possible higher doses to surrounding tissues.

Methods: Radioactive sources were inserted into healthy tissues of pigs for a short duration of time (1-2 days). The surrounding tissues were then sectioned to thin slices (10 µm), fixated and the activity concentration was measured using autoradiography. The diffusion length was calculated as the fit to the activity concentration in concentric rings around the source. Damage to the tissue was also observed in the histopathology.

Results: The diffusion length was measured in the brain, kidneys, pancreas, spleen, liver, lung, and muscle tissue. In all samples the measured value was in the range 0.25-0.3 mm. We observed tissue damage up to a distance of ~0.5-1.5 mm from the source. Conclusions: We found that the diffusion length in healthy tissues is ~0.3 mm which is in the order of magnitude of the values observed in small non-necrotic mice tumors. This is a good trade off between the desire to minimize the migration of radioactive atoms into healthy tissues and minimize the dose, and the full coverage goal to minimize the risk of recurring cancer. The new data obtained in this study will help optimize future treatment plans.

Combining Alpha-DaRT with Convection Enhanced Delivery for improved tumor dose coverage

Lior Epstein, Israel Gannot, Itzhak Kelson, and Lior Arazi

Background: Alpha DaRT is a new solid tumor treatment technique that relies on alpha particles to deliver a lethal radiation dose to the tumor while sparing adjacent healthy tissue. Alpha DaRT employs implantable sources carrying low activities of 224Ra, that continually release from their surface a chain of short-lived alpha emitting atoms. These spread in the source vicinity by diffusion, delivering a therapeutic dose through their alpha decays over a region measuring ~3-5 mm in diameter. Although the rapid fall-off of the radiation field allows sparing surrounding healthy tissue, it requires the use of multiple sources at a typical spacing of ~4 mm. This presents a challenge when treating deep-seated hard-to-reach tumors.

Purpose: Here, we present a preliminary theoretical study on the feasibility of combining Alpha DaRT with convection-enhanced delivery (CED). CED was originally developed to treat brain tumors from a single penetration point, by using induced convection to drive drugs radially outward from the tip of a catheter inserted into the tumor. The motivation of the present study is to extend the effective therapeutic range of Alpha DaRT using a similar flow pattern.

Methods: We consider two scenarios for the combination of Alpha DART and CED and calculate the tumor dose distribution: (1) placing several wire-like Alpha DaRT sources inside the catheter tube, close to its tip inside the tumor, and driving a constant flow through it; (2) creating a 212Pb-rich fluid in an external vial containing several Alpha DaRT sources to be administered through the catheter. We present a numerical model to calculate the tumor dose distribution in both scenarios.

Results: We calculated the dose as a function of distance from the catheter entrance point for different source activities, flow velocities and treatment duration, for both scenarios. When placing the sources close to the catheter outlet inside the tumor, the proximity of the sources allows some 220Rn to reach the tumor, while when the sources are placed inside the vial, 220Rn fully decays inside the catheter and does not reach the tumor. In both scenarios, the addition of a convective flow to the Alpha DaRT treatment provides coverage of a spherical region with a diameter of ~2-3 cm using a few hundred μCi 224Ra.

Conclusions: The combined treatment of Alpha DaRT and CED can potentially allow treating large tumors from a single penetration point. Of the two considered treatment scenarios the second one is favourable - placing the 224Ra sources inside an external vial - due to its relative simplicity, small-diameter catheter needle and the possible use of higher activities. Further experimental studies are required to investigate the practicality and limitations of the proposed idea.

POSTERS

Poster Session 1

Validation of a MnO_2-Based Method for Simultaneous Detection and Quantification of Low Concentrations of Pb-210 and Ra-226 in Drinking Water Using Gamma Spectroscopy

Mor Ben-Lulu, Ofer Aviv, Dani Vaknin, Natanel Chichportich, Zohar Yungrais, Getaneh Abebe and Michal Brandis

The Water Laboratory routinely conducts radioactivity measurements of natural radionuclides in drinking water samples from various water sources, intended for public consumption in Israel. According to the Ministry of Health regulations, drinking water should be tested for the identification and quantification of 12 natural radionuclides, including Ra-226 and Pb-210. In Israel, the activity concentration limits for these radionuclides are set at 0.1 Bq/L and 0.2 Bq/L for Ra-226 and Pb-210, respectively. While a standardized method for Ra-226 quantification is well-established and routinely applied, a validated method for Pb-210 is still lacking.

Herein, a validation was conducted to evaluate a method ,based on recent work by O. Aviv et al. [1], for simultaneously determining low activity concentrations of Pb-210 and Ra-226 in drinking water.

The method relies on MnO2 fibers for the adsorption of the radionuclides of interest, followed by gamma-ray spectrometry. The method's linear response and reproducibility were confirmed through comparisons with established techniques and certified reference materials for both radionuclides. Recovery rates exceeded 80% for Pb-210 and Ra-226 across different matrices, including tap water and high-TDS (total dissolved solids) water, with minimal variability (CV<5%).

Sensitivity tests demonstrated minimum detectable activities of 0.008 Bq/L for Pb-210 and 0.01 Bq/L for Ra-226 after 24 hours of measurement, meeting international regulatory thresholds for drinking water.

Robustness tests exhibited the method's resilience to variations- including measurement geometry, fiber-compressing techniques, and prolonged storage. Uncertainty analyses quantified contributions from counting statistics, detector calibration, and gamma-ray emission probabilities, yielding a combined uncertainty below 10%.

This validated method integrates rapid sample preparation, high sensitivity, and costeffectiveness, enabling the simultaneous analysis of both Pb-210 and Ra-226 in drinking water. Its adaptability to diverse water sources and operational simplicity establishes it as a valuable tool for environmental radioactivity laboratories, streamlining routine monitoring of these radionuclides.

Neutron-induced reactions in a high density plasma at National Ignition Facility

S. Bhattacharya[1], M. Paul[1], R. N. Sahoo[1], D. Casey[2], C. Cerjan[2], J. Jeet[2], C. Velsko[2], A. Zylstra[2], M. Avila[3], E. Lopez[3], J. C. Dickerson[3], C. Fougères[3], J. McLain[3], R. C. Pardo[3], K. E. Rehm[3], R. Scott[3], I. Tolstukhin[3], R. Vondrasek[3], M. Tessler[4], S. Vaintraub[4], T. Bailey[5], L. Callahan[5], A. M. Clark[5], P. Collon[5], Y. Kashiv[5], D. Robertson[5], U. Koester[6], H. F. R. Hoffmann[7], M. Pichotta[7], K. Zuber[7], T. Doering[8], R. Schwengner[8], R. Purtschert[9]

1 Hebrew University of Jerusalem, Israel
2 Lawrence Livermore National Laboratory, Livermore CA USA
3 Argonne National Laboratory, Argonne IL USA
4 Soreq Nuclear Research Center, Yavne, Israel
5 University of Notre Dame, Notre Dame IN USA
6 Institut Laue-Langevin, Grenoble France
7 Technical University Dresden, Dresden Germany
8 Helmholtz Zentrum Dresden Rossendorf, Dresden Germany
9 Institute of Physics, University of Bern, Bern, Switzerland

The thermodynamic conditions of plasma density, temperature, pressure, and neutron density during the implosion of a deuterium-tritium (DT)-filled capsule by laserinduced inertial confinement at the National Ignition Facility constitute a unique stellar-like laboratory environment. In this study, we investigated neutron-induced reactions on 40Ar seeds added to the DT capsule, specifically the 40Ar(n,2n)39Ar (268 years) reactions 40Ar(n,γ)41Ar (110 min) and we also searched for the signature of a rapid two neutron capture 40Ar(2n,γ)42Ar (32.9 years) reaction, similar to the r-process occurring in stellar explosive nucleosynthesis. To validate the 39Ar findings, we conducted in parallel direct experiments to measure for the first time the total cross-section of the 40Ar(n,2n)39Ar reaction using a 14-MeV neutron activation. The resulting long-lived argon isotopic residues were analyzed using Noble Gas Accelerator Mass Spectrometry at the ATLAS accelerator, Argonne National Laboratory [1]. We will present preliminary results of these experiments.

Adaptive real-time protective system for critical facilities and infrastructures against blast wave loading

Brandys I., Ornai D., Levy R.

Introduction: Munitions such as surface-to-surface rockets, air-surface missiles, vehicle-borne improvised explosive devices (VBIEDs) and unmanned autonomous aerial vehicles (UAAVs, drones) are used by armies, terrorists and violent non-state actors against critical facilities and infrastructures (CFIs). The blast wave and fragmentation resulted by their explosions cause horrible physical, social and economical consequences, starting from injuries and loss of lives, up to operational disruption of CFI. Currently, active protective systems (APS) are implemented in armored vehicles [1].

Technological improvements enable their almost immediate threat detection and responsive neutralization. These APS are not suggested for CFIs since their ammunition is dangerous during its storage and operation. An active system for blast resistance of structures, based on moving structural elements, was first mentioned by Nordell [2], but have not been developed further.

A novel adaptive real-time protective system (ARTPS) is suggested for CFI protection against blast wave loading and fragmentation. It is designed to withstand near-miss explosions at minimal distance Rp from the CFI, as presented for a single façade in Figure 1. Rp is the perimeter radius from the CFI's façade where the threat is stopped and initiated, e.g. concrete barricade for VBIED and protective net for UAAV or munition with impact fuse. The ARTPS should be fully engaged in a very short time derived from the detection and response time considering Rp for the specific scenario.

The arrival time of the blast wave should be greater than the ARTPS readiness time for moving a protective plate aside the CFI's façade or opening an inclined protective plate, that will both protect against decreased blast loading. It may reduce casualties and maintain structural functionality (defined as protective category 1 [3]). The ARTPS can be operated (1) manually, when regional or local alert is given, or (2) automatically, by Sensing, Identification, Controlling, Engagement, Dynamic response and Damage evaluation (SICEDD).

Artps methodology: Similarly to FEMA three layers of defense against terrorist attacks (1st & 2nd layers: natural or manmade barriers, 3rd layer: the façade of the building) [4], the ARTPS has an external layer with fast on ground or air-borne threats sensing and identification system, shown in Figure 1. These can include chemical explosive sensorsa , electrooptical sensorsb , optical sensors and pressure sensorsc that are the inputs to the control system, which accounts the protective requirements and resistance capacity against single strike or multiple strikes. It is used for the feedback of damage evaluation due to the blast loading. Single strike requirement enables up to plastic response while multiple strikes limit the response to the elastic regime of the protected CFI and the ARTPS components. The permissible responses are based on the supports' angle of rotation and the ductility ratio (the maximum dynamic deflection divided by elastic or equivalent deflection, depends upon the static scheme).

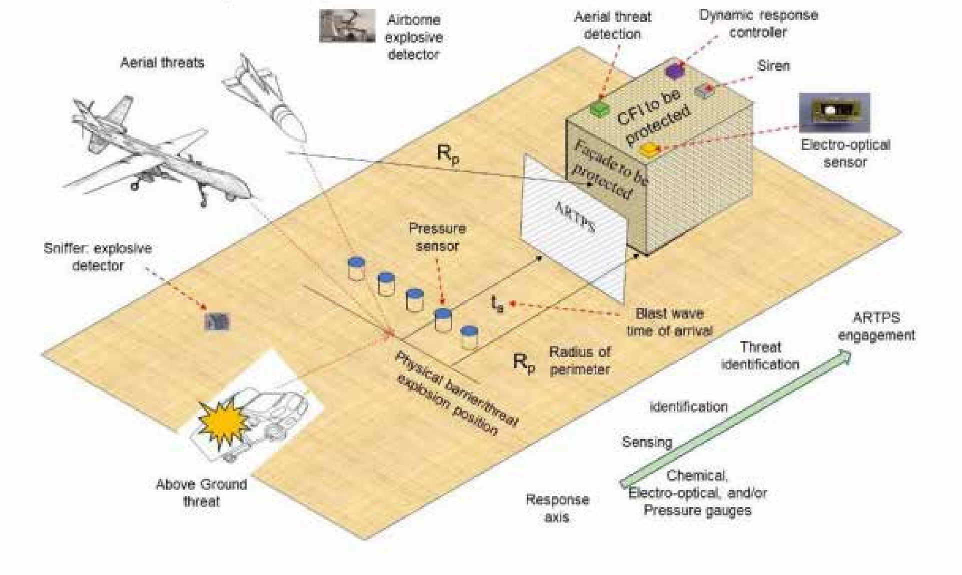

Figure 1. General architecture of the ARTPS

Sicedd system: Triggered by the dynamic controller, the ARTPS changes within milliseconds the structural mass, damping, stiffness (and the resulted resistance), e.g. by raising and firmly attaching protective steel plates aside the front side of the CFI's façade. It is enabled by a single or multiple mechanisms, such as electric motors, linear belt drives etc. After the blast occurs, structural is evaluated. In case of a single strike protective capacity damaged elements should be replaced, while for multiple strikes protective capacity, the protective system remains elastic with no need for any replacement. The ARTPS control flowchart is displayed in Figure 2.

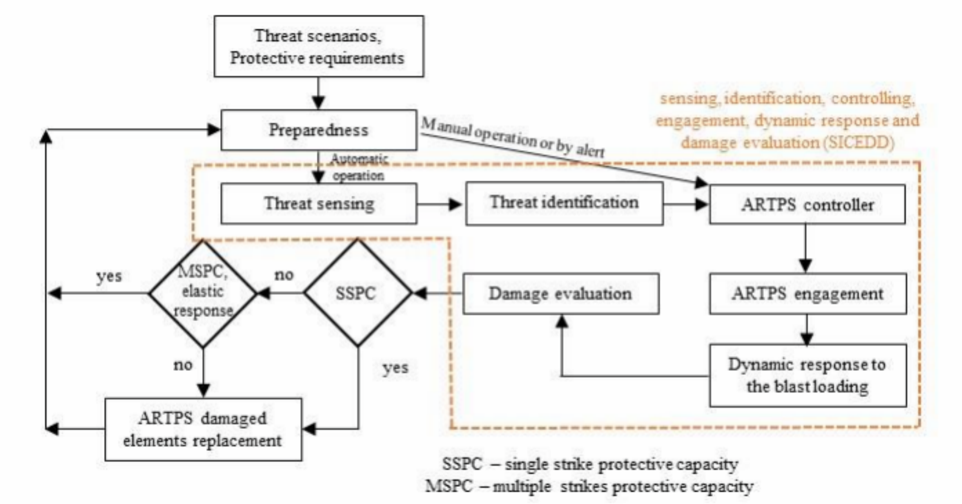

Figure 2. ARTPS open loop control flowchart

Summary: In this paper, the ARTPS' principles, control method and response mechanisms including time stages are defined, along with presenting two dynamic responses to above-ground and aerial threat scenarios. It can be used in protecting existing and new CFI.

Developing and constructing a thermal conductive measuring system for soil samples

Chricker Raz, Levi Moshe, Marzuk Avi, Panker Avimelech, Peretz Liel, Izhak Shai, Hajbi Tai-El, Vaknin Matan, Sadia Yatir, Ben-Yehuda Ohad

NRCN

Background: In recent years, there has been ongoing activity both locally and globally to examine the feasibility of disposing of radioactive waste at depth. As an initial pilot, it was decided by the NRCN to examine the disposal of approximately 60 Cs137 sealed sources at an intermediate depth (approximately 150 meters) at a designated site in the Yamin plain at the Negev [1,2].

In the disposal of heat-generating sources, there are two central thermal safety requirements. The first is the maintenance of ground stability (chemical, mechanical, mineralogical, etc.). The second is the preservation of the structural stability of the engineered disposal containers (canisters), which contain the sealed sources. Therefore, a thermal model has been developed, in which a generic borehole design was embedded. The model, which validates the planned disposal configuration and its compliance with safety requirements, is based on thermal conductivity values for various soil formations and borehole fillers (bonding materials), as found in the literature. To validate these values and support the model, experimental characterization of the thermal conductivity values for the soil formations and fillers is required.

Method: Further to the above, the development, construction, and validation of a system for characterizing the thermal conductivity of soil samples (Figure 1) was initiated. In the first phase, a literature review was conducted, in which various measurement methods were examined, and a 'comparison method' was selected as the basis for the measurement system. In the second phase, the experimental system was constructed, including the characterization of the heating element, the vacuum system, the thermocouples, and the data logger. In the final phase, calibration experiments were conducted using various samples (e.g., MACOR, Alumina) with thermal conductivities within the typical range for soil samples (1-5 W/m·k). The system operates under a primary vacuum atmosphere (below) and includes a mechanism for compensating axial pressure on the sample.

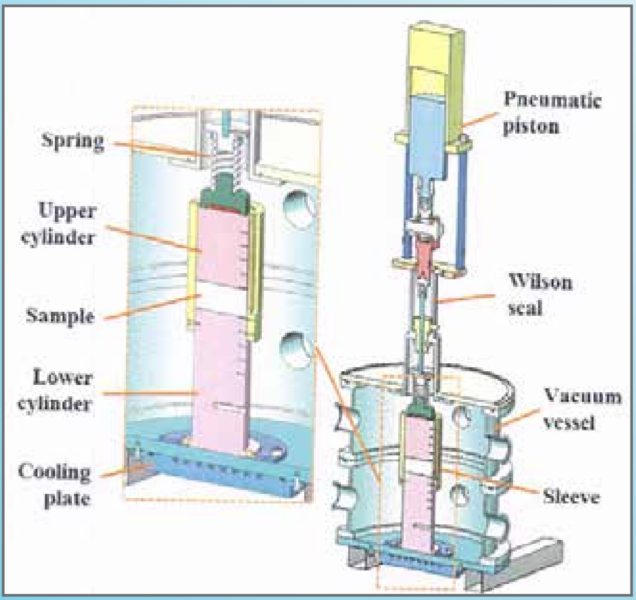

Figure 1: main parts of the thermal conductive measuring system

Results: A system for characterizing the thermal conductivity of soil samples was established. The characterization will be performed within a temperature range of 30-100°C. Several calibration experiments were conducted, and a deviation of 20% for the average value was observed, in relation to literature values (measurement error of ±10%).

Discussion and Conclusion: A system for characterizing the thermal conductivity of soil samples was developed and established, based on literature review. The system was calibrated using various samples with thermal conductivities within the typical range for soil samples. A deviation of 20% for the average value was observed, in relation to literature values (measurement error of ±10%). In the next phase, the thermal conductivity of the soil samples will be characterized, considering the observed error.

Quick Sort Triage Critical Mission: Detecting Internal Exposure in Mass Radiological Emergency

Hanan Datz, Ofer Aviv, Henry Spitz

In radiological emergencies involving dispersal of radioactive materials, rapid identification of individuals with potential internal radiation exposure above action guidelines is critical for effective medical treatment. We present an innovative Quick Sort triage method utilizing a commercial Geiger-Mueller (GM) detector to help identify individuals who may have received an intake of radioactive material at levels corresponding to one Clinical Decision Guide (CDG) - a level at which a physician may consider initiating medical treatment to enhance radionuclide removal from the body. The CDG values, established by NCRP Report No. 161 and referenced in NCRP Report No. 166, correspond to the adult 50-year committed effective dose of 250 mSv.

The triage method employs a portable GM detector positioned against the lower anterior torso of a seated subject in a bent-forward position to maximize body tissue coverage. The response of the GM detector is related to a quantity of internally deposited activity using a novel anthropometric phantom that exhibits the physical and radiological properties of the adult human lower thoracic and abdominal cavity containing a known quantity of radioactive material. This work describes the detection efficiency of a Ludlum Model 133-4 GM detector used with the phantom containing the equivalent of 1 CDG of radioactive material received during the first 24-hr post intake. Individual sealed sources of 232Th and 137Cs were separately inserted at various locations in the phantom to simulate conditions following intakes that generate a range of photon energies.

Results using the phantom demonstrate that the Quick Sort triage protocol provides a rapid, low-cost screening method that can be implemented with minimal operator training. The approach is suitable for efficiently screening large populations and sufficiently robust to identify individuals who may have a localized (hot spot) or uniform deposition of radioactive material approaching or exceeding the adult 1 CDG threshold.

Radiological incidents and accidents involving mobile high activity sources

Fried Y., Epstein L. and Brandis M.

Work conducted for ICRP Task Group 106, Committee 4

The International Commission on Radiological Protection (ICRP) recognized the need to clarify the application of the commission's recommendations on radiological protection of workers, the public, and environment to activities involving mobile high activity sources. Task Group 106 was created with the aim to develop a report that will cover uses of sealed sources in industrial radiography, and other instances in which high activity sources are used in a mobile setting. This literature survey of events related to high activity mobile sources was part of the mentee's duties in the ICRP Mentorship Programme - a program to engage early-career professionals and scientists in ICRP Task Groups.

The International Atomic Energy Agency (IAEA) defines a radiation accident as "an event that has led to significant consequences to people, the environment or the facility" [1]. Since each radiation accident is unique and has its own characteristics, any attempt to derive generic rules based on an individual accident constitutes a challenge, especially when the main goal is to prevent or best manage potential future accidents [2]. According to the United Nations Scientific Committee on the Effects of Atomic Radiation (UNSCEAR), the leading radiation accidents resulting in early acute health effects or significant population exposures are industrial accidents [3]. We will focus on radiation accidents with mobile high activity sources for industrial radiography.

The Health Protection Agency (UK) and the Centre d'étude sur l'évaluation de la protection dans le domaine nucléaire (CEPN, France) publish lessons learnt from radiological incidents in a shared website [4]. Table 1 presents the different types of incidents divided according to the failure mechanism [4]:

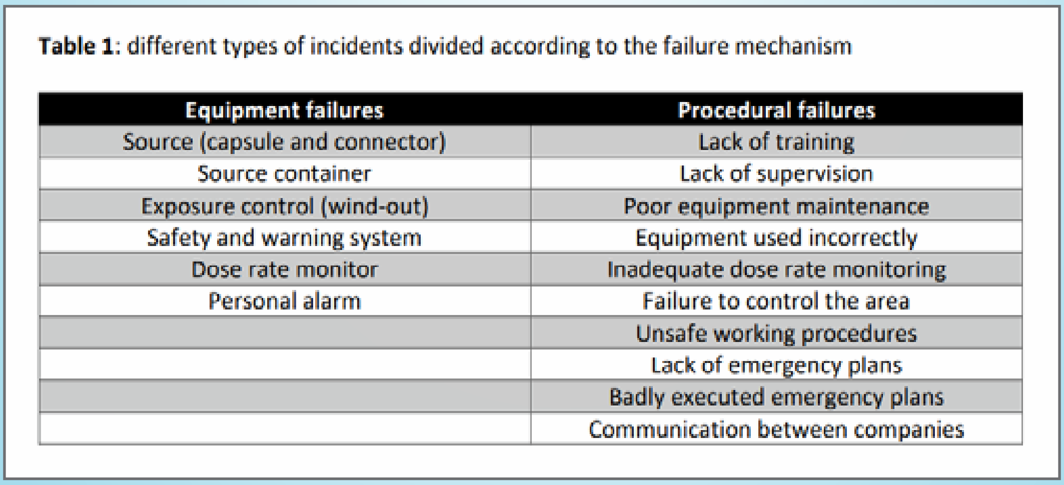

Table 1: different types of incidents divided according to the failure mechanism

Equipment failures	Procedural failures
Source (capsule and connector)	Lack of training
Source container	Lack of supervision
Exposure control (wind-out)	Poor equipment maintenance
Safety and warning system	Equipment used incorrectly
Dose rate monitor	Inadequate dose rate monitoring
Personal alarm	Failure to control the area
	Unsafe working procedures
	Lack of emergency plans
	Badly executed emergency plans
	Communication between companies

We present two case: The Radiological Accident in Chilca in 2012 [5], and the radiological accident in Nanjing, China in 2014 [6]. Each case will include a short description, continue with a list of the causes of the accidents, and end with conclusions and lesson learned.

Preliminary Study on the Colorization of Neutron-Induced Tracks in CR-39 Detectors

Nir Pour and Gal Amit

Background: CR-39 detectors are widely used in neutron dosimetry due to their high sensitivity and reliability. This study introduces a novel approach to enhance track visualization through colorization, with the potential to improve track analysis and interpretation. Ultimately, this method aims to improve the accuracy of dose evaluation for passive personal dosimeters, by enabling a rough estimation of the neutron energy spectrum, as outlined in ICRP 103.

Method : A modified post-etching process was developed to introduce color into the neutron-induced tracks in CR39 detectors. Several staining materials were tested for their ability to adhere to track characteristics while preserving the integrity of the detector material. Among the materials tested, $FeCl_3$ in an aqueous solution and Prussian blue demonstrated the best results, producing distinct and consistent track coloration.

Results: Preliminary results demonstrated successful colorization of neutron-induced tracks, achieving distinct and visually enhanced features.

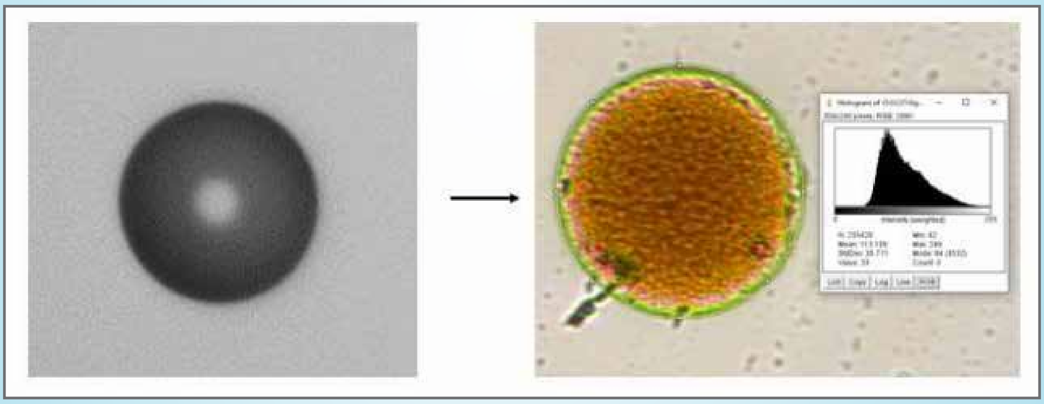

Tracks were clearly distinguishable, enabling easier differentiation and potential feature analysis. While the correlation between track color gradients and neutron energy remains under investigation, these findings confirm the feasibility of the method.

Discussion and Conclusions: The colorization of neutron-induced tracks in CR-39 detectors represents a promising innovation in neutron dosimetry. This approach has the potential to enhance the accuracy and efficiency of track identification, paving the way for energy-based track classification. Although further research is required to establish quantitative correlations, these preliminary results indicate strong potential for practical applications in radiation detection and neutron dosimetry.

Safety-Critical Software Design: Modular Architecture for Enhanced Reliability

Salomon Yossi, Knafo Yakir, Sheinfeld Mati, Dadon Shay, Osovizky Alon, Manor Avi
Nuclear Research Center - Negev (NRCN)

Designing reliable software for safety-critical systems poses significant challenges, particularly in managing complexity, while achieving rigorous compliance with safety industry standards, ensuring predictable behavior. Conventional monolithic architecture often struggles due to complex interdependencies and limited fault isolation. To address these challenges, we propose a modular architectural framework inspired by IEC 61508, the international standard for the functional safety of electronic safety-related systems.

IEC 61508 emphasizes safety in embedded systems and includes a dedicated chapter on the software safety lifecycle. It provides guidelines covering the entire development lifecycle, from the requirements phase through architecture design, supported tools, testing, and validation. Key aspects include robust input validation, error-handling mechanisms, and defensive programming techniques to protect against invalid inputs and system faults.

Following this standard, we designed a simple, single-threaded architecture without an operating system. This approach eliminates race conditions and shared memory issues, enhancing system reliability and predictability. Leveraging modern microprocessors, the design enables efficient execution on a single high-performance processor while supporting computationally intensive tasks without requiring an operating system. The architecture follows the single-responsibility principle, with small, self-contained modules and well-defined interfaces, ensuring clear communication between modules and minimizing potential failure modes.

Testing is conducted systematically using fault injection and boundary condition analysis, enabling precise verification of individual components. By avoiding the overhead and unpredictability of an operating system, the architecture achieves a deterministic and streamlined design suited for safety-critical applications. The modular structure allows components to be tested independently and as part of full system validation. Although the software is embedded, it remains adaptable for execution on a PC, facilitating simulation of long scenarios within a shorter timeframe.

This work demonstrates how the proposed framework aligns with IEC 61508, leverages modern microprocessor capabilities, and significantly enhances reliability, predictability, and maintainability compared to non-safety designs. Through practical implementation and rigorous testing, the methodology proves to be effective in advancing safety-critical software architecture and development.

Outsourced Software Development: Strategic Risk Reduction for Software Systems

Salomon Yossi, Azot Noy, Gonen Ehud, Vax Eran, Dadon Shay, Manor Avi, Osovizky Alon

Nuclear Research Center - Negev (NRCN)

Outsourcing software development introduces significant risks to system security, integrity, and reliability. Our approach addresses these challenges by focusing on supply chain vulnerabilities, enforcing secure development practices, and implementing robust technological safeguards to ensure compliance with safety standards and resilience against potential threats.

A key aspect of the framework is adopting zero-trust architecture principles, which require verification of all users and devices at every stage of the development process. This strategy minimizes insider threats and prevents unauthorized access. Additionally, advanced code source tracking enhances security by maintaining a detailed record of all software components, ensuring traceability, and preventing the integration of malicious or unauthorized code. Secure communication protocols protect sensitive data from tampering and leaks. Since our systems operate in a closed environment, threats primarily arise when integrating externally developed software or hardware.

To further enhance security, the approach incorporates technology compartmentalization, isolating critical components to contain potential breaches and prevent system-wide propagation. Sandboxed development environments ensure that untested or malicious code does not impact production systems.

Continuous security validation mechanisms, such as automated scanning and real-time testing, are integrated to detect and mitigate vulnerabilities as they emerge, ensuring no exploit goes undetected. Additionally, multi-layered authentication safeguards development environments, making unauthorized access through compromised credentials significantly more difficult. Strict intellectual property protection is enforced through both contractual and technical safeguards, preserving the integrity of proprietary assets.

To proactively detect threats, machine learning-based anomaly detection monitors unusual patterns in user behavior and code changes, flagging potential security risks for immediate review. Real-time code monitoring provides continuous oversight, reducing the likelihood of vulnerabilities or malicious modifications being introduced into the codebase.

By integrating technological, legal, and procedural controls, this approach offers a comprehensive and proactive strategy for mitigating risks in outsourced software development. It ensures system integrity, compliance with safety standards, and robust protection against emerging threats, making it a vital methodology for securing software systems and mitigating threats.

Entangled charge carriers in LiF;Mg,Ti Traps/Luminescence Centers (TCs/LCs) - A Theoretical Approach

Dr. Daniel Sattinger[1], **Dr. Max Platkov**[2]

1 Israel Atomic Energy Commission (IAEC)
2 Nuclear Research Center Negev (NRCN)

Background: A practical and unique experiment is proposed in order to verify and understand the quantum entanglement (QE) of charge carriers trapped in LiF:Mg,Ti trapping centers/luminescence centers (TCs/LCs). Few limited experiments have been reported in the past, and none of them were officially published. One has been carried out by Robert Desbrandes and Daniel L. Van Gent [1]. In this experiment the entanglement between electrons in ion traps was investigated by demonstrating correlated Thermoluminescent (TL) signals in two remote locations. Here, we propose a new theoretical approach and use previous studies concerning Trapping centers (TCs) and Luminescent centers (LCs) as micro-nano scale trap entities for entangled charge carriers (electron & hole). We use well known quantum mechanics formalism in order to construct the various trapping configurations (the base vectors) and entangled states between electrons and holes. The main idea is to experimentally verify the existence of the relevant TL peaks (i.e., peaks 4, 5a & 5) which are directly associated with the TC/LC centers. These peaks/signals are expected to be detected in a remote slave TLD chip due to an optical bleaching experiment in a master chip. We see an advantage in this approach due to the ability to research the entanglement between charge carriers by the examinations of the direct conversion signals associated with the various traps.

Methods and Methodology: We shall use TLD -100 (LiF:Mg,Ti) single crystal master chips and slave chips. The master chips will be used in the main laboratory and the slave chips in experiments that will be carried out in remote location. We suggest to conduct experiments that will be able to detect the physical mechanism that cause the entanglement of electron - hole in LiF:Mg,Ti crystals. We shall create entangled charge carrier in the TCs/LCs during irradiation by exposing the TLD chips to a radiation source and swapping the entanglement of photons to the electrons/holes in the TCs/LCs complex. We plan to bleach the master chip in well-known light wave lengths that are expected to create conversion between the main dosimetric peaks (4,5a,5). This will also cause the collapse of the wave function of the entangled states. Every experiment must be followed by a very accurate glow curve deconvolution protocol of the expected TL signal of the slave chip. Successful preliminary experiments, i.e., positive revealing of QE would give the insight to new theoretical calculations (density matrices, degree of QE, entropy ...) as well interesting practical applications (remote information transfer, fast remote dosimetry, etc...).

QE in LiF;Mg,Ti – TC/LC complex – Theoretical Approach

Entangled particles can be created by irradiation in LiF;Mg,Ti traps (TCs) and luminescence (LCs) centers that are spatially correlated, i.e., are bound together by some form of a long range interaction into a large complex [2-5]. This can be done by using entangled photons source and entanglement swapping to the trapped charge carriers. In this case the entangled particles are electron and a hole that occupied a TC/LC (Fig.1). There may be also other possibilities to create entangled charge carriers during the irradiation of LiF;Mg,Ti, i.e,. two electrons in close proximity in F2 centers, two holes in close proximity in V3 centers.

We shall define a TC/LC as a quantum system. A micro-nano dimension complex that has the ability to trap charge carriers during the irradiation stage.

TC/LC complex following irradiation can be populated at four different manners: The complex has capture (i) an electron – hole pair, (ii) only an electron, (iii) only a hole, or (iv) no charge carrier has been trapped (Fig.1). We can use vectors representation to define four states:

$|e+>$ – TC/LC has capture an electron.
$|e->$ – TC/LC has not capture an electron.
$|h+>$ – TC/LC has capture a hole.
$|h->$ – TC/LC has not capture a hole.

Following the irradiation process we can define our four basis vectors:
$|e+;h+>$ – the TC/LC complex has capture an electron – hole pair.
$|e+;h->$ – the TC/LC complex has capture only an electron.
$|e-;h+>$ – the TC/LC complex has capture only a hole.
$|e-;h->$ – no charge carrier has been trapped.

In order to get composite systems, we shall define independent product states for our charge carriers. Since we are using quantum systems we assume that the electron state is defined by the following linear combination $\alpha|e+>+\beta|e->$ and the hole state by $\gamma|h+>+\delta|h->$. We assume that each state is normalized: $\alpha^*\alpha+\beta^*\beta=\gamma^*\gamma+\delta^*\delta=1$.

The most general vector in the composite space of states describing a combined system is given by: $|\psi_{initial}>=a|e+;h+>+b|e+;h->+c|e-;h+>+d|e-;h->$ (1)
The coefficients a, b, c, d determine the probabilities to find adjust quantum mixed state (to be in one of the basis vectors).

After implying an external interaction (measurement) the wave function in (1) will collapse to one of the four possibilities. Every TC/LC complex can collapse to one of the four possibilities with probabilities $|a|^2 \ldots |d|^2$ respectively.

If we can write the product state describing the combined system $|\psi_{initial}>$ as the following product- $(\alpha|e+>+\beta|e->)\cdot(\gamma|h+>+\delta|h->)$ (2) than the initial state is not entangled. In any other case our charge carriers (electron/hole) are quantum entangled. In the entangled state the probability of finding a charge carrier (hole) in a certain state changes after we interact with the other charge carrier (electron). In this case the measuring is identifying the population of the TC/LC complex. By equating (1) to (2) and examine the coefficients it is easy to show that for not entangled state we must have: $a=\alpha\gamma$, b= $\alpha\delta$, c= $\beta\gamma$, d= $\beta\delta$. So, the initial probability for a hole to be in |h +> before the measurement will be α 2 γ 2+β2 γ 2= γ 2 (α2+ β 2) (3)

The sum of all probabilities is unity: α 2 γ 2+ α 2 δ 2+ β 2 γ 2+β2 δ 2= (α2+ β 2) (γ 2+ δ 2) =1 If we find by measurement the state |e +> than we have two options for the hole TC/LC occupation and our collapsed wave function becomes:
|e +> (γ $\sqrt{}\gamma$ 2+ δ 2 |h + > + δ $\sqrt{}\gamma$ 2+ δ 2 |h − >) (4)

We dedicate that the probability to find |h +> is γ 2 γ 2+ δ 2 = γ 2 (α 2 + β 2), i.e., the same result before the measurement.

If the initial state is entangled, we can write in general: |ψinitial >= α |e + ;h +>+ β |e + ;h −>+ γ |e − ;h +>+ δ |e − ;h −> (5)
Here, the initial probability for a hole to be in |h +> before the measurement is α2+γ2 .

If we find by measurement the state |e +> the collapsed wave function becomes:
|e + > (α $\sqrt{}\alpha$2+ β2 |h + > + β $\sqrt{}\alpha$2+ β2 |h − >) (6)

We dedicate that the probability to find |h +> is α 2 α2+ β2 , i.e., different result comparing to the initial probability. We conclude that in entangled state the result of measuring the quantum state of one charge carrier will affect the probability of the other. This can give us some knowledge of the entangled particle state and the motivation for various experiments to examine the e-h entanglement in TC/LC complexes as well other charge carriers combinations in other centers. Further, we can look at the maximum entangled states.

These states carry no information about the individual subsystems and form a singlet and triplet states:
|singlet state >=1/$\sqrt{}$2(|e + ;h −>− |e − ;h +>) (7)
The singlet state cannot be written as a product state. The same is true for the triplet states, which are also maximum entangled states.
|triplet state1>=1/$\sqrt{}$2(|e + ;h −>+ |e − ;h +>) (8)
|triplet state2>=1/$\sqrt{}$2(|e + ;h +>+ |e − ;h −>)
|triplet state3>=1/$\sqrt{}$2(|e + ;h +>− |e − ;h −>)

The maximum entangled states (7) and (8) carries the complete information of the composite system but no information of the individual subsystem. In general, the degree of entanglement in a given quantum mechanical system can be measured by the Entanglement entropy.

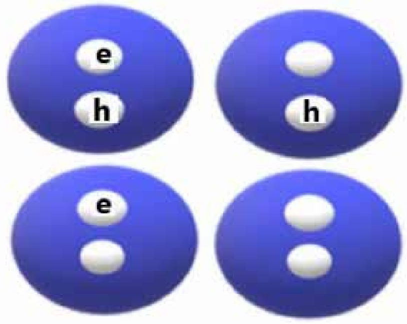

Fig1: Trapping Centers (TCs) Luminescence Centers configurations.

Discussion: Our objective in this research is to establish numerous unique experiments in order to verify and understand the entanglement of charge carriers trapped in LiF:Mg,Ti TCs/LCs. Here we've presented only the main theoretical idea. This experimental results can be expected to significantly enhance the dosimetric characterization of prominent TLD materials since a success in verifying and understanding the entanglement phenomena is directly connected to information transfer. Moreover, this information is independent of the distance between the materials (master chips and slave chips). Understanding the QE in TLDs can contribute to state of the art research in remote dosimetry, i.e., space dosimetry, underwater dosimetry etc.

The Ed Scale for Maintenance: a Comprehensive Framework for Evaluating and Prioritizing Maintenance Needs in Research Reactors

Y. Shaposhnik and E. Binkley

This paper introduces the Ed Scale for Maintenance, a structured framework designed to identify, evaluate, and prioritize maintenance needs within an organization. The scale provides a systematic approach to resource allocation and planning, ensuring optimal operation and prevention of failures. By categorizing maintenance tasks into five levels based on their complexity and impact, the Ed Scale aids in the efficient management of maintenance activities.

Keywords: Maintenance, Resource Allocation, Prioritization, Maintenance Management, Ed Scale

1. Introduction: Effective maintenance management is crucial for the reliability and longevity of any system or organization. Traditional methods often lack a structured approach to identifying and prioritizing maintenance tasks, leading to inefficiencies and potential system failures. This paper introduces the Ed Scale for Maintenance, inspired by the Bonen Scale of R&D Knowledge Gaps[1,2] , to address this gap. The Ed Scale categorizes maintenance tasks into five levels, providing a detailed framework for assessing and prioritizing maintenance activities.

2. The Ed Scale for Maintenance: The Ed Scale for Maintenance is designed to provide a comprehensive framework for evaluating and prioritizing maintenance tasks within an organization. Maintenance is a critical component of any operational strategy, ensuring the reliability, safety, and efficiency of systems and equipment. However, maintenance tasks can vary widely in complexity and impact, from routine daily fixes to major overhauls requiring extensive planning and resources. The Ed Scale categorizes maintenance tasks into five distinct levels, each defined by specific criteria such as the personnel required, the resources needed, the coordination necessary, and the duration of the task. By systematically categorizing maintenance activities, the Ed Scale helps organizations allocate their resources more effectively, focus on the most critical issues, and ensure that maintenance tasks are completed in a timely and efficient manner.

The five levels of the Ed Scale ranging from "Another Day in the Office" to "Tikkun Olam" provide a clear and structured way to assess maintenance needs. Each level represents a different degree of complexity and impact, allowing organizations to prioritize tasks based on their urgency and resource requirements. This structured approach not only enhances maintenance efficiency but also supports long-term operational sustainability.

2.1. Level 0: "Another Day in the Office": This level addresses daily maintenance tasks that are routine and require minimal coordination and effort. Tasks at this level are characterized by their simplicity and routine nature. They do not require specialized skills or extensive planning. Typically, these tasks can be handled by a small team of up to two persons. The resources needed are basic, often available on hand, and do not necessitate any special coordination. The duration for these tasks is short, generally completed within a single working day.

- **Personnel:** Up to 2 persons.
- **Resources:** No specific resources or qualifications needed.
- **Coordination:** None required.
- **Duration:** Can be completed within a single working day.
- **Examples:** Routine inspections, minor repairs, cleaning, and lubrication.
- **Impact:** These tasks ensure the smooth daily operation of the system without significant interruptions.

2.2. Level 1: "Easy Fix": This level involves simple maintenance tasks that require some procedures and readily available components. These tasks are slightly more complex than Level 0 and require a certain level of skill and coordination. They involve straightforward procedures that may need basic system isolation and coordination among team members. Personnel involved should be qualified, and while the tasks may be simple, they require adherence to specific procedures. The resources needed are typically on-the-shelf components and tools available within the organization. The duration for these tasks can extend up to a week.

- **Personnel:** Up to 6 qualified persons, potentially split into 2 groups.
- **Resources:** On-the-shelf components and tools available within the organization.
- **Coordination:** Basic system isolation and coordination required.
- **Duration:** Up to a week.
- **Examples:** Replacing worn-out parts, simple system isolation for minor repairs, basic component swaps.
- **Impact:** These tasks prevent minor issues from escalating into major problems, ensuring continued system reliability.

2.3. Level 2: "Just a Problem": This level involves more complex maintenance tasks requiring external resources and possibly reverse engineering. These tasks are more complex and may require external resources such as specialized tools, components, and personnel. They often involve detailed procedures and preplanning, including reverse engineering if necessary. Personnel required for these tasks include both internal staff and external specialists, necessitating a larger team. The resources needed may not be immediately available and might require procurement. These tasks can take up to 14 working days to complete, with up to 100 days of preparation time for procurement and planning.

- **Personnel:** Up to 10 persons, including external specialists.
- **Resources:** Off-site resources such as tools, components, and specialized personnel.
- **Coordination:** Detailed procedures, training, and pre-planning involved.
- **Duration:** Up to 14 working days, with up to 100 days for procurement and preparation.
- **Examples:** Integration of new components, significant repairs, modifications requiring custom tools or parts.
- **Impact:** These tasks address significant issues that require more extensive planning and resources, ensuring long-term system stability.

2.4. Level 3: "A Project": This level involves major maintenance activities requiring extensive planning and multiple expert groups.

Tasks at this level are large-scale projects that require extensive planning, coordination, and significant resources. These tasks involve multiple expert groups, each with specialized skills, and necessitate the use of specific production tools and long lead times for procurement. Detailed planning and safety assessments are crucial, as these projects can take several months to complete, with up to a year for preparation. The complexity and scale of these tasks require comprehensive coordination among different teams and thorough execution.

- **Personnel:** Multiple expert groups, each up to 6 persons.
- **Resources:** Specific production tools, extensive pre-planning, and long lead times for procurement.
- **Coordination:** Involves detailed planning, coordination, and safety assessments.
- **Duration:** Several months, with up to a year for preparation.
- **Examples:** Large-scale system overhauls, major equipment upgrades, significant retrofitting projects.
- **Impact:** These tasks involve significant changes to the system, requiring extensive coordination and resources to ensure successful implementation.

2.5. Level 4: "Tikkun Olam": This level involves first-of-its-kind maintenance tasks with unknown gaps, requiring innovative methods and R&D. These tasks are characterized by their high uncertainty and complexity, requiring innovative methods and extensive research and development. Multidisciplinary teams, potentially including R&D personnel, are essential to address these unprecedented challenges. The resources needed include new methods and extensive research efforts. Planning for these tasks is comprehensive, involving high levels of coordination and uncertainty. The duration is indeterminate and can span several years, reflecting the novelty and complexity of the tasks.

- **Personnel:** Multidisciplinary teams, potentially including R&D personnel.
- **Resources:** New methods, extensive research, and development efforts.
- **Coordination:** Comprehensive planning, high uncertainty, and extensive testing and validation.
- **Duration:** Indeterminate, potentially years.
- **Examples:** Developing and implementing novel maintenance strategies, pioneering solutions for unprecedented issues.
- **Impact:** These tasks involve high-risk, high-reward maintenance activities that can significantly advance the state of the system or technology.

3. Application of the Ed Scale: The Ed Scale for Maintenance provides a structured approach to identifying, evaluating, and prioritizing maintenance tasks. Applying this scale involves several key steps, each aimed at ensuring the effective and efficient management of maintenance activities.

3.1. Identifying Maintenance Needs: Identifying maintenance needs is the first step in applying the Ed Scale. This involves comprehensively assessing the organization's maintenance requirements through various methods. Regular inspections are conducted to detect wear and tear, potential issues, and areas requiring maintenance. Reviewing historical maintenance logs helps identify recurring problems 4 and areas that have required frequent attention. Utilizing advanced condition monitoring systems allows tracking the health and performance of equipment and systems in real-time. Additionally, gathering input from maintenance staff and operators who are familiar with the day-to-day operation of the systems can provide valuable insights into potential maintenance needs. Thoroughly identifying maintenance needs ensures that no potential issues are overlooked and that all maintenance tasks are considered for evaluation.

3.2. Evaluating Each Criterion: Once maintenance needs are identified, each task is evaluated based on the criteria outlined in the Ed Scale, including severity, frequency, complexity, resource requirement, and time sensitivity. The severity criterion assesses the potential impact of the maintenance gap on system performance and safety, determining the consequences of not addressing the maintenance task, such as system failures or safety hazards. Frequency evaluates how often the maintenance gap leads to issues or failures, helping understand the regularity of the problem and its potential to disrupt operations. Complexity determines the difficulty in addressing the maintenance gap, including evaluating the technical challenges, the need for specialized skills, and the intricacy of the required procedures. Resource requirement assesses the amount of resources (time, money, manpower) needed to address the maintenance gap, estimating the costs, availability of necessary tools and components, and the number of personnel required. Time sensitivity evaluates the urgency of addressing the maintenance gap to prevent significant impact, determining how quickly the maintenance task needs to be performed to avoid severe consequences. By systematically evaluating each maintenance task against these criteria, organizations can obtain a clear picture of the relative importance and urgency of each task.

3.3. Prioritizing Maintenance Tasks: After evaluating each maintenance task, the scores for the criteria are aggregated to prioritize the tasks. Tasks with higher scores are given higher priority due to their potential impact on the system. This prioritization process ensures that critical maintenance activities are addressed promptly, while less critical tasks are scheduled appropriately. Prioritization helps in resource allocation by ensuring that resources are allocated to the most critical tasks first, optimizing the use of available personnel, tools, and budget. It also aids in scheduling by developing a maintenance schedule that addresses urgent tasks immediately and plans for less critical tasks over a longer period. Furthermore, it contributes to risk management by reducing the risk of system failures and safety incidents by addressing the most impactful maintenance needs first.

3.4. Planning and Allocating Resources: With the prioritized list of maintenance tasks, the next step is detailed planning and resource allocation. This involves assigning the right personnel with the necessary qualifications and expertise to each task, ensuring that all required tools and components are available and accessible for the maintenance tasks, and coordinating with different teams and departments to facilitate the maintenance activities, including system isolation, safety measures, and procedural adherence. Developing a comprehensive maintenance schedule that balances urgency with resource availability and operational constraints is also essential. Effective planning and resource allocation are crucial to ensure that maintenance tasks are completed efficiently and without unnecessary delays.

3.5. Implementation and Monitoring : The final step in the application of the Ed Scale is the implementation and continuous monitoring of the maintenance tasks. This involves carrying out the maintenance tasks according to the plan and schedule, ensuring that all procedures are followed, safety measures are adhered to, and the tasks are completed to the required standard. Continuously monitoring the outcomes of the maintenance activities is essential to ensure their effectiveness, which includes conducting performance assessments, gathering feedback from personnel, and tracking any recurring issues. Maintaining detailed records of the maintenance activities, including what was done, who performed the tasks, and any issues encountered, is also crucial for future reference and continuous improvement. Continuous monitoring and documentation help in identifying areas for improvement and ensuring that the maintenance process remains effective and efficient.

4. Validation of the Ed Scale: Validating the Ed Scale for Maintenance is essential to ensure its effectiveness and applicability in real-world scenarios. The validation process involves several key steps, starting with historical data analysis. This method involves analyzing historical maintenance records to identify patterns, common issues, and the effectiveness of previous maintenance activities. By comparing the performance and reliability of systems before and after the implementation of the Ed Scale, organizations can understand the impact of the scale on maintenance efficiency and system performance. Additionally, identifying trends in maintenance needs and outcomes helps determine if the Ed Scale accurately reflects the priority and urgency of maintenance tasks. Historical data analysis provides valuable insights into the scale's effectiveness and helps in fine-tuning its criteria and scoring system. Another crucial step in validating the Ed Scale is gathering feedback from maintenance experts. This process involves organizing panels of maintenance experts to review the scale, its criteria, and its application. Experts provide insights into the practical applicability of the scale and suggest improvements. Conducting interviews and surveys with maintenance personnel and managers who use the scale can highlight any challenges, strengths, and areas for improvement. Engaging with industry peers through peer reviews offers a broader perspective on the scale's effectiveness and relevance. Expert reviews ensure that the Ed Scale is practical, comprehensive, and aligned with industry best practices. Conducting empirical studies is also vital for validating the Ed Scale. This involves applying the scale in real-world scenarios and measuring its impact. Implementing the Ed Scale in pilot projects tests its effectiveness in a controlled environment, providing a practical understanding of how the scale performs under real-world conditions. Developing performance metrics to measure the scale's impact on maintenance efficiency, resource allocation, and system performance is essential. Metrics can include the number of completed tasks, time taken, resource utilization, and system downtime. Documenting case studies of organizations that have successfully implemented the Ed Scale offers detailed examples of the scale's application and its benefits. Empirical studies provide concrete evidence of the Ed Scale's effectiveness and help in identifying any areas that need further refinement. Validation is an ongoing process, and the Ed Scale should be continuously improved based on feedback and real-world experience. This involves conducting regular reviews of the scale and its criteria to ensure it remains relevant and effective. Continuously incorporating feedback from users and experts is essential for refining the scale. Additionally, adapting the scale to changes in technology, industry practices, and organizational needs ensures it remains up-to-date. Continuous improvement ensures that the Ed Scale remains a valuable tool for maintenance management and continues to provide significant benefits to organizations.

5. Conclusions: The Ed Scale for Maintenance offers a structured and comprehensive approach to identifying, evaluating, and prioritizing maintenance needs. By categorizing tasks into five levels based on their complexity, resource requirements, and impact, the scale helps organizations allocate resources efficiently and maintain optimal system performance. The validation of the Ed Scale through historical data analysis, expert reviews, and empirical studies ensures its effectiveness and applicability in real-world scenarios. Future work includes further validation of the scale and exploring its application in various industries, ensuring that it continues to evolve and meet the needs of modern maintenance management.

Disclaimer: Certain commercial equipment, instruments, or materials are identified in this study in order to specify the experimental procedure adequately. Such identification is not intended to imply recommendation or endorsement by the National Institute of Standards and Technology, nor is it intended to imply that the materials or equipment identified are necessarily the best available for the purpose.

Resistance and Risk Assessment of Tunneled Smr Npp Exposed to Earth Penetrating Weapons' Hits in a Multiyear Perspective

Gal Shany[1], David Ornai[1], and Robert Levy[2], Igal M. Shohet[1]

1 Department of Civil and Environmental Engineering, Ben-Gurion University of the Negev, BeerSheva, P.O.B. 653, Israel, 8410501
E-mail: galshany@gmail.com; ornai@bgu.ac.il; igals@bgu.ac.il
2 Department of Structural Engineering, Sammy Shamoon College of Engineering, Beer-Sheva, Israel, E-mail: roberle@sce.ac.il.

Civil society is gradually exposed to terror and war threats. The scenarios caused by these man-made extreme events are highly relevant to the continuous performance and safety of underground Critical Infrastructures (CIs) such as power plants and data centers facilities. The research is focused on the development of a risk informed decision support methodology, demonstrated on a case study of a tunneled CI in chalk rock, exposed to two threat scenarios: direct hits of Earth Penetrator Weapons (EPWs). The investigated CI is NuScale® Small Modular Reactor (SMR) NPP, hypothetically built in underground cavern, particularly its reactor building (RXB) including Structures, Systems and Components (SSCs). If this NPP and its nuclear power modules (NPMs) are damaged, it might lead to Core Damage (CD) and Large Release (LR) of radioactive materials to the atmosphere, with significant negative impact on public health, power supply, groundwater, air pollution and soil contamination. Therefore, the CI's protectiveness is essential along its service life that can reach more than 100 years. Integrated risk analysis and assessment methodology was developed defining the threat scenarios and addressing three levels for consideration: (1) Geotechnical level - the tunneled cavern stability and integrity; (2) Structural level - RXB stability and integrity; and (3) Systems and Components level - integrity and safe operation. An Integrated Fragility Model (IFM) was developed for blast induced instructure motions caused by the EPWs, based on seismic fragilities of NPP's and the Nuclear Engineering Institute (NEI) data of NPPs exposed to aircraft crash median tolerance values. The instructure motions were analyzed by analytical-empirical expressions of the ground shock that fit numerical simulations. A Physical Deterioration Model (PDM) of the tunneled cavern containing the CI, comprising a) gathering of large relevant data sets while determining the main parameters affecting the prediction; b) applying Random Forest (RF) algorithm for the service life prediction. The model was validated with chi-square and Cohen's Kappa tests with high level of significance.

Keywords: Cavern, Integrated Fragility Model, Machine Learning, Random Forest, SMR, In-structure Motions, Blast, Seismic Fragility

Artifact Removal in Medical Imaging of Embedded Fragments Containing Different Radioactive Materials

Shukrun R. H., Epstein L., Hershko I., Breitman D., Ben-Lulu, M., Yungrais, Z., Aviv, O., Fried, Y., Oren, Y., Datz, H., and Zalevsky Z.

Background: Explosive Radiological Dispersal Devices (RDDs) are radiological weapons designed to disperse radioactive materials using conventional explosives. Detonation of an RDD can result in shrapnel trauma injuries, with contaminated fragments. When arriving to seek medical help, the injured patient will undergo radiographic imaging, such as X-ray or CT scans, for triage and treatment. Fragments containing high activity may introduce significant imaging artifacts, such as blurring and saturation. These artifact can delay or even prevent correct diagnosis and medical care. This study proposes an advanced artifact removal technique to improve the quality of radiographic images with an embedded radioactive fragment.

Methods: The radiographic image and resultant artifact were produced using the FLUKA Monte Carlo code with the Flair user interface. To obtain the imaging plate response to the emitted radiation, we exposed the imaging plate to variuos source, representing a wide range of energies: 57Co, 60Co, 137Cs, 192Ir, and 241Am. We found the relationship between the isotope air kerma and the measured pixel value, for our imaging system. We then simulated a radiographic setup in FLUKA, including an X-ray source, an imaging plate, a torso phantom, and a radioactive fragment, to produce the image with the expected artifact. The artifact was produced for activities of 1 GBq, 10 GBq, and 100 GBq. ◦“◦◦ We developed a novel approach based on a modified Papoulis-Gerchberg superresolution algorithm to reduce the atrifact. By using Fourier transform on the blurred image, we can remove the zero-frequency components to preserve highresolution data, and then inverse transforms the image. Unblurred regions from the original image are reintegrated using a pre-defined mask, and the process is iteratively refined. Since the blurring originates from physical phenomena, we constructed a mask based on the fragments brightness, assumed to be the brightest object, and an importance matrix generated from the inverse of the distorted image and local contrast. This allowed our algorithm to iteratively enhance the most blurred regions while preserving overall image clarity.

Results: Our simulations revealed that 1 GBq fragments caused minimal blurring, while 10 GBq fragments produced significant artifacts for all isotopes - 57Co, 60Co, 137Cs, 192Ir, and 241Am. It was found that the low-energy photon emitter 241Am exhibits the least noticeable distortion, while 192Ir exhibits the most noticeable distortion. Application of the modified Papoulis-Gerchberg algorithm successfully identified the location of the radioactive fragment, enhanced the overall contrast of the image, and restored the anatomical details.

Discussion and conclusions: Our results highlight the impact of high-activity radioactive fragments on radiographic images, particularly in creating artifacts that obscure the fragment's surroundings. The developed algorithm effectively mitigates these artifacts, allowing for identification of the location of the radioactive fragment and improves image contrast. Our approach can help diagnoses in an RDD event, enabling faster medical response and reducing delays in treatment.

Characteristics of the mechanisms in vertically counter-current liquid-gas film, subjected to wall heat flux boundary condition

D. Ronen, **Y. Weiss**

Mechanical Engineering, Ben-Gurion University
Ben-Gurion Blvd. 1, Beer-Sheva - Israel

Background: Two-phase vertical shear flow of liquid and gas in a counter-current manner on a heated wall is very common and widely used in many applications, from electronic devises to heat exchanges and nuclear reactor cooling. This work addresses the highly complicated problem of detecting and analyzing the mechanisms involved in hydro-dynamic flooding leading to flooding Critical Heat Flux (CHF).

Methods AND Results: To do so, we analyze existing analytical and empirical data, with additional analytical modeling of two main problems. First is the potential inviscid flow model, which provide two flow stability conditions. Additionally, this model stresses the considerable impact of the surface tension on the flow stability for small disturbance wavelengths (fig-1). The second, is the two-phase viscous shear flow model for which detailed analytical analysis and numerical solution are presented.

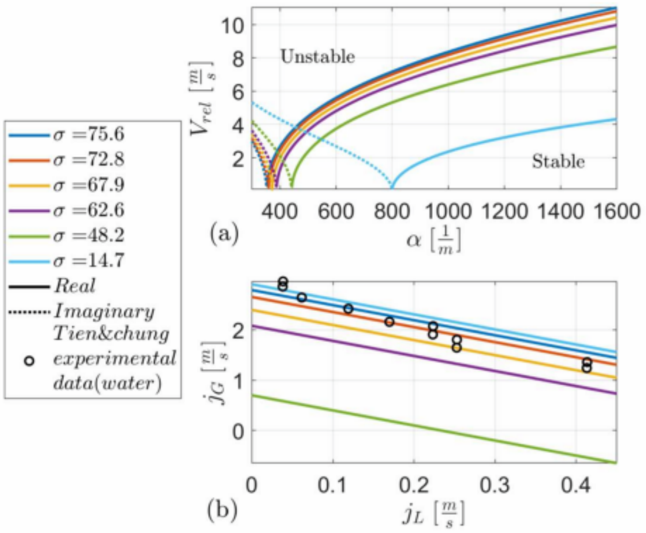

Figure-1: (a) The relative velocity as a function of the wave number for various surface tension values (b) Flooding curve for various surface tension values compared against Tien & Chung experimental data with water ($\sigma = 72.7\ 10^{-3}$ $[N/m]$) for $\alpha = 450[1/m]$. All surface tension values are given in 10^{-3} $[N/m]$.

Both models are analyzed for the same geometric parameters and saturation liquid and gas properties (density, viscosity and surface tension). The findings show that beyond a certain value of perturbation wave number the flow becomes unstable and is no longer affected by changes in its value. Moreover, in this region, surface tension variations impact the flow stability significantly. In addition, other thermal phenomena with substantial impact on the flow stability, such as the Marangoni effect, are reviewed.

For the first model the relative liquid-gas flooding velocity was analytically calculated as a function of the surface tension and the wave number. Being that the mathematical complexity of the second model is substantial, the same could not been done for it analytically. Alternately, a semianalytical expression was calculated as a function of the wave number only.

The first model analysis produced a correlation for the prediction of flooding as a function of the surface tension. The LHS is the relative velocity in means of the superficial velocities and the RHS is the dynamic apprehension of this analysis corresponding to the constant CW and CK used in Wallis and Kutateladze correlations, respectively. The flooding curve derived from Eq.1 is presented in Fig-2 as a function of the surface tension.

1) $$\tilde{j}_G + \hat{m}\tilde{j}_L = \sqrt{\frac{\frac{\rho_G}{\rho_L} - 1}{\xi^2 (g\sigma\Delta\rho)^{1/2}} \left(\frac{g\Delta\rho}{\alpha} - \alpha\sigma\right)}$$

Were $\xi = 1 - \delta/H$

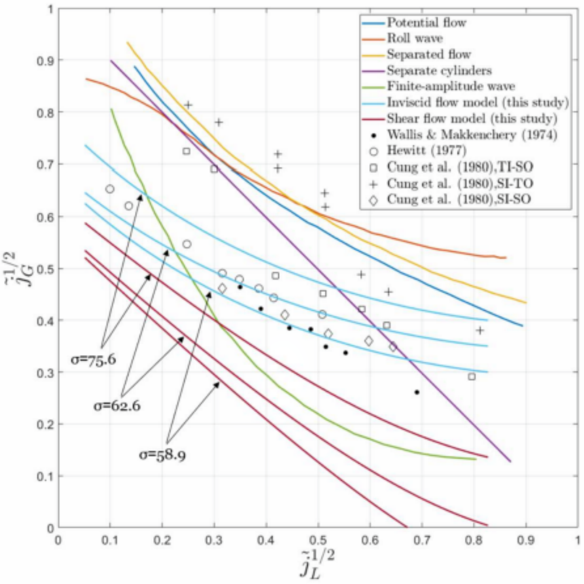

Figure-2: Comparison of various analytical models (solid lines) and numerical models (markers) with air-water flow data (H=31.8 mm). The wave numbers for

our models are αc = 450 (Inviscid flow) and αc = 775.2 (Shear flow). All surface tension values are given in10−3 [N/m].

The analysis revealed, in addition to the three regions of the flow frequently found in the literature, another region of interest of small perturbation wavelengths. Both models analyses are aligned well with this partition. The numerical solutions of the second model are validated against known cases from the literature and are in good agreement. Finally, the flooding CHF is calculated (eq.2) for different channel geometries and are found to be lower than other correlations predictions (Fig3). Further analysis of the thermal implications on the flow stability is needed, the surface tension and the Marangoni effect.

2) $$q''_{CHF} = \frac{h_{fg}}{\xi}\frac{H}{L_B}\left(\rho_G + \frac{1-\xi}{\xi}\frac{\rho_G^2}{\rho_L}\right)^{-1}\sqrt{\left(\frac{\rho_G}{\rho_L}-1\right)\left(\frac{g\Delta\rho}{\alpha}-\alpha\sigma\right)}$$

Were $\xi = 1 - \delta/H$ and for $\lambda \to \infty$

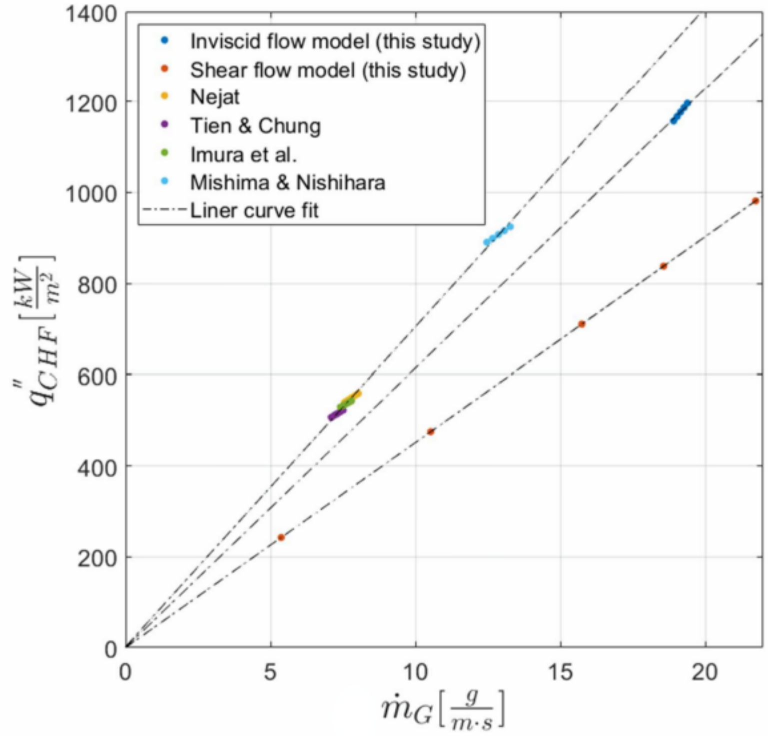

Figure-3: Comparison of various flooding CHF correlations with the results of this model calculated flooding CHF. The Heat flux values are presented as a function of the gas mass flow rate, each corresponding to a different channel width $a_c = 450$ (Inviscid flow) and $a_c = 775.2$ (Shear flow).

Summary and Conclusions: In this work we presented two linear analytical and numerical models to analyze the stability of a thin liquid film sheared by gas in a counter-current vertical flow, in the presence of a uniform heat flux. The main goal is to predict the onset of the flooding CHF through a deep understanding of the impact of the heating on the hydro-dynamic flooding. When addressing the flow problem, a comprehensive model for the prediction of flooding in inviscid two-phase shear flow is presented. This model emphasizes the critical impact of surface tension variations on the flow stability for small disturbance wavelengths. The literature usually divides the wavelength spectrum into three regions. The first is for very large wavelengths which requires the use of low-dimensional models. The second discuss similar wavelengths and film thickness and the third for wavelength not much greater than the film thickness, both are in very good agreement with the OS equation. In this work we present another region, in which the wavelengths are very small. In this region, the wavelength can no longer impact the parameters leading to flooding and the surface tension variations with temperature become the main factor influencing the flow stability. If we consider the liquid-gas interface to be a very thin membrane "holding" the liquid film at bay, for an increase in temperature, the surface tension reduces and the pressure that the membrane can endure decreases. This phenomenon is most significant for small wavelengths, when large amplitude waves are formed on the interface.

Another model presented is the viscous two-phase shear flow model, for which all numerical results were in excellent agreement with the cases found in the literature. For the two-phase shear flow, the natural stability and dispersion curves were plotted to map the stable and unstable conditions for both the low and high regions of the wave number α. For very small wave numbers, the flow was found to be unstable up to a constant wave number threshold. For the case of moderate wave numbers and above, on the other hand, the OS model shows very good agreement with the full NS accurate solution, capturing inertia effects properly.

When increasing the wave numbers, for the second region, the flow is always stable regardless of the wave number. However, further increase in the wave number value leads to a critical point of both α and Re, exactly as for the Poiseuille flow. For a flow under those conditions, an increase in the Reynolds number leads to the appearance of unstable eigenvalues, corresponding to specific wave numbers. At higher wave numbers (up to $\tilde{\alpha} \sim 17.6$) the flow is almost never stable, and the dominating unstable mode is different.

Due to the results of the potential inviscid flow model, the high wave number region of the two-phase shear flow is also examined. The flow seems to lose stability above a constant value, regardless of the gas Reynolds number. This is consistent with the results of the potential flow model analysis. Since we have analyzed the dynamics of a thin liquid film falling down a heated wall by means of a uniform heat flux, the critical values of instability are in fact the flooding CHF. The calculated heat flux values were found to be lower than those predicted by the known correlations. In other words, flooding CHF occurs earlier for the same gas mass flux. Several explanations are provided, among them the surface tension variations in temperature and, as a result, the Marangoni effect. The heating of the wall sets up surface tension gradients which induce thermo- capillary Marangoni effects. Thermal motion can produce capillary waves at a molecular scale and cause flow instability. In conclusion, the thermal influence on the flow stability is grave.

Thus, in order to properly predict the flooding CHF one must take into account all of the variables that are effected by the heating. As this is not a simple thing to do, the parameter with the most significant impact has to be considered as such. This research demonstrates that one of those parameters is the surface tension variations with temperature, which was somewhat overlooked in the literature. Lastly, flooding CHF is commonly referred to as the critical heat flux at which hydro-dynamic flooding accrues. This study shows that for a stable flow, a state of CHF can be reached prior to the flooding and effectively induce the hydro-dynamic flooding. Further research in needed to incorporate the heating implications on the flow stability.

Alpha particle identification using polymer detector

S. Segal, T. Kravchik, M.Platkov, S. Tsroya

Nuclear Research Center-Negev, POB 9001, Beer-Sheva 84190, Israel
Corresponding Author: shahars@nrcn.co.il

1. Introduction: CR-39 detectors made from C12H18O7 polymers are widely used for alpha, proton and neutron radiation measurements due to their sensitivity to high linear energy transfer (LET) radiation. When a CR-39 detector polymer is irradiated by a high LET radiation, defects are formed on its surface due to the breaking of its molecular structure. The defects have a size of only about 10 nm and are therefore known as "latent tracks"(1)..In order to expose the alpha radiation tracks for analysis, it involves an etching process, e.g. a chemical reaction between a liquid etchant and the CR39 polymer, at specific conditions (6N NaOH solution, at a temperature of 70°C)(2) . The formation of tracks on the surface of the CR-39 polymer is sensitive to the conditions of the etching process, such as temperature, etching time and the concentration of the etchant solution. After the etching process is concluded, the track's dimensions can be measured by optical means. The goal of this research was to achieve a good alpha track spectrometry in a nondestructive-research setting, with a simplify procedure and infrastructure requirements. In this work we will address two issues with this method:

1. When trying to optimize and facilitate alpha energy discrimination based on the measurement of the etched alpha tracks diameter, a limitation is encountered: alpha particles with different energies could have created the same track diameters, at the same etching time. The diameter of the track was found to be a nonlinear function of the alpha particle energy(3) , unless the etching duration was fitted for each energy(4) .
2. There is a tendency to use high-end equipment, high-zoom magnification, sophisticated algorithm or destructive methods (scanning penetration depth of the track after slicing the card in key positions) (5-8) .

2. Materials and Methods

Materials: The CR-39 detector (Radosys Co.) has a density of 1.32 g/cm3 , an area 100 mm2 and a thickness of 10 mm. The polymers were imaged by optical system "Radometer"-model DH110 by Radosys Co. It consisted of a B&W CCD camera a computer-controlled microscope, and sample stage. The ImageJ software(8) was used for image-analysis. To expose the detector polymers to a discrete alpha energy under normal incidence, a set of collimators was made using a plastic ABS 3D printer. For achieving the highest alpha energy exposure under normal incidence, a collimator made of aluminum foil was used, due to a limitation on the spatial resolution of the printer. In addition to the collimator, a 3-D printed holder was made to allow repeatable conditions of the CR-39 exposure to the 241Am source. It set the CR-39 in a constant position, in front of the source.

Methods:

Storage: The CR-39 detectors were maintained in a freezer at a temperature of -22°C before and after the etching and exposure stages in order to avoid environmental factors affecting the sensitivity of the detector polymers(10,11) .

Chemical treatment: The formation of tracks is very sensitive to etching conditions therefore, it is necessary first to determine the optimal solution concentration and heating temperature. Different etch procedures were recommended in the literature (2,12) . A 6.25 N NaOH solution at 70°C was used for various etching durations, then the detectors were immersed for 20 minutes in a 6.25 N acetic acid solution, washed with distilled water for additional 20 minutes and finally dried.

Bulk Etching Rate: The bulk etching rate, Vb [cm/h], was determined by measuring the difference between CR-39 mass before and after the etching process, eq.1

$$V_b = \frac{(M_{be} - M_{ae})}{2 \cdot A \cdot \rho \cdot t} \qquad (1)$$

Mbe and Mae are the CR-39 mass [g] before and after the etching process, respectively, A is the area of the CR-39 after the etching process [cm2], is its density [g/cm3] and t is the duration of the etching process [h].

Optics and Image Analysis: After etching the CR-39 polymers and the neutralization of the etching solution, the surface of the polymers was optically scanned with the Radometer system in transmission mode (polymer between light-source and camera). The CR-39 surface was divided by the Radometer software into nine regions of interest and each one was imaged and processed by ImageJ:

1. By utilizing a binary filter, the images were subjected to a gross threshold, in order to differentiate tracks from the background.
2. Various track parameters such as area, mean gray value, Minor and Major Diameters (respectively, smaller and larger track diameters) were extracted.
3. A circularity filter was applied on each track, with a threshold of 0.9 on the ratio between major and minor axes.
4. Different descriptive statistics were calculated on the remaining tracks.

These included mean and standard-deviation figures, histograms and others. This procedure been done to achieve a track parameters database of background and irradiated CR-39. The CR-39 cards were first studied for their background tracks parameters (Alpha tracks were separated from false tracks, presumably created by defects, scratches in the CR-39 polymer or background exposure from radon) (13)(15) . Then the tracks parameters had been analyzed for exposed CR-39 with discrete alpha energies after the background tracks had been subtracted.

Radioactive Source: To analyze a wide energy spectrum, a 241Am source with different collimator thicknesses was used to obtain different discrete energies. The energy spectrum of the incident particles was controlled by changing the distance between the source and the CR-39 detector. The energy of the alpha particle at the surface of the detector was calculated according to eq.2 and eq.3(16):

$$R_{air} = 0.322 E_{\alpha}^{\frac{3}{2}} \qquad (2)$$

$$E_R = \left[\frac{(R_{air} - d)}{0.322}\right]^{-\frac{2}{3}} \rightarrow d = R_{air} - 0.322 E_R^{\frac{3}{2}} \quad (3)$$

Rair is the travel distance of alpha particles in air [cm], Eα is the initial alpha energy (MeV), ER is the residual energy, and d is the air distance between the source and the detector-polymer surface [cm]. A good correlation been found between the alpha particle energy and the track diameter when an alpha particle strikes a CR-39 surface at an energy higher than 3 MeV and at an angle of 90° (13) . For this reason ~3 MeV was set as the lowest energy bound for collimator construction purposes. Table 1 specifies the calculated values of energetic attenuation for each collimator thickness.

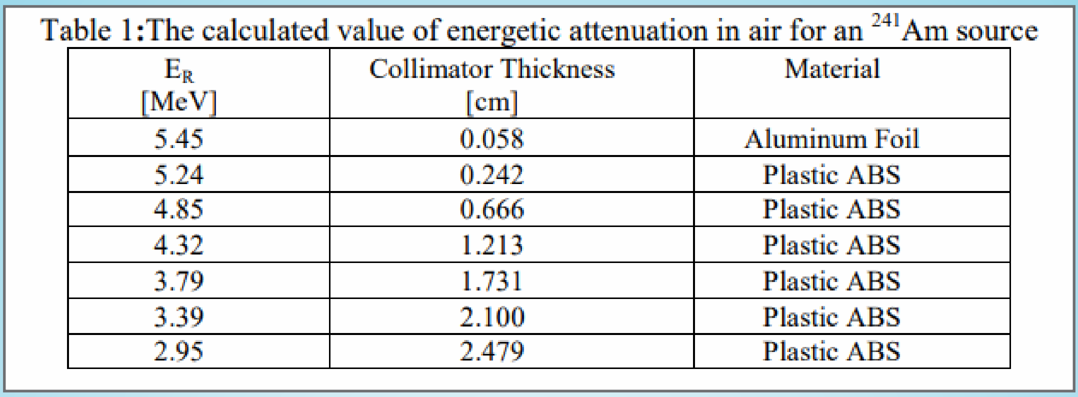

Table 1:The calculated value of energetic attenuation in air for an ^{241}Am source

E_R [MeV]	Collimator Thickness [cm]	Material
5.45	0.058	Aluminum Foil
5.24	0.242	Plastic ABS
4.85	0.666	Plastic ABS
4.32	1.213	Plastic ABS
3.79	1.731	Plastic ABS
3.39	2.100	Plastic ABS
2.95	2.479	Plastic ABS

3. Results and Ddiscussion: The bulk etching rate and the dimension of the false tracks been established by six unexposed, etched CR-39 cards. The average bulk etching rate, Vb, using the mass method, was found to be 1.84 μm/h. False tracks characteristics, area and value of mean gray tracks were measured using ImageJ. Their area dimensions and gray level were found to be lower than 82 μm2 and higher than 59, respectively, in accordance with published research(16) . Additionally, CR-39 cards were exposed to 241Am with different collimators and etched for six hours. More than 400 alpha tracks were obtained for each energy. The irradiated CR-39 resulted in a relatively low correlation (R2 =0.86) between the energy and the average track Minor or Major diameters. Also, the distribution was found to contain two peaks instead of one. This phenomenon was noticed especially in the higher energy range, where the tracks, measured by the microscope, were too small. To improve the resolution and correlation of the diameter distribution, a four-hour etching time was added to the irradiated CR-39, on top of the known protocol(2), there by exposing the polymers to a total of 10 hours in NaOH. Increasing the etching duration allowed the track dimensions to increase and thus compensate for the microscope's optical limitation. The results for the Minor and Major diameters, after the addition of four etching hours concluded with substantially improved correlation (R2 =0.98). Furthermore, only One counting peak of the diameter distribution was observed. To determine the optimal CR-39 etching time for calibration curve generation while avoiding etching accuracy variation in any specific bulk etch, it is required to find the bulk etch and time etch which will cause maximum compatibility between energy and track diameter. CR-39 detector polymer samples were therefore exposed to an 241Am source with different collimators, and were etched with new solution for several different durations, as shown in Table 2. The average bulk etching rate, Vb, was measured again using the mass method, and was found to be 2.07 μm/h.

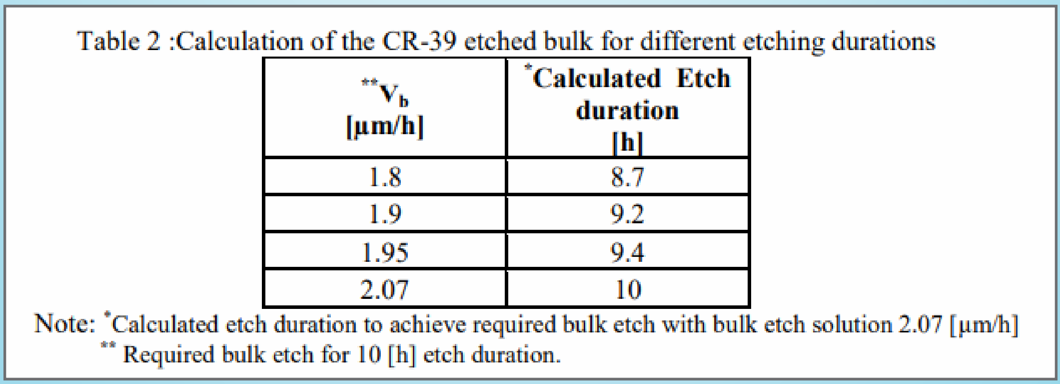

Table 2 :Calculation of the CR-39 etched bulk for different etching durations

$^{**}V_b$ [μm/h]	***Calculated Etch duration [h]**
1.8	8.7
1.9	9.2
1.95	9.4
2.07	10

Note: *Calculated etch duration to achieve required bulk etch with bulk etch solution 2.07 [μm/h]
** Required bulk etch for 10 [h] etch duration.

Figure 1 shows the experimental curves for the average Major and Minor track diameters, as a function of energy and CR-39 etched bulk. High correlation was observed for the Major and Minor diameters, with correlation coefficients in the range of 0.93 to 0.98 and 0.93 to 0.99, respectively.

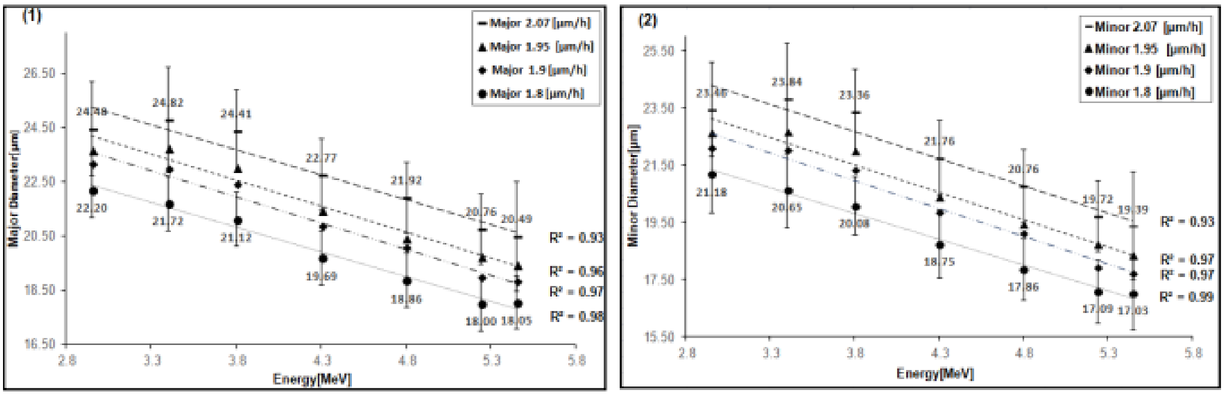

Figure 1: The average Major and Minor track diameters, as a function of energy and CR-39 etched bulk.

The correlation coefficient decreased as the CR-39 etched bulk (Vb, Table 2) increased, a result of an over etching of the tracks in the lower energy range causing the formation of a "Bragg curve"(3) . To determine the optimal calibration curve, several parameters were examined. These included the peak of the track diameter distribution and the correlation between energy to diameter. An optimal calibration curve was determined for energy discrimination, the Major diameter curve for 10 [h] etch with 1.8 [µm/h] bulk etch rate. Data was fitted by a linear approximation, which enabled the alpha particle energy to be calculated, according to eq 4.

$$\text{Energy[MeV]} = -\left(\frac{\text{D\_Major}[\mu\text{m}] - 29.43}{2.16}\right) \qquad (4)$$

To determine the degree of energetic discrimination according to the calibration curve, the uncertainty of the track diameter needed to be estimated. The total uncertainty consisted of arbitrary and systematic uncertainty. The arbitrary uncertainty included the measurement resolution and the standard deviation of the Major diameter distribution. The systematic uncertainty included factors involved in the evaluation of the measurement system calibration coefficient. Table 3 shows the results of the total uncertainty for each alpha particle energy in the range of 2.95 - 5.45 MeV. To test the method of spectral identification by the calibration curve, several alpha emitters were examined without collimators, three within the calibration curve range and two outside it.The alpha source emitters were: 241Am (5.486 MeV), 222Rn (5.489 MeV), 222Rn Progeny: 218Po (6 MeV), 214Po (7.7 MeV) and 238U (4.2MeV). Two CR-39 cards were exposed to each of the alpha sources. Table 3 shows the results for the energy identification of various alpha sources. The energy identification of 241Am, 222Rn and 238U sources were conducted according to the method developed, and a standard deviation of up to 3.6% was obtained. When the CR-39 cards were simultaneously exposed to several energies from 218Po and 214Po sources, a standard deviation of up to 16.2% was observed, which was the result of an overlap in the distribution of the two energies.

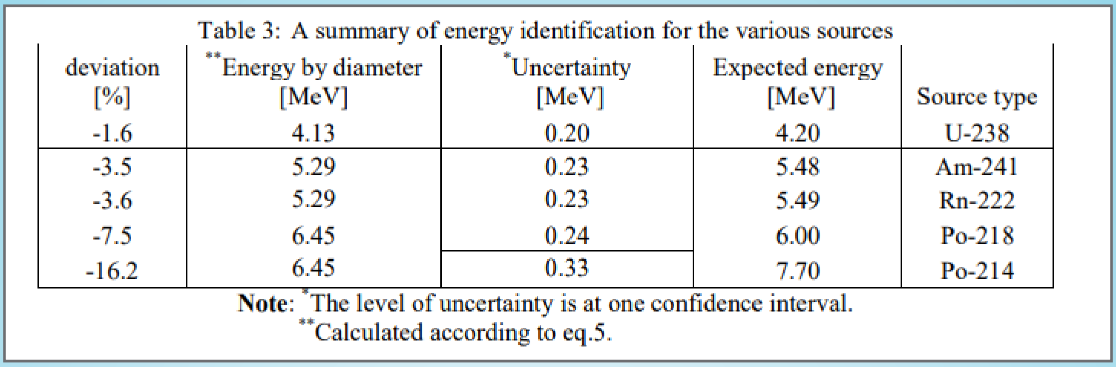

Table 3: A summary of energy identification for the various sources

deviation [%]	**Energy by diameter [MeV]	*Uncertainty [MeV]	Expected energy [MeV]	Source type
-1.6	4.13	0.20	4.20	U-238
-3.5	5.29	0.23	5.48	Am-241
-3.6	5.29	0.23	5.49	Rn-222
-7.5	6.45	0.24	6.00	Po-218
-16.2	6.45	0.33	7.70	Po-214

Note: *The level of uncertainty is at one confidence interval.
**Calculated according to eq.5.

4. Conclusions: A spectral discrimination method was developed using a device with low optical capabilities, without the development of a complex algorithm or method. Several track characteristics filters were used after the CR-39 was irradiated and been etched: circularity>0.9, track area>82 μm2 and a mean gray level<59.

It should be noticed, however, that the method is applicable only to the Radosys CR-39 card. The use of CR-39 cards from other manufacturers requires rechecking of the CR-39 etched bulk and the characteristics filters values. It is possible that a difference in the production process could influence the track etching rate and the CR-39 etched bulk. The energy of the alpha emitter was determined using the peak value of the Major track diameter distribution and the curve calibration equation. The method, developed in this study,

makes it possible to detect energies of mono-energetic alpha emitters, in the energy range of 2.95 MeV to 5.45 MeV, with a resolution of 0.11 to 0.23 MeV, respectively. The detection of a non mono-energetic source is very important, so options for improving the developed method should be further investigated.

The Integration of Blender 3D Mesh Modeling and FLUKA Flair through Voxelization

Y. Korotinsky, L. Epstein, and M. Brandis

Background: Monte Carlo (MC) codes are widely employed in scientific and engineering applications, covering areas from financial analysis to particle transport simulations. Among the various MC software available, FLUKA is particularly prominent for particle transport applications. A major advantage of FLUKA is its capability to model and visualize intricate geometries via the Flair GUI. Typically, the geometric input depends on Boolean combinations of basic shapes. While sufficient for most applications, these techniques may present challenges when attempting to replicate more complex structures encountered in advanced engineering designs, medical equipment, and computations for radiation protection.

Purpose: This research explores the challenge of representing complex geometries in FLUKA using the produced geometric output of the open source 3D modeling suite - Blender. The produced output can then be converted to the FLUKA-Flair framework by transforming polygonal mesh models into a grid of volumetric pixels (voxels).

Methods: We devised a custom MATLAB script tailored to convert Blender's geometric outputs, particularly those in the .OBJ file format (3D polygonal meshes outlined in Cartesian coordinates), into a voxel-based data format. This method was also developed to effectively convert models comprising multiple materials.

The voxelized geometry was subsequently processed by a predefined FLUKA routine to be compatible with the Flair voxel import format. To ensure precise comparisons, Blender was used to generate 3D models, while Flair was used to create geometric replicas through traditional Boolean operations. The precision of the method was evaluated by comparing the voxelized geometries with those modeled internally in Flair, focusing on fluence and dose rate distributions. Furthermore, we evaluated the preprocessing and execution times of the geometries, as well as the volumetric sizes of the structures.

Results: The discrepancies in volume between Flair models and Blender mesh models did not exceed 0.6%. Similarly, the variance in CPU computation time was within 5%, with Flair-generated geometries exhibiting slightly reduced times. An analysis of the fluence and dose rate distributions indicated no substantial differences between the two geometric configurations.

Conclusions: This research introduced and validated a technique to convert complex 3D polygonal mesh models, created using Blender, into voxel geometries suitable for integration within FLUKA. This enables the conversion from various geometry files, including engineering softwares. Additionally, the study showcased the precise conversion and importation of multimaterial models.

Electrodeposition and the problematic use of H2SO4 and HNO3, the traditional ingredients of electrolyte solutions

Raphael Gonen, Shimon Tsroya

Nuclear Research Center Negev, Beer-Sheva, Israel, 84190

In this research, we focused on some of the traditional ingredients of the electrolyte solutions of the electrodeposition (ED) process. We suspected that H2SO4 and HNO3 contribute to accelerated corrosion of metal disks (stainless steel and copper) while the process is done. The corrosion formed looks like a black coated film situated on the surface of the cathode disk. The film that is formed, was examined as well to verify whether when exists, it decreases the metal deposits onto the metal disc cathodes.

H2SO4 and HNO3 were found to be the causative ingredients to form the corrosion phenomena that took place during the ED process. The amount of corrosion formed was found to be related to the decreasing amount of the deposited metals.

As a conclusion, it is advised not to include these ingredients in the electrolyte solutions, as the have influence on ED yield. The corrosion formed may have another disadvantage by causing bad resolutions of alpha emitting radionuclides (yet to be proved).

Experimental study of Critical Heat Flux temperature due to a rapid heating process at constant pressure

Doron Biton[1,2], **Gennady Ziskind**[2], **Tali Bar-Kohany**[1,3]

1 Department of Mechanical Engineering, NRCN, Beer-Sheva, 8419001, Israel
2 Department of Mechanical Engineering, Ben-Gurion University of the Negev, Beer-Sheva, 84105, Israel
3 School of Mechanical Engineering, Tel Aviv University, Tel Aviv, 6997801, Israel

This study investigates the impact of rapid heating on Critical Heat Flux (CHF) and the Onset of Nucleate Boiling (ONB) in dielectric fluids, at rapid heating rates ranging from 0.5×10^6 to 18.5×10^6 K/s under atmospheric pressure. Utilizing a micro-heater, experiments were conducted with and without pretreatments, and at subcooling levels between 15 °C and 35 °C. Despite the prevalent use of dielectric fluids in electronic cooling applications, there is a notable scarcity of literature addressing their ONB and no CHF behaviors under rapid heating conditions. This research expands the existing data for ONB in HFE-7100 and introduces new findings for HFE-7000, revealing superheating levels of 10 °C and 21 °C, respectively. A novel, non-visual criterion for CHF detection is proposed and validated through high-speed photography. Additionally, the study examines the influence of heating element size on CHF mechanisms and values, identifying and explaining a discontinuity in CHF temperature as a function of heating rate.

These insights contribute to a deeper understanding of rapid boiling dynamics in dielectric fluids, which is crucial for advancing their thermal management technologies.

Poster Session 2

Fission Tracks Pattern Analysis and Properties Reconstruction: Advancing Nuclear Forensics using Classic Image Processing Algorithms

Babayew Rami, Yaacov Yehuda-Zada, Galit Bar, Elgad Noam, Last Mark, Jan Lorincik, Itzhak Orion, Shay Dadon, Aryeh Weiss, Galit Katarivas Levy, Halevy Itzhak

Fission Track Analysis (FTA) is a crucial technique in nuclear forensics, enabling the identification of nuclear materials through the examination of fission tracks in Solid-State Nuclear Track Detectors (SSNTDs). This study enhances FTA by integrating advanced image processing techniques with both real and synthetic fission track data, improving detection, classification, and property reconstruction. Real data provides physical insights, while synthetic data offers controlled environments for testing algorithm performance and detector response.

Monte Carlo simulations using GEANT4 (v10.6) with the “QGSP_BERT_HP” physics library were employed to model fission product trajectories. Additionally, we developed the “FTA Trainer” application to generate synthetic fission track clusters on real SSNTD background images, enabling scalable and configurable data generation (36 pixels = 1 μm). These datasets were used to develop and validate image processing algorithms for pattern analysis and property reconstruction of fission track clusters.

Our methodology includes:

1. **Fission Site Calculation** – Hough transform-based edge detection to identify track lines and their interception points, estimating potential fission site locations.
2. **Fission Track Recognition & Length Analysis** – Classical image processing techniques (filtering, edge detection, morphology, histogram equalization, thresholding, and feature extraction) for precise track identification.
3. **Fission Properties Reconstruction** – Geometric analysis of light and heavy fission product track lengths for material characterization.

Results demonstrate successful fission product pattern analysis and image-based evaluation of generated U-235 enrichment clusters (FTA Trainer 2.4). Our findings highlight:

Fission Tracks Pattern Reconstruction of simulated and real star are depicted in Fig 1 and Fig 2.

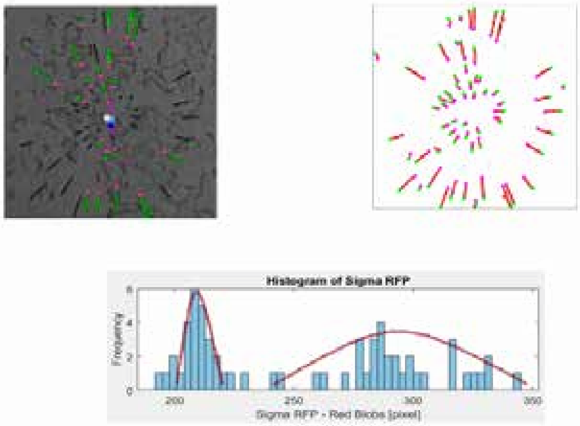

Fig. 1: Fission Tracks Pattern Reconstruction of **simulated** star.

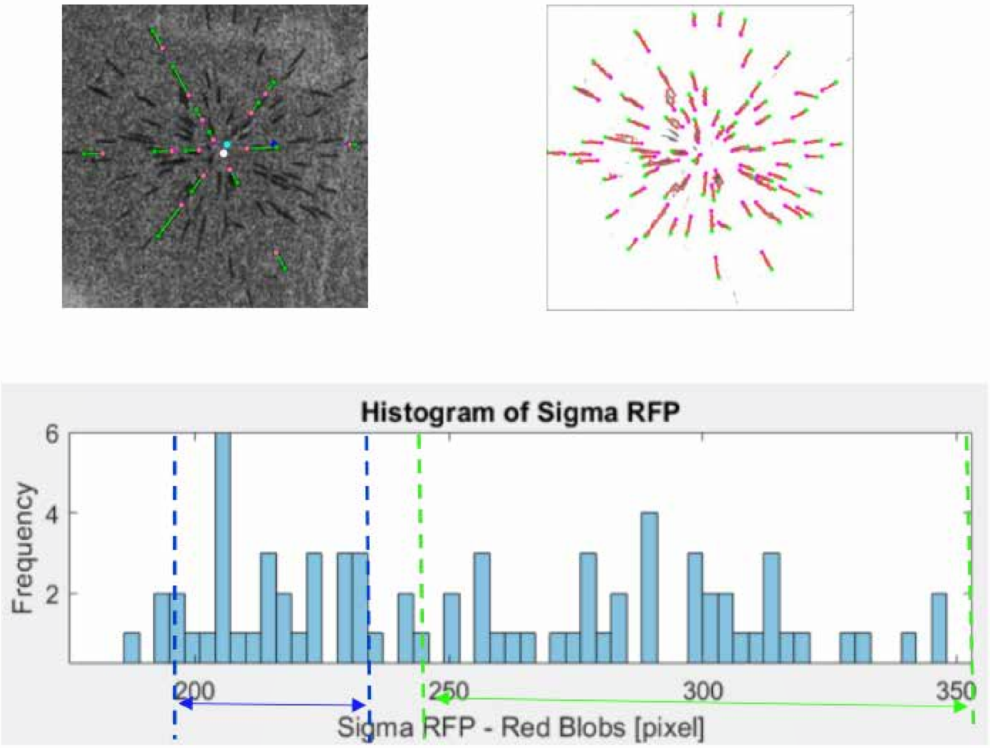

Fig. 2: Fission Tracks Pattern Reconstruction of **Real** star.

- The track path histogram varies depending on the SSNTD setup, reflecting the influence of experimental conditions such as detector material and exposure time.
- Overlapping or highly dense fission track clusters pose a challenge, as they reduce the accuracy of individual track identification, requiring advanced detection techniques.
- Synthetic data enables controlled testing of algorithm performance, allowing us to refine detection and classification methods before applying them to real nuclear forensic samples.

Analysis of real fission track data (IAEA314 'Soreq' Reactor) validated our automated processing approach, revealing challenges such as noise, background artifacts, and overlapping tracks that necessitate advanced filtering. Despite limited statistics, our methodology proved effective for fission property reconstruction.

Future work will focus on integrating an Aerogel Spacer into the experimental setup to enhance statistical significance. Current GEANT4 simulations of aerogel-coated SSNTDs will be followed by experimental validation at the Soreq Nuclear Reactor.

A Combined Gamma Spectrometry and Proportional Counting Method for Sr-90 Quantification in a Mixed Sample: An ALMERA Proficiency Test Case Study

Tamar Avraham, Mor Ben-Lulu, Dani Vaknin, Sagi Nissim, Natanel Chichportich, Zohar Yungrais, Getaneh Abebe, Ofer Aviv and Michal Brandis

The Analytical Laboratories for the Measurement of Environmental Radioactivity (ALMERA), supported by the IAEA, is a global network designed to evaluate and enhance laboratory capabilities in environmental radioactivity measurements. To achieve this, the IAEA organizes annual proficiency tests, in which well-characterized reference materials with unknown radionuclide activities are provided and analyzed by the participating laboratories.

As part of the 2024 ALMERA proficiency test exercise, a filter sample containing Sr-90 and Cs-134 with unknown activities were analyzed. As a beta-gamma emitter- Cs-134 can be accurately quantified using high-purity germanium (HPGe) gamma spectrometry; however, Sr-90, a pure beta emitter, could not be detected by this method. Therefore, alternative or complementary detection methods are required to achieve accurate activity determination of Sr-90.

First, HPGe gamma spectrometry was used to determine the activity of Cs-134. Then, proportional counting using the LB4200 measurement system was employed to determine the total beta activity in the filter. By subtracting the gamma spectrometryderived activity of Cs-134 from the total beta activity measured, the activity of Sr-90 was determined. In order to further validate the results obtained, additional measurements were conducted using liquid scintillation counting with Quantulus 6220, determining activities of both radionuclides separately.

This work presents a systematic approach for the accurate determination of pure beta or alpha emitters in mixed radionuclide samples, demonstrating the effectiveness of complementary detection techniques in enhancing measurement reliability and supporting radioactivity assessments in complex matrices.

Manual Correction of Gamma Contributions in Liquid Scintillation Counting: A Case Study with Quantulus GCT 6220

Natanel Chichportich, Sagi Nissim, Mor Ben-Lulu, Ofer Aviv and Michal Brandis

The Quantulus GCT 6220 is a liquid scintillation counter known for its high efficiency in detecting low-level alpha and beta radiation. The system is equipped with an optically transparent bismuth germanium oxide (BGO) scintillating crystal, installed between the sample and PMT faces. The BGO, which acts both as a light guide and a guard detector, enables subtraction of background events by rejecting BGO pulses and any simultaneous sample pulses. While effective in reducing external gamma contributions, this design can systematically underestimate activity for radionuclides undergoing beta or alpha decays accompanied by gamma emissions, such as Co-60.

Herein, a manual correction method was proposed to address the systematic underestimation of radionuclides whose decay is accompanied by a coincident gamma emission. This approach accounted for gamma contributions detected by the BGO guard, by integrating them into the total count rate associated with alpha or beta emissions recorded by the liquid scintillation cocktail. By post-processing the measurement data of nuclides of interest (Co-60, Am-241 and Na-22) using the developed approach, the determined activities deviated by less than 5% from the expected values. The developed method was also applied to a mixed radionuclide samples containing both pure beta emitters (H-3/C-14) and a beta-gamma emitter (Co-60). The results demonstrated deviations within 5% of the expected activities, confirming the reliability of the proposed correction strategy.

Finally, this method provides a framework for accurately quantifying total alpha and beta decays while effectively accounting for gamma contributions, thereby expanding the system's ability to accurately measure samples beyond pure beta and alpha emitters only.

PROCORAD Proficiency Tests: A 10-Year Review of Performance in Gamma-Emitter Detection and Quantification

Zohar Yungrais, Mor Ben-Lulu, Tamar Avraham, Maya Veinger, Revital Sasson, Sagi Nissim, Getaneh Abebe, Ofer Aviv and Michal Brandis

The Gamma Spectrometry Laboratory is responsible for gamma-emitters detection and quantification tests in urine samples of radiation workers, using high-purity germanium detectors. As part of its quality assurance efforts and compliance with the ISO 17025 standard, the laboratory has participated in international proficiency tests organized by PROCORAD (an organization dedicated to improving radiotoxicological analysis and measurement standards) for approximately 15 years. These annual tests involve around 40 laboratories, with each laboratory evaluated based on defined performance criteria.

This work summarizes the performance of the gamma spectrometry Laboratory in gamma-emitter measurements and analysis across 11 proficiency tests conducted between 2013 and 2023. It incorporates findings from official PROCORAD summary reports and the laboratory's internal evaluations. Identified deviations during the tests were analyzed, and key strategies were developed to ensure continued success in future assessments.

This poster demonstrates that the gamma spectrometry Laboratory achieved high success rates in the majority of tests, consistently excelling in radionuclide identification and activity concentration accuracy. These outcomes underscore the reliability of the laboratory's methods for the preparation, measurement, and analysis of urine samples for gamma emitters.

The Effect of Matrix Composition on Solidification Rate and Heat Generation of Geopolymers

Savion Braunstein*, Gali Orian, Shani Maman, Nitzan Shtreimer Kandiyote,
Yosef Aharon, Gabriela Bar-Nes, Hadas Raveh-Amit

** Corresponding Author, E-mail: savionb@post.bgu.ac.il*

Introduction and Research Goals: Alkali-activated aluminosilicate cements, also known as geopolymers, have been applied as immobilization matrices for radioactive waste, e.g. the SIAL® matrix used for sludges, resins, and other organic liquids. The preparation of waste-contained geopolymers initiates a multi-phase geopolymerization process. This process is governed by exothermic reactions, leading to solidification and encapsulation of radionuclides. Geopolymerization might be affected by the chemical composition of the waste and the binding matrix. In this work, we study the impact of the Si/Al ratio of metakaolin-based geopolymers mixed with a simulant aqueous waste solution (based mainly on sodium nitrate) on the geopolymerization process. The solidification rates and the heat generation profiles were examined for freshly prepared pastes with two different formulations.

Results and Conclusions: Metakaolin-based geopolymers with different Si/Al ratios (1.3 and 1.7) were prepared by mixing a simulant aqueous waste solution with sodium hydroxide as an alkali activator, and different amounts of sodium silicate. Solidification rates and heat production were studied by performing the Vicat needle test and isothermal calorimetry on the fresh pastes, respectively. It was found that increasing the Si/Al ratio of the geopolymers slowed their solidification, demonstrated by longer initial times of setting, i.e. 12.7 ± 1.0 vs. 3.3 ± 0.4 hours for geopolymers with Si/Al ratios of 1.7 and 1.3, respectively.

Slower solidification rates correlated with lower accumulated heat generation and an extended heat production phase, manifested by a heat production peak after ~8 hours and ~3 hours after the preparation of geopolymers with Si/Al ratios of 1.7 and 1.3, respectively (Figure 1). This outcome may be due to the differences between the silica and alumina dissolution rates. 1 A numerical thermal simulation based on finite elements was developed to explore the dependency of the evolved temperatures on several parameters, like the material thermal properties and the environmental conditions. The experimental results of the heat production profiles are utilized in the simulation to predict the evolved temperatures of the pastes under realistic operational conditions. Next, we plan to study the impact of the simulant waste composition by assessing the effect of different formulations on the geopolymerization of fresh grouts.

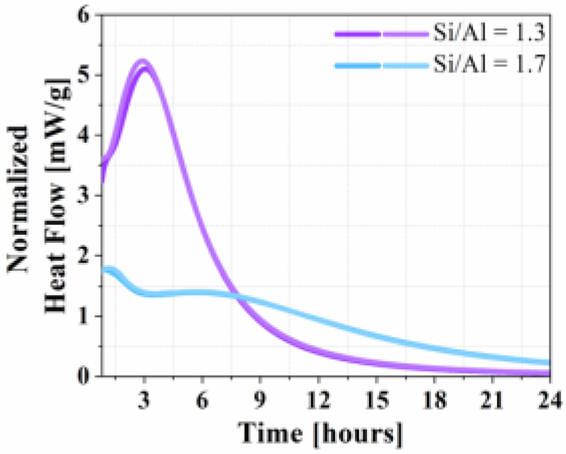

Figure 1. Normalized heat production [mW/g] over time [hours] of geopolymers with Si/Al ratios of 1.3 and 1.7, respectively.

Utilization of Deep Learning for Star Segmentation and Classification using Semi-Automated Adaptive Threshold methodology

N. Elgad[1,2*], R. Babayew[1,2], M. Last[3], Y. Yehuda-Zada[1,2], J. Lorincik[4], I. Orion[2], E. Gilad[2], A. Weiss[5], G. Katarivas Levy[6], and I. Halevy[2]

1 *Physics Department, Nuclear Research Center Negev, Beer-Sheva, Israel*
2 *Unit of Nuclear Engineering, Faculty of Engineering Sciences, Ben Gurion University of the Negev, Israel*
3 *Department of Software and Information Systems Engineering, Faculty of Engineering Sciences, Ben Gurion University of the Negev, Israel*
4 *Nuclear Fuel Cycle Department, Research Centre Řež, Hlavní 130, Řež 250 68, Husinec, Czech Republic*
5 *Faculty of Engineering, Bar Ilan University, Ramat Gan P.O.B. 90000 5290002 Israel*
6 *Department of Biomedical Engineering, Faculty of Engineering Sciences Ben-Gurion University of the Negev, Beer-Sheva, Israel*
**e-mail: n.elgad@gmail.com*

This study presents an innovative approach for detecting and classifying star-shaped patterns in microscopic images, leveraging advanced deep learning techniques of segmentation and classification [1] for fission track analysis mission in the domain of nuclear forensics. The U-Net model, a fully convolutional neural network, employed to segment various star-like patterns in both single-class and multi-class settings (figure 1 [1]). In order to train the model, artificial star shapes were used, among other data, generated through a specialized simulation tool which was developed by our research team [2].

The model which conducted with a 5-fold cross validation analysis was built for small sized stars, less than 60μm, and under 200 pixels with less than 10 leaves and without black center. This model achieved a total area of 0.84 under the ROC curve. In addition, a model for bigger and richer stars was built that achieved a total area of 0.90 under the ROC curve. Also, preliminary models were built which can differentiate between roses of different shapes and sizes at the same time.

Furthermore, this study also summarizes focused research conducted to determine thresholds for background noise filtering and to improve identification and established a new methodology for semi-automated adaptive threshold setting.

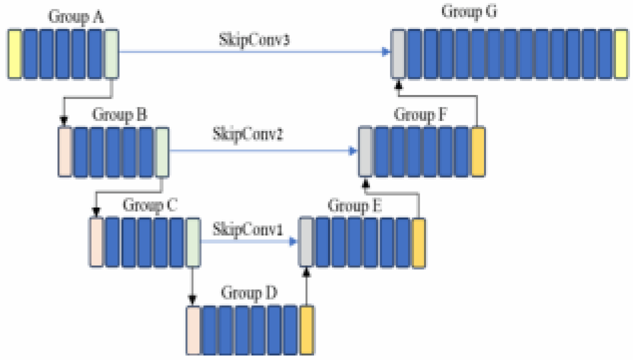

Figure 1: Design and implementation of a U-Net architecture for segmentation and classification.

MAXIMA-II - A versatile Detection System for Trace-Level Radiation Analysis

Sagi Nissim[1,2], **Ofer Aviv**[1], **Michal Brandis**[1], **Erez Gilad**[2]

1 Soreq Nuclear Research Centre,
2 Ben- Gurion University of the Negev

MAXIMA-II is a radiation detection system under development at Soreq Nuclear Research Center in collaboration with the unit of nuclear engineering at Ben-Gurion University. It integrates a high-purity germanium (HPGe) used for high-resolution gamma-ray spectrometry and a liquid scintillator (LS) used for counting alpha and beta particles at large efficiency. The system combines a coincidence detection technique with machine learning-based pulse shape discrimination (ML-PSD), enabling simultaneous investigation of alpha, beta, and gamma decay products while effectively rejecting background events.

Maxima II applications include detecting trace-level radioactive isotopes for various fields (e.g., nuclear forensics and environmental monitoring), radiation protection and accurate evaluation of nuclear decay data.

Preliminary results demonstrate successful alpha-beta separation and noise reduction using a dual-PMT configuration. We will present the system design and initial findings, showcasing MAXIMA-II's potential as a compact and efficient tool for complex sample analysis.

Disposal of Nuclear Waste in Space Using Electromagnetic Accelerator Launchers

Perets Y. and Bahiri S.

Background: The nuclear power plant has taken an important place in the global effort to supply clean, low-carbon and reliable energy. By December 2021, there were 437 actives NPPs worldwide generating about 390 GW(e), which is approximately 10% of global world's electricity [1]. The production of electrical energy through nuclear power plants generates byproducts of various radioactive wastes. Throughout the lifecycle of NPP - operation, maintenance and decommissioning, various types of radioactive waste are generated, requiring safe disposal to prevent the possibility of exposure to both the environment and humans. According to the IAEA [2], around 90% of the global waste volume is considered a low level of radioactivity (LLW) and limited half-life time. The other 10% is considered intermediate level waste (ILW) and high-level waste (HLW) and comes mainly from spent fuel reprocessing, which is highly radioactive, and its half-life can reach to tens to thousands of years. Although their small volume, ILW and HLW radioactivity constitute more than 95% of the total radioactivity inventory. While low- and intermediate-level waste is treated and stored at the power reactor site or designated site, high-level waste is stored for a prolonged period for cooling and decay, first in wet storage for a few years and then in dry storage and eventually goes to disposal. Many countries, such as Finland, France, Japan, UK, Russia, Spain, Sweden, Switzerland, USA and many others have chosen the deep geological disposal strategy as the preferred alternative. The commonly proposed concept for deep geological disposal is an underground mined repository (e.g. a deep tunnel or cave) and deep boreholes consist of drilling holes hundreds to thousands of meters deep in the ground.

Most of these countries are in the early stages of HLW geological disposal programs, which are expected to be completed from 2035 to 2060. Finland's Onkalo Repository is the only one in the commissioning stage. The lack of an existing and significant solution for the existence of HLW and spent fuel inventory and public acceptance of deep geological disposal techniques have resulted in the need to search for other solutions. From the late 70's to the 90's, the disposal of radioactive waste in space was studied by NASA. The main idea is to launch the HLW into one of space orbit destinations, including solar system escape, using a rocket or space shuttle.

The main drawbacks of the rocket and space shuttle concepts were payload limitations imposed by physics, with payloads often being less than 4% of the rocket's total mass, rockets must be really big to lower the cost per kg which limits launch availability, a large number of rockets required to launch each year to handle existing and future spent fuel and the low availability of launching devices, making it neither effective nor economically feasible. Also, there was a notable proportion of failures in rocket launches into space, meaning a high potential risk in launch entails significant safety hazards to the environment and civilians. We will discuss an innovative approach for launching capsules filled with HLW from NPP spent nuclear fuel, using an electromagnetic accelerator-based kinetic SSTO (SingleStage-to-Orbit) launcher for permanent disposal in space.

Methods: The methods of this work focus on the design and implementation of a space disposal system for high-level waste (HLW) and spent nuclear fuel (SNF). The system uses a kinetic, electromagnetic accelerator-based SSTO launcher to eject capsules containing HLW onto solar system escape trajectories, ensuring permanent waste isolation.

The capsule design incorporates an aerodynamic Sears-Haack body to minimize drag, while the structure includes a two-layer shield for radiation protection. An inner capsule structure, incorporating both the capsule's framework and gamma shielding, maintains radiation levels below 20 mSv/hr within the launch facility, while the outer shield ensures that radiation exposure remains below 2 mSv/hr during transportation. This outer shield will be removed upon the capsule's arrival at the launch facility. The mechanical containment design serves as the primary safeguard against the release of nuclear waste, ensuring structural integrity during transport and providing protection in the event of potential impacts during launch.

Results: A preliminary calculation was made to estimate the capsule's internal shielding. The capsule shield thickness was calculated for a variety of materials, suitable for radiation shielding and compatible with electromagnetic accelerator (non-ferromagnetic with low magnetic permeability close to 1). NEA (2023) benchmark [3] conducted a comparative study on dose rate calculations for typical uranium oxide (UOX), containing 469.2 kgHM and mixed oxide (MOX) spent FAs containing 454 kgHM, from pressurized water reactor (PWR). According to the NEA Benchmarks results, the gamma dose rate [Sv/h] at a 1m distance from the midpoint of a PWR fuel assembly, 30 years after discharge, was found to be 5.8 Sv/h and 11 Sv/h for the UOX and MOX fuels, respectively. After 30 years of cooling time, the release of gamma is dominated by the longer-lived isotopes, particularly 137Cs (661.657 keV), which continues to be the primary contributor.

Typically accounts for over 80% of the total gamma release in the first few decades after discharge. Additional isotopes such as 54Eu (68.17 keV and 100.88 keV) and 241Am (59.54 keV) also contribute to the gamma release, but their contributions are generally smaller compared to 137Cs.

For preliminary approximating to estimate the capsule's internal shielding thickness, we use the exponential attenuation equation with a buildup factor. Considering 137Cs (661.657 keV) as the main contributor to gamma radiation, we abstract the mass attenuation coefficient and the buildup factor.

The results show that materials like lead, tantalum, and tungsten, which have higher density, require the thinnest wall thickness for effective shielding, about 4.8 to 8.1 cm. This trend is suitable due to the model being based on calculations from a one-point radiation source. However, it is important to note that in a more realistic 3D model with multiple photon sources, based on industry standards such as the MCNP transport code, the material with the thinnest shielding wall does not necessarily correspond to the lowest capsule mass.

Discussion and conclusions: The optimal design of the waste capsule is crucial for achieving an ideal payload-torocket ratio that is well-suited for a Single-Stage-to-Orbit (SSTO) launch system. Initial calculations indicate that the most efficient payload mass ratio for the proposed system ranges between 8% and 17%. This range can ensure that the capsule design aligns with the efficiency requirements of the SSTO launcher. Further optimization of the capsule's structural thickness and material composition is required to improve the payload ratio by using a more realistic 3D model. Additionally, factors such as heat resistance, aerodynamic properties, and overall mass distribution should also be considered.

Implementation of the DXT-RAD Dosimeter in the External Dosimetry Lab at SNRC

Yaniv Levy, Netanel Chichportich, Nir Pour and Gal Amit

Background: The External Dosimetry Lab (EDL) at Soreq Nuclear Research Center (SNRC) is in the process of upgrading its extremity dosimetry capabilities by implementing the advanced Thermo Fisher Scientific DXT-RAD Thermoluminescent dosimeters (TLD). This new technology offers enhanced sensitivity to beta and lowenergy gamma radiation, along with improved dosimeter durability. Most notably, it is expected to significantly improve the measurements precision by implementing the built-in Element Correction Coefficient (ECC) capability.

Methods: The DXT-RAD dosimeters, manufactured by Thermo Fisher Scientific and implemented within the advanced Harshaw TLD 8800plus system, are being validated for use in extremity dosimetry through a series of controlled irradiation and performance evaluations.

To assess the effects of mixed radiation fields and to ensure compliance with ANSI/HPS N13.11, the dosimeters were exposed to known radiation sources (137Cs, M150 (X-ray), 90Sr and 85Kr) at an accredited calibration laboratory (PNNL).

Additionally, accuracy and linearity tests are being conducted in collaboration with the SNRC's SSDL facility, following the performance requirements outlined in IEC 62387. These tests ensure that the dosimeters meet precision, accuracy and reliability standards for extremity dosimetry. Currently, final validation is underway to achieve full compliance with IEC 62387.

Results: The DXT-RAD dosimeters demonstrated superior performance compared to the 3500 system. As an example, by using the build-in ECC capability the precision improves from ±30% to ±2% for the lab relevant doses (0.5 mSv to 500 mSv). Moreover, the enclosed TLD element design enhanced durability and minimizes organic contamination. The dosimeters showed excellent sensitivity to beta, low and highphoton energy radiation, meeting the acceptance criteria by ANSI/N13.11 (Table 1)

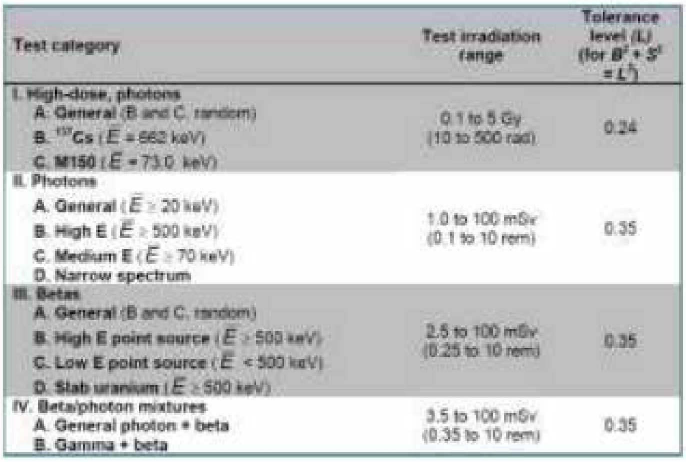

Test category	Test irradiation range	Tolerance level (L) (for $B^2 + S^2 = L^2$)
I. High-dose, photons A. General (B and C, random) B. ^{137}Cs ($\bar{E}$ = 662 keV) C. M150 ($\bar{E}$ = 73.0 keV)	0.1 to 5 Gy (10 to 500 rad)	0.24
II. Photons A. General ($\bar{E}$ ≥ 20 keV) B. High E ($\bar{E}$ ≥ 500 keV) C. Medium E ($\bar{E}$ ≥ 70 keV) D. Narrow spectrum	1.0 to 100 mSv (0.1 to 10 rem)	0.35
III. Betas A. General (B and C, random) B. High E point source ($\bar{E}$ ≥ 500 keV) C. Low E point source ($\bar{E}$ < 500 keV) D. Slab uranium ($\bar{E}$ ≥ 500 keV)	2.5 to 100 mSv (0.25 to 10 rem)	0.35
IV. Beta/photon mixtures A. General photon + beta B. Gamma + beta	3.5 to 100 mSv (0.35 to 10 rem)	0.35

Table 1: ANSI/HPS N13.11 acceptance criteria

Discussion and Conclusions: While the use of the DXT-RAD dosimeters at SNRC EDL will improve extremity dosimetry for all radiation workers in Israel, its implementation is dependent on the successful completion of the ongoing validation process. This advancement will ensure compliance with international standards such as ISO/IEC 17025 and establish a robust framework for accurate radiation monitoring, particularly for personnel exposed to beta and photon radiation.

The Plasma Window for Enhanced Particle Beam Transmission from Vacuum to Atmosphere

Ophir Ruimi
HUJI & HIM/JGU

Neutrons play a dominant role in the stellar nucleosynthesis of heavy elements. We review a scheme for the experimental determinations of neutron-induced reaction cross sections using a high-intensity neutron source based on the 18O(p,n)18F reaction with an 18O-water target at SARAF's upcoming Phase II. The quasi-Maxwellian neutron spectrum with effective thermal energy kT ≈ 5 keV, characteristic of the target (p,n) yield at proton energy Ep ≈ 2.6 MeV close to its neutron threshold, is well suited for laboratory measurements of MACS of neutron-capture reactions, based on activation of targets of astrophysical interest along the s-process path. 18O-water's vapour pressure requires a separation in between the accelerator vacuum and the target chamber. The highintensity proton beam (in the mA range) of SARAF is incompatible with a solid window in the beam's path. Our suggested solution is the use of a Plasma Window, which is a device that utilizes ionized gas as an interface between vacuum and atmosphere, and is useful for a plethora of applications in science, engineering and medicine. The high power dissipation (few kW) at the target is expected to result in one of the most intense sources of neutrons available at stellar-like energies. Preliminary results concerning proton beam energy loss and heat deposition profiles for target characteristics and design, a new fullscale 3D CAD model of the Plasma Window (as well as its operation principles) and the planned experimental scheme at SARAF, are reviewed. Moreover, work includes a feasibility study for the use of a plasma window for the Gamma Factory, a proposed high energy (up to 400 MeV) photon source at CERN.

Comparison Between Semi-Insulating GaAs Alpha Radiation Detector with Schottky Anode Contact and P+ Anode Contact Layer Grown by MOCVD

O. Sabag[1,2,3], E. Evenstein[1], G. Atar[1], M. Bin-Nun[1], M.Alefe[1], D. Memram[4], R. Tamari[4], S. Primo[1], S. Zoran[1], L. Hovalshvili[1], D. Cohen-Elias[1,4] and T. Lewi[2,3]

1 Soreq Nuclear Research Center
2 Faculty of Engineering, Bar-Ilan University
3 Institute of Nanotechnology and Advanced Materials, Bar-Ilan University
4 The Israeli Center for Advanced Photonics

Gallium Arsenide (GaAs) is a promising candidate for the absorber layer in particle detectors. The advantages of GaAs-based particle detectors include radiation hardness, a short response time due to high charge carrier mobility, and low dark current resulting from its large bandgap [1-3].

Detectors based on semi-insulating (SI) GaAs substrates are typically fabricated with an N-type Ohmic contact for the cathode, while a Schottky contact is commonly used on the anode side [1-5]. Schottky contacts are easy to implement, as metals can be directly evaporated or sputtered onto the SI substrate. However, Schottky contacts allow electron injection into the GaAs substrate, leading to increased leakage current [6-7]. To eliminate this leakage current, an Ohmic contact using a heavily doped P+ GaAs contact layer can be employed [8-9]. The P+ layer creates a neutral region with flat energy bands which blocks the injection of electrons, as schematically shown in Figure 1.

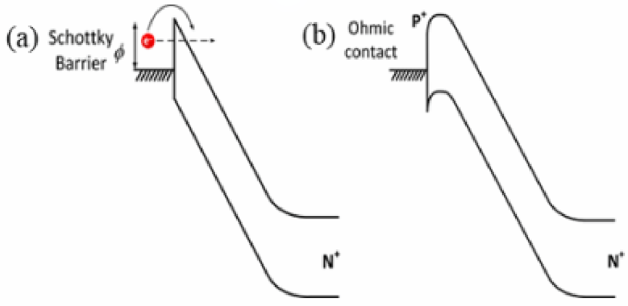

Figure 1: Schematic band diagram for: (a) Schottky contact (b) Ohmic contact.

We present the fabrication and characterization of SI GaAs alpha particle detectors incorporating a P+ doped layer grown on the front side of the detector. The growth process was carried out using MetalOrganic Chemical Vapor Deposition (MOCVD), and the performance of these detectors was compared with that of detectors utilizing Schottky contacts.

In this study we focus on optimizing the contact layer grown via MOCVD for advanced detector development. This involves evaluating a single wafer with both Ohmic and Schottky contact configurations to directly compare their effects on detector performance. Additionally, the impact of growing an N+ contact layer via MOCVD is being investigated, with a focus on its influence on critical parameters such as dark current, charge collection efficiency, and detector sensitivity. These findings aim to identify the optimal contact configuration and MOCVD growth parameters for achieving high-performance particle detectors.

The P-type Ohmic contact detector exhibited decreased dark current, in comparison to the Schottky contact detector, for biases up to 70 V as shown in the Figure 2:

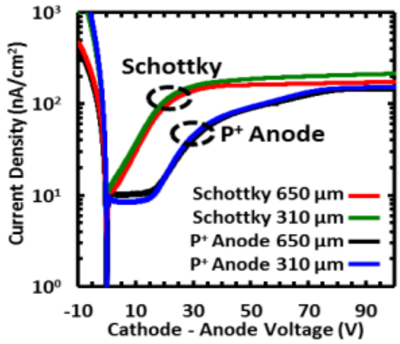

Figure 2: II-V characterization P+ contact detectors and Schottky contact detectors with 310 µm and 650 µm thicknesses

A comparison between the Schottky contact and P+ Ohmic contact detectors revealed that both exhibited the same charge collection efficiency (CCE). As shown in Figure 3a-b, the detected spectra for both detectors produced the same peak channel number. Additionally, for the 310 µm detectors, both the Schottky and P+ Ohmic configurations showed an increase in peak channel value and total counts, as illustrated in Figure 3c-d.

Reducing the substrate thickness from 650 µm to 310 µm led to a ~2× increase in CCE at 100 V, without increasing the leakage current. Further thinning is expected to enhance the CCE even further, making these detectors suitable for low-bias operation (<100V).

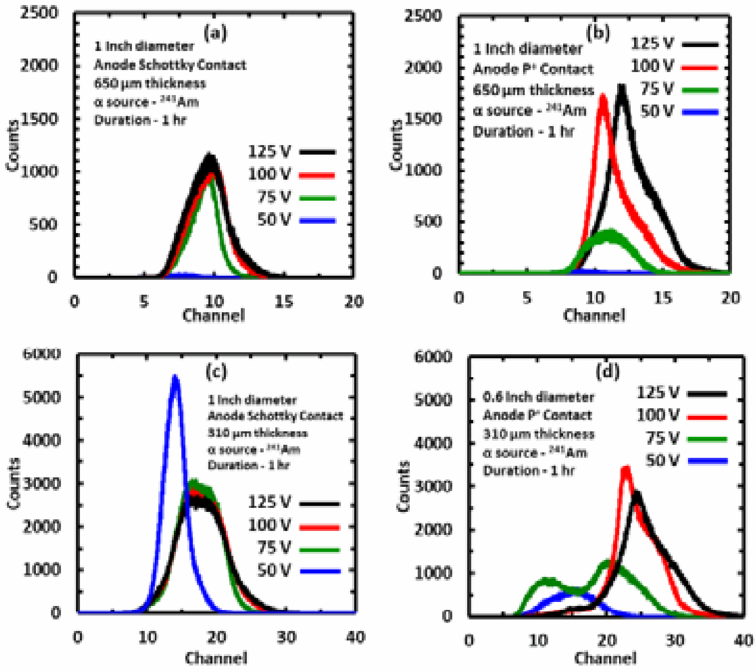

Figure 3: Spectrometry characterization for: (a) Schottky contact detector with 650 µm thickness (b) Ohmic contact detector with 650 µm thickness (c) Schottky contact detector with 310 µm thickness (c) Ohmic contact detector with 310 µm thickness.

These results demonstrate the potential of P+ GaAs contact layers to significantly improve the performance of GaAs-based particle detectors.

Cubic Ellipsoid Nuclear Model a Link between Nuclear Structure and Atomic Properties

R. Yavor

This study suggests that the nuclear structure determines the atomic properties and proposes a geometric nuclear model to confirm this. The model contains the advantages of the liquid drop, shell, collective and cluster models and can serve as a starting point to an effective field theory process. The main goal at this stage is not necessarily to obtain more accurate results than existing models, but rather to raise the possibility of a tangible interpretation of nuclear and atomic physics and to explore different perspectives of this idea. According to the model, the nucleus generally has an ellipsoidal shape, made up of a three-dimensional lattice of protonneutron bonds (treated here as a cubic system) and nuclear shells populated by protons, corresponding to the atomic shells and angular momentum, as represented by the periodic table. The excess neutrons (those not paired with protons) are in the nuclear envelope. First the nuclei with full orbitals are developed in a consistent manner and their masses are calculated in good agreement with empirical data. A link between the spatial nuclear structure and the atomic properties is then demonstrated by showing a linear dependence of the atomic covalent radius on the nuclear geometry.

Maximum Storage Time Period of Urine Sample for ICP-MS Uranium Analysis

Rinat Levy-Yanus, **Lior Carmel**, **Raphael Gonen**, **Shimon Tsroya**
Nuclear Research Center Negev, P. O. Box 9001, Beer-Sheva, ISRAEL 84190

Urine analysis is the most common method of radiobioassay for the assessment of internal exposure to uranium. At the Nuclear Research Center Negev (NRCN) urine samples for uranium analysis are collected as spot samples amounting a single urine void. In addition to the measurement of uranium concentration in the urine sample, its creatinine concentration is also measured in order to normalize the uranium concentration to a daily excretion rate needed for internal dose assessment.

The samples are introduced directly into a flow injection- ICP- MS (of the Institute of the Geological Survey of Israel) for uranium concentration determination and to a Cobas Integra 400 for creatinine concentration determination. In many cases, urine samples analysis is postponed due to various reasons, and therefore need to be stored temporarily until analysis is available. In most common cases at the NRCN, urine samples are stored for short periods (several weeks) in a refrigerator at 4° to 8°c. in some cases the urine samples need to be stored for extended periods.

This study examined the stability of uranium and creatinine concentration in urine samples when stored for longer periods at different temperatures.

The main conclusion of this study was that the uranium concentration was stable in the spot urine samples at 4° to 8°c for up to forty days. When frozen to -18°c or when stored at room temperature (22°c), the uranium concentration was stable until only 10 days. The creatinine concentration was stable in the spot urine samples at 4° to 8°c for eighty-seven days and when frozen to -18°c it kept its stability for one year.

The data presented in this study is unique as we didn't find any other data in the literature.

Addressing Challenges of Low-Energy Gamma Radiation Quantification for Environmental Samples by ALMERA

Mor Ben-Lulu, Zohar Yungrais, Gregory Gershinsky, Ayelet Ramazanov, Yamit Goldner, Getaneh Abebe, Ofer Aviv and Michal Brandis

The Gamma Spectrometry Laboratory participates in annual proficiency tests organized by ALMERA (Analytical Laboratories for the Measurement of Environmental Radioactivity), an IAEA-established network. These exercises are designed to assess the accuracy of radionuclide activity measurements across member laboratories and identify areas requiring further development.

As part of the 2024 ALMERA exercise, sediment and bauxite samples were analyzed using a high-purity germanium (HPGe) detector for gamma spectrometry. Initial measurements were performed using a calibration model, accounting for samples geometry and density. While high-energy gamma emitters such as Cs-137 were accurately quantified, low-energy emitters like Pb-210 (46.5 keV) exhibited significant discrepancies, with deviations of 130% and 30% from the expected activities in bauxite and sediment samples, respectively. Furthermore, the 2024 ALMERA report indicated that among 476 participating laboratories, only 25% and 33% obtained results consistent with the expected Pb-210 activities in bauxite and sediment, respectively.

Accurate quantification of low-energy gamma emitters is highly dependent on sample composition, as self-absorption effects can significantly impact detection efficiency. To account for these effect, X-ray fluorescence (XRF) was employed to determine the chemical composition of the samples, enabling refinements in the calibration model and ultimately, bringing Pb-210 activity assessments into agreement with expected values. Finally, this work highlights the importance of integrating compositional analysis and computational modeling to achieve accurate quantification of low-energy gamma emitters in complex matrices.

A new adhesive Material Resistant to Ionizing Radiation

Dr. Galit Bar, NRC Soreq, Yavne, Israel

Nuclear fusion has been recognized as the most promising technology for a sustainable, low-carbon source of energy. The advantages of fusion reactors include abundant and easily accessible fuel materials, and no production of long-lived nuclear waste. Recently, the U.S. Department of Energy (DOE) and the National Nuclear Security Administration (NNSA) announced the achievement of fusion ignition, which was obtained at the Lawrence Livermore National Laboratory (LLNL). This study demonstrated achieving a net positive energy gain from a fusion reaction. However, moving from the laboratory to a full-scale industrial reactor requires more research studies.

Material research in the field of fusion reactors is currently focused on synthesis and extraction of fuel materials and the development of construction materials capable of reliably withstanding the extremely severe operational conditions. To the best of our knowledge, there are no commercial adhesives available suitable for use in fusion reactors that sustain high-ionizing radiation. Therefore, development of such material is required and can be most beneficial as an adherent or sealant.

At NRC Soreq, a hybrid silica-rich (>70%) material was developed that presents high adhesive strength and excellent resistance to damaging effects induced by ionizing radiation. Additional properties of the new material include high transparency (in the visible range), low refractive index (1.42-1.44), outstanding moisture tightness, gas tightness (<10 ml/min for He), high thermal resistance (less than 4% weight loss up to 400 °C), and good chemical resistance to organic solvents.

Preliminary tests of the new adhesive material in the nuclear reactor at NRC Soreq showed the absence of radionuclides after exposure to thermal neutrons at a flow of 5x1012 Neutrons×cm-2 ×sec-1 for 1 minute. Furthermore, no visible damage, cracks, and bloating were observed following long exposure (several months) while the adhesive was submerged in the reactor pool in contact with the water. The synthesis of the material in the laboratory enables modification and improvement of its properties as needed. For example, changing the organic end groups can add flexibility or change the adhesion strength and adaptability to different surfaces. In addition, the optical activity of the material can be modified by combining alkoxides with different metal centers or radiation responsive nanoparticles. In the poster, I will present the new material and the potential for its integration into various applications in the field of nuclear energy research.